Contrib. Astron. Obs. Skalnaté Pleso **48**, 511 – 535, (2018)

Photometric and spectroscopic observations of Supernova 2014J in M82

D.Yu. Tsvetkov[1], V.G. Metlov[1], I.M. Volkov[1,2], S.Yu. Shugarov[1,3], V.P. Goranskij[1], T.N. Tarasova[4], N.N. Pavlyuk[1], A.V. Kusakin[5], M.A. Krugov[5], R.I. Kokumbaeva[5], E.A. Barsukova[6], A.F. Valeev[6], A.A. Nikiforova[7,8], I.S. Troitsky[7] and Yu.V. Troitskaya[7]

[1] *Sternberg Astronomical Institute, M.V. Lomonosov Moscow State University, Universitetsky pr. 13, 119234 Moscow, Russia*

[2] *Institute of Astronomy of the Russian Academy of Sciences, 48 Pyatnitskaya street, 119017 Moscow, Russia*

[3] *Astronomical Institute of the Slovak Academy of Sciences 059 60 Tatranská Lomnica, The Slovak Republic*

[4] *Crimean Astrophysical Observatory of the Russian Academy of Sciences, Nauchnyi, Crimea, 298409 Russia*

[5] *Fesenkov Astrophysical Institute, Almaty, Kazakhstan*

[6] *Special Astrophysical Observatory of the Russian Academy of Sciences, Nizhniy Arkhyz, Karachai-Cherkesia, 369167 Russia*

[7] *Astronomical Institute, St. Petersburg State University, 198504 St. Petersburg, Russia*

[8] *Pulkovo Observatory, 196140 St.Petersburg, Russia*

Received: March 30, 2018; Accepted: May 4, 2018

Abstract. We present 207 photometric epochs and 9 spectra of SN Ia 2014J in M82. $UBVRI$ photometry was carried out with 13 telescopes at 8 locations, covering the period from January 23, 2014 until May 15, 2015. The parameters of the light curves and interstellar extinction are determined. The comparison of different sets of photometric data is carried out. The light and colour curves of SN 2014J are compared to those for SNe Ia with similar photometric characteristics. We present results of high-cadence monitoring of SN 2014J in the BVR bands carried out on 6 nights and find no evidence for the microvariability. The spectral evolution is found to be typical for SNe Ia, with the expansion velocity at the maximum slightly greater than average and with a low velocity gradient.

Key words: supernovae: individual (SN 2014J)

1. Introduction

The homogeneity and high luminosity of type Ia supernovae (SNe Ia) determine their application for measuring extragalactic distances and estimating cosmological parameters (e.g., Pskovskii, 1977; Phillips, 1993; Riess et al., 1998;

Astier et al., 2006; Kessler et al., 2009). However, the results obtained in this way are based on the assumption that distant SNe are similar to well-studied nearby objects and their luminosities can be calibrated by identical methods. At present, many fundamental questions of the physics of SNe Ia, including the nature of presupernovae and the explosion mechanism, are still not completely clear. Therefore, accumulating observational data on nearby SNe Ia and elucidating the causes of differences in their characteristics remain important tasks of modern astrophysics.

Supernova (SN) 2014J, located at $\alpha = 9^{\mathrm{h}}\,55^{\mathrm{m}}\,42^{\mathrm{s}}.14, \delta = +69^\circ\,40'\,26''.0$ (2000.0) in the galaxy M82, was discovered by Steve J. Fossey on UT 2014 January 21.8.

At a distance of 3.5 Mpc (Karachentsev & Kashibadze, 2006) SN 2014J is the nearest SNIa after SN 1972E, and it offers the unique possibility to study a thermonuclear SN over a wide range of the electromagnetic spectrum.

The description of the discovery and early observations were presented by Goobar et al. (2014). The prediscovery data and early photometric and spectroscopic observations were reported by Zheng et al. (2014), Ashall et al. (2014), Denisenko et al. (2014), Itagaki et al. (2014), Gerke et al. (2014), Goobar et al. (2015). These sets of data show that SN 2014J is a spectroscopically normal Type Ia SN, although it exhibited high-velocity features in the spectrum and was heavily reddened by the dust in the host galaxy.

Follow-up photometric and spectroscopic observations were made by various groups, the largest sets of data are from Amanullah et al. (2014), Kawabata et al. (2014), Foley et al. (2014), Marion et al. (2015), and Srivastav et al. (2016).

Our observations for the first 40 days after the discovery were presented by Tsvetkov et al. (2014). In this paper we report the results of further extensive monitoring of SN 2014J in the optical bands carried out with 14 telescopes at 8 sites.

2. Observations and data reduction

CCD photometry of SN 2014J in the *UBVRI* passbands was carried out at:

- Nauchnyi in Crimea, where telescopes operated by the Crimean Astrophysical Observatory (CrAO) and Sternberg Astronomical Institute (SAI) are located;
- the Simeiz Observatory of CrAO, Simeiz, Crimea
- the Special Astrophysical Observatory (SAO), Nizhniy Arkhyz;
- the Moscow Observatory of SAI;
- the Caucasian Mountain Observatory (CMO) of SAI near Kislovodsk

- the Stará Lesná Observatory of the Astronomical Institute of the Slovak Academy of Sciences, Slovakia;
- the Tien-Shan Observatory (TSO) of the Fesenkov Astrophysical Institute near Almaty, Kazakhstan; and
- the Peterhof Observatory of Saint-Petersburg State University.

A list of the observing facilities is given in Table 1.

Table 1. Telescopes and detectors employed for the photometric observations.

Telescope code	Location	Aperture [m]	CCD camera	Filters	Scale [arcsec pixel^{-1}]	FoV [arcmin]
S60	Stará Lesná	0.6	FLI ML 3041	$UBVR_CI_C$	0.85	14.0
K50	Nauchnyi	0.5	Apogee Alta U8300	$UBVR_CI_C$	1.10	30.5x23.0
K60	Nauchnyi	0.6	Apogee AP-47p	$UBVR_CI_J$	0.7	6.0
M70	Moscow	0.7	Apogee AP-7p	$UBVR_CI_J$	0.64	5.5
M20	Moscow	0.2	Apogee AP-7p	BVR_CI_J	1.22	10.4
S100	Simeiz	1.0	FLI PL09000	$UBVR_CI_C$	0.96	9.8
S60	Simeiz	0.6	VersArray F512	BVR_CI_J	1.37	5.8
A100	TSO	1.0	Apogee Alta U9000	BVR_C	0.38	19.2
N100	SAO	1.0	EEV CCD42-40	$UBVR_CI_C$	0.48	8.3
N600	SAO	6.0	EEV CCD42-40	BVR_CI_C	0.36	6.3
C250	CMO	2.5	EEV CCD44-82	BVR_CI_C	0.15	10.0
P40	Peterhof	0.4	SBIG ST-7XME	BVR_CI_C	2.3	14.3x9.5
K70	Nauchnyi	0.7	SBIG ST-7XME	BVR_CI_C	1.3	8.1x5.4

The standard image reductions and photometry were made using the IRAF[1]. The magnitudes of the SN were derived by a PSF-fitting relatively to a sequence of local standard stars.

The CCD image of SN 2014J and local standard stars is presented in Fig. 1.

---

[1] IRAF is distributed by the National Optical Astronomy Observatory, which is operated by AURA under cooperative agreement with the National Science Foundation.

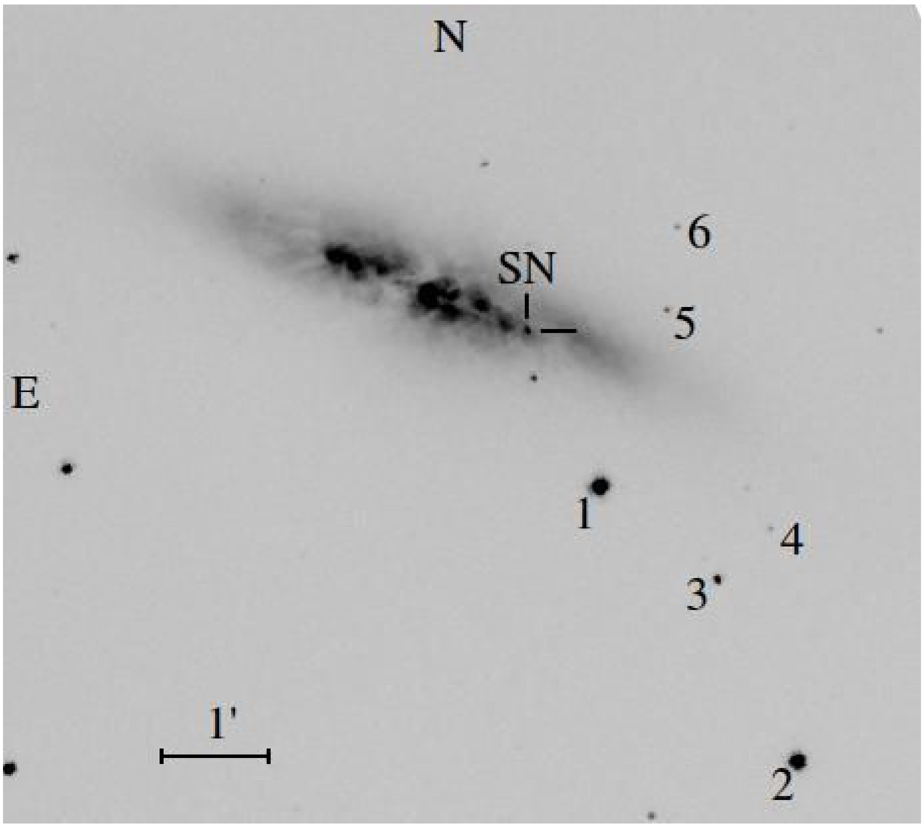

Figure 1. The image of SN 2014J and local standard stars.

The magnitudes of the local standards, calibrated on 15 nights relative to a standard in the field of the nearby galaxy M81 (Richmond et al., 1996), are reported in Table 2.

The surface brightness of the host galaxy at the location of the SN is high, and subtraction of the galaxy background is necessary for accurate photometry. We used the images obtained at the A100 before an SN outburst in 2012, and those taken at the K60 in 2016. These images were transformed, combined and used for galaxy substraction.

The photometry was transformed to the standard Johnson-Cousins system by means of instrumental colour-terms, determined from observations of standard star clusters.

Our photometry of the SN is presented in Tables 3,4, and 5.

Table 2. $UBVRI$ magnitudes of local standard stars.

Star	U	σ_U	B	σ_B	V	σ_V	R	σ_R	I	σ_I
1	10.84	0.02	10.63	0.01	10.03	0.01	9.70	0.01	9.41	0.01
2	12.15	0.02	11.51	0.01	10.69	0.01	10.23	0.01	9.87	0.01
3	14.29	0.03	14.32	0.01	13.76	0.01	13.43	0.01	13.10	0.01
4			16.31	0.02	16.09	0.02	15.99	0.02	15.87	0.02
5			17.75	0.05	16.31	0.03	15.43	0.02	14.62	0.02
6			17.38	0.04	16.45	0.03	15.93	0.03	15.47	0.03

Table 3.: $UBVRI$ photometry of SN 2014J at 10 telescopes.

JD−2450000	U	σ_U	B	σ_B	V	σ_V	R	σ_R	I	σ_I	Tel.
6682.13			12.48	0.04	11.18	0.03	10.52	0.03	10.04	0.02	M20
6686.20			12.07	0.03	10.75	0.03	10.24	0.03	9.78	0.02	M20
6687.13			11.98	0.03	10.68	0.02	10.16	0.02	9.73	0.01	M20
6688.17			11.97	0.03	10.65	0.02	10.14	0.02	9.73	0.01	M20
6689.13			11.95	0.02	10.59	0.02	10.11	0.03	9.72	0.02	M20
6691.18	12.70	0.04	11.85	0.02	10.50	0.01	10.05	0.01	9.87	0.02	K50
6692.20	12.77	0.04	11.87	0.02	10.50	0.02	10.06	0.02	9.91	0.02	K50
6693.17	12.77	0.03	11.90	0.02	10.50	0.01	10.08	0.01	9.94	0.02	K50
6694.17	12.71	0.04	11.94	0.02	10.52	0.02	10.08	0.02	9.96	0.02	K50
6694.49	12.86	0.05	12.00	0.02	10.68	0.02	10.11	0.02	10.00	0.03	T60
6695.18			11.99	0.01	10.53	0.02	10.12	0.02	10.00	0.02	K50
6696.16			12.03	0.01	10.54	0.03	10.17	0.02	10.03	0.02	K50
6700.17	13.04	0.07	12.28	0.02	10.71	0.02	10.42	0.02	10.28	0.01	K50
6701.20			12.38	0.01	10.77	0.03	10.52	0.02	10.33	0.02	K50
6702.30	13.44	0.04	12.48	0.01	10.83	0.02	10.60	0.01	10.38	0.02	K50
6702.45	13.51	0.03	12.54	0.01	11.01	0.01	10.57	0.02	10.39	0.03	T60
6706.22	13.99	0.11	12.89	0.01	11.08	0.01	10.77	0.01	10.40	0.02	K50
6707.17	14.07	0.04	12.99	0.01	11.11	0.02	10.81	0.01	10.40	0.03	K50
6708.22			13.19	0.06	11.25	0.03	10.77	0.04			M20
6708.23	14.27	0.07	13.08	0.01	11.15	0.02	10.81	0.02	10.38	0.02	K50
6711.35	14.58	0.06	13.39	0.02	11.28	0.02	10.81	0.02	10.30	0.03	K50
6712.18			13.49	0.05	11.31	0.01	10.81	0.02	10.28	0.02	K50
6712.25	14.83	0.06	13.56	0.02	11.51	0.02	10.76	0.02	10.22	0.02	T60
6714.22			13.79	0.02	11.48	0.02	10.84	0.02	10.14	0.02	M20
6714.40	14.97	0.04	13.71	0.02	11.56	0.02	10.80	0.02	10.13	0.02	T60
6715.18			13.84	0.02	11.51	0.02	10.85	0.02	10.12	0.01	M20
6715.42	15.10	0.03	13.79	0.03	11.62	0.02	10.81	0.01	10.14	0.02	T60
6716.31	15.44	0.04	14.08	0.01	11.59	0.01	10.88	0.01	10.13	0.01	M70
6716.41	15.24	0.07	13.89	0.02	11.67	0.02	10.85	0.03	10.13	0.03	T60
6717.23	15.43	0.03	14.17	0.02	11.63	0.01	10.92	0.02	10.15	0.02	M70
6718.42	15.32	0.03	14.08	0.02	11.74	0.01	10.86	0.02	10.09	0.02	T60

Table 3.: Continued.

JD− 2450000	U	σ_U	B	σ_B	V	σ_V	R	σ_R	I	σ_I	Tel.
6719.31			14.08	0.02	11.64	0.02	10.93	0.02	10.20	0.02	K50
6720.18	15.40	0.05	14.11	0.02	11.68	0.02	10.94	0.01	10.19	0.01	K50
6722.23	15.78	0.06	14.24	0.01	11.79	0.03	11.06	0.01	10.27	0.02	K50
6726.20	15.79	0.10	14.74	0.02	12.16	0.02	11.41	0.01	10.48	0.01	M70
6727.19			14.50	0.03	12.10	0.02	11.41	0.01	10.58	0.02	K50
6730.19			14.63	0.03	12.23	0.02	11.57	0.02	10.78	0.02	K50
6735.20	16.03	0.11	14.71	0.02	12.39	0.03	11.80	0.03	11.07	0.04	K50
6738.21	16.21	0.12	14.83	0.02	12.49	0.01	11.90	0.01	11.21	0.02	K50
6739.20	16.20	0.11	14.79	0.02	12.49	0.02	11.94	0.02	11.27	0.02	K50
6740.23			14.82	0.02	12.54	0.01	11.95	0.01	11.31	0.02	K50
6740.27	16.43	0.07	15.06	0.01	12.67	0.02	12.01	0.01	11.23	0.01	M70
6741.23	16.17	0.12	14.84	0.02	12.57	0.02	12.01	0.01	11.36	0.02	K50
6743.25			15.10	0.01	12.76	0.02	12.13	0.02	11.36	0.01	M70
6745.37	16.13	0.08	14.93	0.04	12.90	0.02	12.16	0.02	11.51	0.04	T60
6746.22			15.15	0.01	12.85	0.02	12.25	0.02	11.51	0.01	M70
6747.25	16.25	0.08	14.97	0.02	12.94	0.01	12.20	0.01	11.56	0.02	K50
6747.27			14.91	0.02	12.76	0.02	12.21	0.02	11.63	0.02	T60
6748.25	16.30	0.08	14.91	0.02	12.78	0.02	12.25	0.02	11.69	0.02	K50
6750.29			15.14	0.03	12.79	0.01	12.33	0.01	11.74	0.02	K50
6751.23	16.54	0.14	14.97	0.02	12.87	0.02	12.34	0.01	11.80	0.02	K50
6751.55	16.32	0.04	15.15	0.02	13.14	0.02	12.39	0.02	11.87	0.02	N100
6755.24			15.00	0.02	12.94	0.02	12.46	0.02	11.96	0.02	K50
6756.25	16.27	0.08			13.14	0.02	12.57	0.02	11.94	0.01	M70
6757.25			15.24	0.01	13.15	0.02	12.59	0.01	11.99	0.01	M70
6758.24	16.54	0.05	15.25	0.01	13.18	0.02	12.63	0.01	12.03	0.01	M70
6758.29	16.60	0.06	15.18	0.02	13.32	0.02	12.59	0.01	12.04	0.02	T60
6761.25	16.90	0.16	15.26	0.02	13.24	0.02	12.70	0.02	12.14	0.02	M70
6762.39			15.17	0.02	13.20	0.04	12.69	0.02			K60
6763.24			15.25	0.02	13.29	0.02	12.73	0.02	12.05	0.02	K60
6768.27	16.70	0.06	15.35	0.02	13.45	0.01	12.93	0.02	12.42	0.02	M70
6771.26			15.31	0.02	13.52	0.02	12.98	0.02			K60
6772.26			15.42	0.01	13.56	0.02	13.05	0.01	12.57	0.01	M70
6774.26			15.25	0.02	13.50	0.02	13.09	0.02	12.69	0.01	K50
6775.30			15.48	0.03	13.63	0.02	13.17	0.03	12.71	0.02	M70
6777.29	17.13	0.17	15.47	0.02	13.68	0.02	13.19	0.02	12.75	0.02	M70
6783.57			15.35	0.02	13.92	0.02	13.38	0.02	13.10	0.03	T60
6785.42			15.34	0.03	13.79	0.04	13.32	0.02			K60
6786.27			15.45	0.02	13.90	0.02	13.42	0.02	12.89	0.03	K60
6786.29			15.40	0.03	13.77	0.03	13.46	0.02	13.13	0.01	K50
6786.30			15.55	0.04	13.95	0.02	13.49	0.01	13.01	0.01	S100
6787.52	17.09	0.14	15.51	0.02	14.00	0.02	13.52	0.01	13.24	0.02	T60
6788.26			15.66	0.03	13.75	0.03	13.37	0.02	13.00	0.03	S100
6788.27			15.43	0.02	13.88	0.02	13.53	0.02	13.22	0.02	K50
6788.39	17.21	0.17	15.53	0.02	14.09	0.02	13.52	0.03	13.21	0.02	T60

Table 3.: Continued.

JD− 2450000	U	σ_U	B	σ_B	V	σ_V	R	σ_R	I	σ_I	Tel.
6789.30	17.26	0.08	15.57	0.02	14.01	0.02	13.57	0.02	13.11	0.02	S100
6790.36			15.62	0.02	14.01	0.02	13.55	0.03	13.12	0.03	S100
6792.25			15.66	0.10	14.04	0.02	13.64	0.02	13.13	0.03	S100
6794.27	17.29	0.19	15.71	0.03	14.18	0.02			13.28	0.01	S100
6795.25			15.66	0.04	14.15	0.02	13.77	0.01	13.29	0.02	S100
6796.29			15.67	0.02	14.16	0.01	13.72	0.01	13.30	0.02	S100
6798.34			15.75	0.01	14.23	0.02	13.80	0.01	13.38	0.02	M70
6799.28			15.59	0.02	14.12	0.02	13.84	0.02	13.49	0.03	K50
6799.34			15.71	0.02	14.24	0.02	13.83	0.02	13.35	0.02	S60
6803.32			15.78	0.03	14.40	0.02	13.89	0.03	13.65	0.03	S100
6803.38	17.51	0.08	15.74	0.02	14.42	0.02	13.95	0.02	13.64	0.03	N100
6805.31			15.77	0.02	14.41	0.02	13.98	0.03	13.65	0.04	K50
6805.40	17.25	0.18	15.71	0.02	14.30	0.02	14.01	0.03	13.66	0.03	S100
6806.29			15.85	0.02	14.42	0.03	14.00	0.02	13.66	0.03	S100
6806.30			15.88	0.03	14.42	0.02	13.98	0.02	13.41	0.02	K60
6807.31			15.76	0.02	14.31	0.03	14.11	0.02	13.70	0.03	K50
6808.29			15.86	0.04	14.51	0.02	14.07	0.03	13.77	0.03	S100
6812.30			15.88	0.05	14.50	0.03	14.21	0.03	13.74	0.03	S60
6818.34			15.95	0.02	14.59	0.01	14.42	0.02	14.01	0.02	K50
6832.29			16.16	0.02	14.90	0.02	14.78	0.02	14.31	0.02	K50
6850.29	18.71	0.09	16.36	0.03	15.32	0.03	15.13	0.02	14.77	0.02	N100
6851.33			16.39	0.03	15.36	0.02	15.13	0.02	14.80	0.02	N100
6852.30			16.45	0.02	15.41	0.02	15.18	0.02	14.83	0.02	N100
6893.26					15.99	0.05	16.06	0.11			K50
6896.31			17.08	0.04	16.18	0.03	15.99	0.03	15.03	0.03	K60
6897.24			17.10	0.03	16.20	0.03	16.01	0.03	15.08	0.02	K60
6899.27			17.21	0.03	16.19	0.02	16.05	0.03	15.03	0.02	K60
6900.24			17.07	0.07	16.17	0.03	16.06	0.03	15.00	0.03	K60
6901.24			17.12	0.05	16.25	0.04	15.99	0.03	15.11	0.05	K60
6902.24			17.07	0.04	16.21	0.03	16.03	0.03	15.17	0.04	K60
6904.23			17.12	0.08	16.21	0.02	16.05	0.04	15.24	0.05	K60
6905.23					16.29	0.04	16.14	0.03	15.36	0.08	K60
6906.22					16.25	0.04	16.11	0.03	15.35	0.06	K60
6908.23			17.15	0.06	16.34	0.04	16.20	0.03	15.33	0.05	K60
6916.47			17.34	0.05	16.51	0.05	16.36	0.04	15.55	0.07	K60
6919.45			17.60	0.07	16.62	0.05	16.44	0.04	15.60	0.07	K60
6941.43			17.86	0.09	16.90	0.03	16.79	0.04	15.79	0.05	K60
6959.61					17.11	0.05	17.05	0.04	16.23	0.05	N100
6967.38			17.92	0.08	17.22	0.04	17.15	0.04	16.18	0.05	K60
6969.44			18.14	0.08	17.30	0.03	17.15	0.05	16.18	0.09	K60
6973.47			18.18	0.06	17.31	0.04	17.22	0.04	16.14	0.05	K60
6974.60			18.16	0.06	17.31	0.03	17.27	0.03	16.49	0.04	N100
6983.55			18.33	0.04	17.46	0.04	17.40	0.04	16.51	0.04	N100
7040.56			18.99	0.12	17.95	0.08	17.88	0.07			N600

Table 3.: Continued.

JD− 2450000	U	σ_U	B	σ_B	V	σ_V	R	σ_R	I	σ_I	Tel.
7071.40					18.44	0.12					S100
7073.14			19.54	0.07	18.49	0.06	18.26	0.09	17.38	0.06	C250
7074.52					18.49	0.05					S100
7078.30									17.17	0.10	S100
7106.27							18.42	0.15			K60

Table 4.: *BVRI* photometry of SN2014J at the P40 and K70 telescopes.

JD− 2456000	B	σ_B	V	σ_V	R	σ_R	I	σ_I	Tel.
681.26					10.73	0.04			P40
681.27	12.75	0.04	11.39	0.04	10.72	0.04	10.32	0.02	P40
685.32	12.11	0.01	10.84	0.02	10.25	0.02	9.89	0.01	P40
686.28	12.07	0.02	10.77	0.02	10.17	0.02	9.87	0.01	P40
687.25	12.01	0.02	10.73	0.01	10.16	0.02	9.85	0.01	P40
688.38	11.98	0.01	10.68	0.01	10.13	0.01	9.84	0.01	P40
693.36	12.00	0.01	10.61	0.01	10.12	0.02	9.98	0.02	K70
694.39	12.05	0.05	10.63	0.02	10.13	0.03	10.01	0.03	K70
695.29	12.07	0.02	10.65	0.01	10.14	0.02	10.06	0.01	P40
713.32	13.61	0.04	11.53	0.03	10.84	0.01	10.27	0.02	P40
715.47	13.85	0.03	11.60	0.02	10.88	0.02	10.20	0.03	P40
716.49					10.90	0.01			P40
717.26	14.03	0.02	11.71	0.03	10.91	0.01	10.21	0.02	P40
724.32	14.54	0.02	12.09	0.01	11.26	0.03	10.38	0.02	P40
726.42					11.42	0.02	10.55	0.01	P40
728.38	14.61	0.06	12.32	0.03	11.54	0.02	10.70	0.02	P40
729.32	14.73	0.02	12.37	0.01	11.59	0.01	10.74	0.02	P40
730.39	14.74	0.02	12.43	0.03	11.65	0.02	10.82	0.03	P40
731.38	14.77	0.03	12.47	0.02	11.70	0.02	10.87	0.03	P40
734.24			12.55	0.02	11.82	0.02			P40
736.35	14.86	0.03	12.63	0.01	11.88	0.01	11.13	0.01	P40
738.27	14.98	0.02	12.70	0.03	11.97	0.02	11.25	0.03	P40
739.25	14.95	0.02	12.72	0.02	11.98	0.02	11.28	0.03	P40
743.38	15.06	0.04	12.79	0.03	12.12	0.04	11.46	0.02	P40
744.29	14.95	0.05	12.76	0.05	12.10	0.05	11.45	0.03	P40
744.30	14.99	0.03	12.90	0.02	12.15	0.01	11.44	0.03	K70
745.52	15.09	0.04	12.87	0.03	12.19	0.03	11.56	0.02	P40
746.42	15.08	0.03	12.91	0.02	12.22	0.02	11.61	0.01	P40
752.35	15.17	0.03	13.11	0.02	12.40	0.03	11.87	0.04	P40
753.33					12.44	0.03			P40
755.35	15.31	0.05	13.25	0.04	12.46	0.06	12.01	0.04	P40

Table 4.: Continued.

JD– 2456000	B	σ_B	V	σ_V	R	σ_R	I	σ_I	Tel.
756.32	15.16	0.04	13.17	0.04	12.57	0.01	12.05	0.02	P40
757.30	15.29	0.04	13.25	0.01	12.59	0.02	12.10	0.02	P40
758.42	15.24	0.04	13.25	0.01	12.62	0.02	12.14	0.02	P40
760.31	15.14	0.03	13.31	0.01	12.65	0.03	12.19	0.02	P40
764.39	15.28	0.05	13.38	0.04	12.78	0.03	12.39	0.02	P40
765.32	15.22	0.05	13.45	0.02	12.84	0.02	12.40	0.03	P40
766.44	15.27	0.03	13.50	0.02	12.86	0.03	12.41	0.03	P40
767.37	15.23	0.07	13.46	0.04	12.89	0.01	12.48	0.02	P40
768.34	15.28	0.04	13.51	0.02	12.84	0.06	12.47	0.04	P40
769.30	15.22	0.05	13.49	0.03	12.92	0.03	12.54	0.02	K70
770.27	15.24	0.05	13.53	0.03	12.95	0.03	12.58	0.02	K70
770.34	15.27	0.06	13.56	0.03	12.97	0.02	12.58	0.02	P40
771.34	15.21	0.06	13.59	0.04	13.00	0.03	12.57	0.02	K70
772.32	15.33	0.06			13.03	0.03	12.69	0.02	K70
773.28	15.22	0.04	13.65	0.03	13.04	0.03	12.71	0.02	K70
773.35	15.38	0.04	13.63	0.03	13.07	0.03	12.74	0.04	P40
775.32	15.33	0.03	13.68	0.02	13.14	0.02	12.81	0.02	K70
780.39	15.36	0.08	13.83	0.05	13.25	0.04	12.95	0.05	P40
780.47	15.42	0.01	13.83	0.02	13.27	0.02	12.98	0.02	K70

Spectroscopic observations were carried out at the 2.6-m Shajn telescope of CrAO on 5 dates from February 4 until June 29, 2014. The spectrograph SPEM provided the wavelength range of 3300–7550 Å with a dispersion of 2Åpixel^{-1}. The spectra were bias and flat-field corrected, extracted and wavelength calibrated with the SPERED code developed by S.I. Sergeev at the CrAO. The spectrophotometric standard HR3894 was used for flux calibrated spectra.

At SAO spectroscopic observations were obtained at the 1-meter telescope with a spectrograph UAGS, which provided the wavelength range of 3507–7885 Å with a dispersion of 2.2 Åpixel^{-1}, and at the 6-meter telescope with a SCORPIO focal reducer and grisms VPHG550G and VPHG1200G. The grism VPHG1200G provided the wavelength range of 4044–5858 Å with a dispersion of 0.88 Åpixel^{-1}, while the grism VPHG550G yielded the range of 3670–7906 Å and a dispersion of 2.3 Åpixel^{-1}.

The spectra were bias and flat-field corrected, extracted and wavelength calibrated in ESO/MIDAS. The spectrophotometric standard AGK+81°266 was used for flux calibrated spectra.

Table 5. *BVR* observations of SN2014J at the A100 telescope.

JD−2450000	B	σ_B	V	σ_V	R	σ_R
6697.37	12.11	0.02	10.59	0.01	10.10	0.01
6697.51	12.11	0.02	10.60	0.01	10.11	0.01
6698.29	12.23	0.01	10.69	0.01	10.23	0.01
6698.42	12.24	0.01	10.69	0.01	10.23	0.01
6705.49	12.88	0.01	11.13	0.02	10.68	0.02
6715.41	13.93	0.02	11.52	0.05	10.82	0.04
6717.10	14.08	0.02	11.61	0.02	10.84	0.04
6719.07	14.23	0.02	11.69	0.02	10.90	0.02
6720.06	14.31	0.03	11.73	0.03	10.93	0.04
6721.08	14.40	0.02	11.73	0.09	11.05	0.01
6722.07	14.44	0.02	11.85	0.04	11.00	0.05
6727.10	14.73	0.01	12.22	0.01	11.60	0.01
6728.07	14.75	0.01	12.25	0.01	11.48	0.01
6729.07	14.79	0.01	12.32	0.01	11.61	0.01
6748.09	15.06	0.01	12.90	0.01	12.27	0.01
6749.08	15.08	0.02	12.89	0.03	12.31	0.01
6751.19	15.16	0.03	12.96	0.03	12.36	0.01
6756.11	15.15	0.01	13.11	0.01	12.51	0.01
6757.21	15.13	0.01	13.14	0.01	12.56	0.01
6758.18	15.11	0.03	13.16	0.02	12.58	0.02
6759.23	15.15	0.05	13.12	0.04	12.58	0.01
6780.26	15.44	0.04	13.78	0.03	13.26	0.03
6782.20	15.45	0.04	13.80	0.03	13.29	0.03
6787.16	15.52	0.04	13.92	0.03	13.44	0.03
6789.14	15.59	0.04	14.01	0.03	13.54	0.03
6791.15	15.59	0.04	14.05	0.03	13.58	0.03
6792.21	15.61	0.04	14.06	0.03	13.58	0.03
6795.31	15.65	0.04	14.17	0.03	13.72	0.02
6801.16	15.74	0.04	14.32	0.02	13.88	0.02
6802.17	15.76	0.04	14.35	0.03	13.92	0.03
6809.14	15.86	0.04	14.50	0.03	14.10	0.02
6837.15			15.09	0.03	14.78	0.04
7001.42	18.51	0.06	17.58	0.05	17.59	0.05

3. Light and colour curves

The complete light curves of SN 2014J are presented in Fig. 2, and the curves around the maximum are shown in Fig. 3.

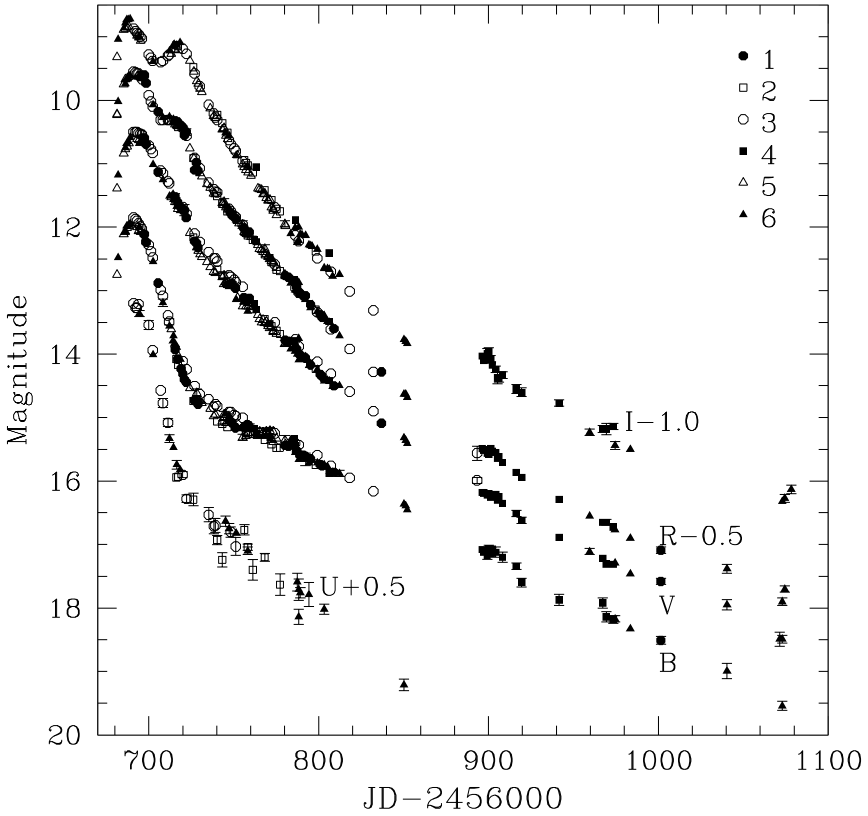

Figure 2. The light curves of SN 2014J in the *UBVRI* bands. The curves are shifted vertically for clarity, the amount of shift is indicated on the plot. The error bars are plotted only when they exceed the size of a symbol. The shape of the symbols corresponds to the instruments used: 1 - A100, 2 - M70, 3 - K50, 4 - K60, 5 - P40 and K70, and 6 - other telescopes.

The results for all the telescopes are in a fairly good agreement, but some systematic differences can be noted. At phase near the maximum the differences in the *I*-band magnitudes between M20 and P40 are evident, and soon after the maximum the *V*-band magnitudes from P40 and M20 are ~ 0.1 mag lower than

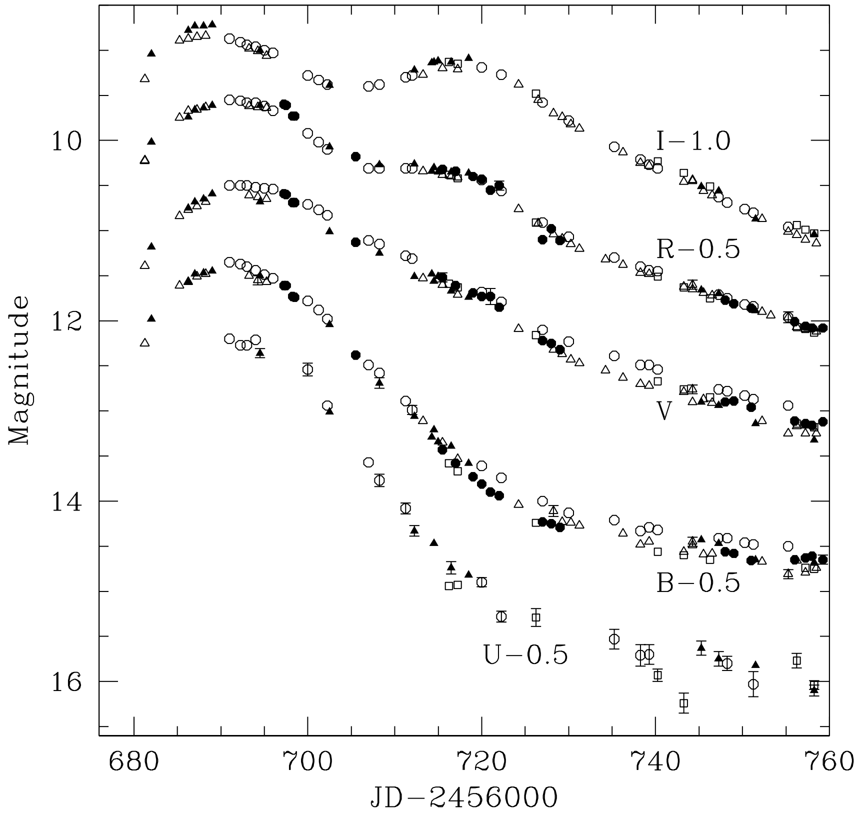

Figure 3. The light curves of SN 2014J near the maximum light.

those from K50. At the phase ∼ 30 days past the maximum the difference in the *B*-magnitudes becomes evident, estimates from K50 are about 0.2 mag higher than those from other sources.

The light curves from five major data sets (Amanullah et al. (2014), Kawabata et al. (2014), Foley et al. (2014), Marion et al. (2015), and Srivastav et al. (2016)) are compared in Fig. 4. The large differences of the *B* magnitudes at phases 30–60 days are revealed. The difference between brightest (Foley et al., 2014) and faintest (Kawabata et al., 2014) estimates amounts to 0.5 mag. Our magnitudes from K50 are closer to the data from Foley et al. (2014), while data from other telescopes are in good agreement with the results by Srivastav et al. (2016).

The agreement between various sets of the *U*-band magnitudes is very poor.

While there is reasonable agreement between data from Srivastav et al. (2016) and Marion et al. (2015), our data and magnitudes from Amanullah et al. (2014) are ~ 0.3 mag fainter at all phases, and the results from the Swift satellite[2] are further 0.5 mag fainter.

The agreement of the V, R and I magnitudes is much better, with the maximum difference not exceeding 0.2 mag.

We conclude that photomery of such a red object on bright background faces significant problems. It is clear that the transformation of instrumental magnitudes to the standard Johnson-Cousins system using linear colour terms is not accurate in this case. Unfortunately, we have no possibility to apply the S-correction method (Stritzinger et al., 2002), and have to take the average values as more reliable.

We fitted the photometric data near the maximum with cubic splines and determined the dates and magnitudes of maximum light and the decline parameters Δm_{15} in different bands. The calculations were carried out for our data and for the combination of our data with the results from the authors listed above. The results are presented in Table 6. The differences between the estimates of maximum magnitudes are very small, but there are some distinctions in determination of dates of maximum and Δm_{15}.

Table 6. Dates and magnitudes of maximum light (for the *I*-band also for the secondary maximum) and the decline rate parameters in different passbands. The results for our data are reported at the upper part, and those for the combination of our photometry with the data from other authors are at the lower part.

Band	JD−2456000	mag	Δm_{15}
B	690.6± 0.7	11.91± 0.05	0.96± 0.05
V	692.4± 0.6	10.53± 0.04	0.64± 0.04
R	692.8± 0.5	10.06± 0.04	0.77± 0.05
I	688.4± 0.9	9.75± 0.08	0.65± 0.10
I_{sec}	717.2± 0.6	10.15± 0.04	
U	687.4± 1.1	12.55±0.08	0.91±0.2
B	691.6± 0.8	11.93±0.05	1.10± 0.05
V	692.4± 0.5	10.55± 0.03	0.70± 0.05
R	691.2± 0.5	10.09± 0.04	0.70± 0.05
I	688.3± 0.9	9.80± 0.08	0.57± 0.10
I_{sec}	717.3± 0.5	10.15± 0.04	

As our observations continued for more than 400 days after the maximum, it is possible to determine the rates of decline on the exponential tail, which started at about 100 days after the maximum light.

---

[2] http://people.physics.tamu.edu/pbrown/SwiftSN/ swift_sn.html

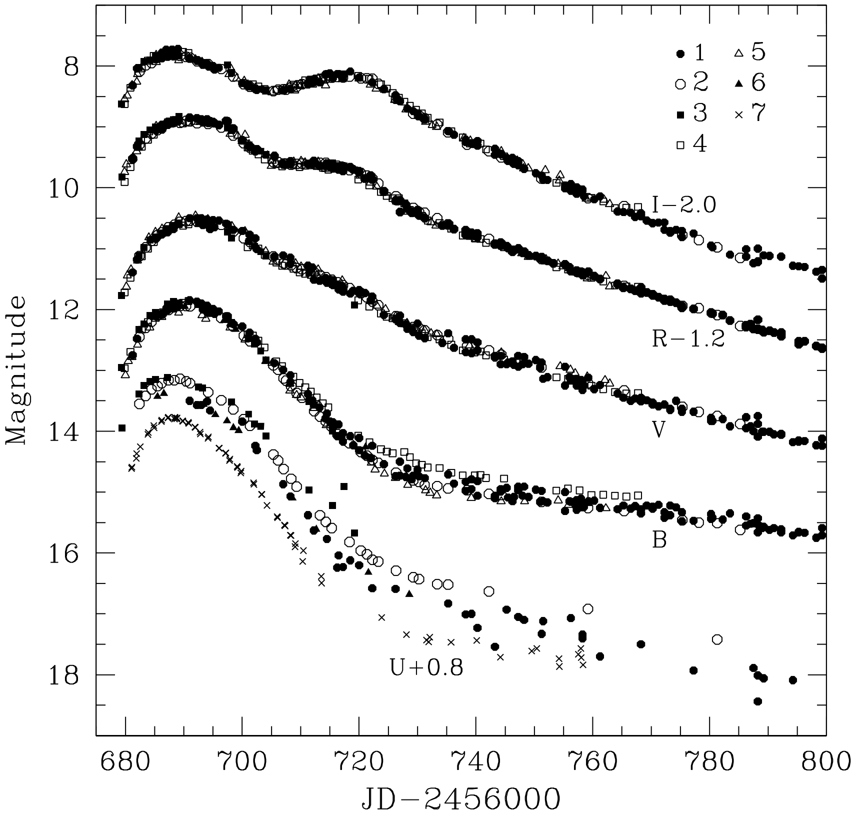

Figure 4. The light curves of SN 2014J from different data sets: 1 - this work, 2 - Srivastav et al. (2016), 3 - Marion et al. (2015), 4 - Foley et al. (2014), 5 - Kawabata et al. (2014), 6 - Amanullah et al. (2014), and 7 - Swift.

The decline rates in magnitudes per day on the exponential tail in the $BVRI$-bands, determined by linear least-square fitting, are 0.0140 ± 0.0003, 0.0142 ± 0.0002, 0.0139 ± 0.0002, and 0.0127 ± 0.0002, respectively. The decline rates in the B, V and R bands are virtually the same, while the I-band decline is slower.

The comparison of light curves for SN 2014J and SNe Ia with a similar value of Δm_{15} is presented in Fig. 5. The light curves in the U, V and R bands are practically identical for all SNe. The most evident difference is for the B-band at a phase interval of 30–50 days. At that stage there is a pronounced protrusion on the B-band light curve of SN 2014J, SNe 2002bo (Benetti et al., 2004) and 2006X

(Wang et al., 2008) show similar behaviour. The light curves of SNe 2003du (Stanishev et al., 2007), 2005cf (Wang et al., 2009b) and 2011fe (Tsvetkov et al., 2013) are linear after the bend from fast decay to the tail, and the difference between these SNe and SN 2014J is evident.

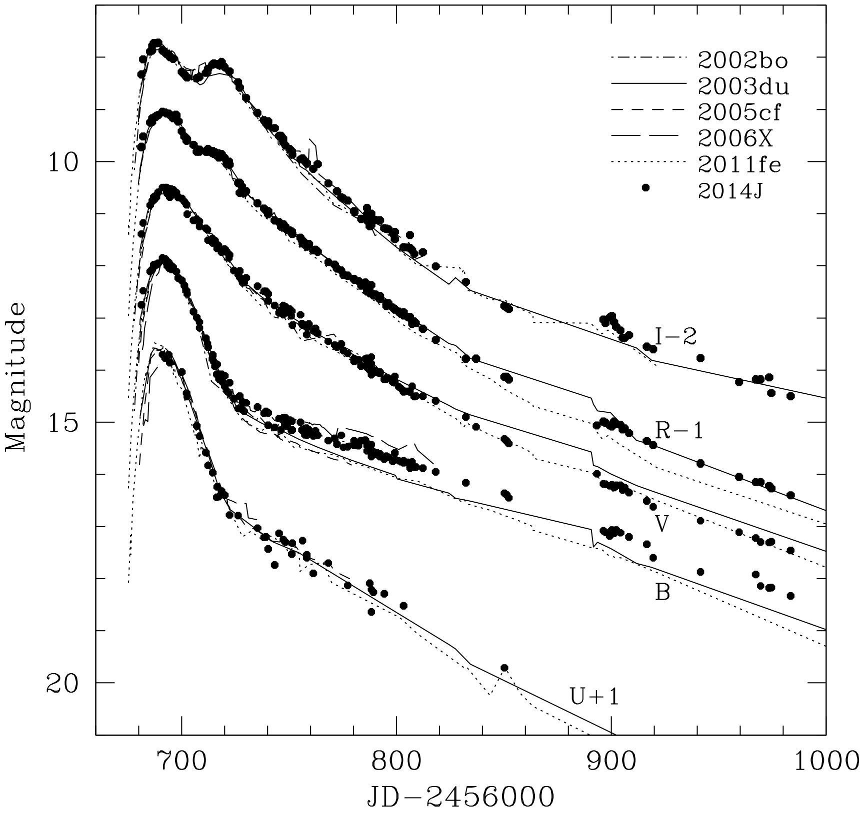

Figure 5. Comparison of the light curves of SN 2014J with those for 5 SNe Ia with nearly the same Δm_{15}.

The colour curves for SN 2014J are presented in Fig. 6. The colour evolution is typical for SN Ia, this is confirmed by comparison with the colour curves for SNe 2002bo, 2003du, 2005cf, 2006X and 2011fe. The colour curves of these SNe are in general agreement with the curves for SN 2014J, although some differences are revealed. The $(B-V)$ colour of SN 2014J is significantly bluer at phase $>$ 100 days than for SNe 2011fe and 2003du, while the $(V-R)$ colour is redder.

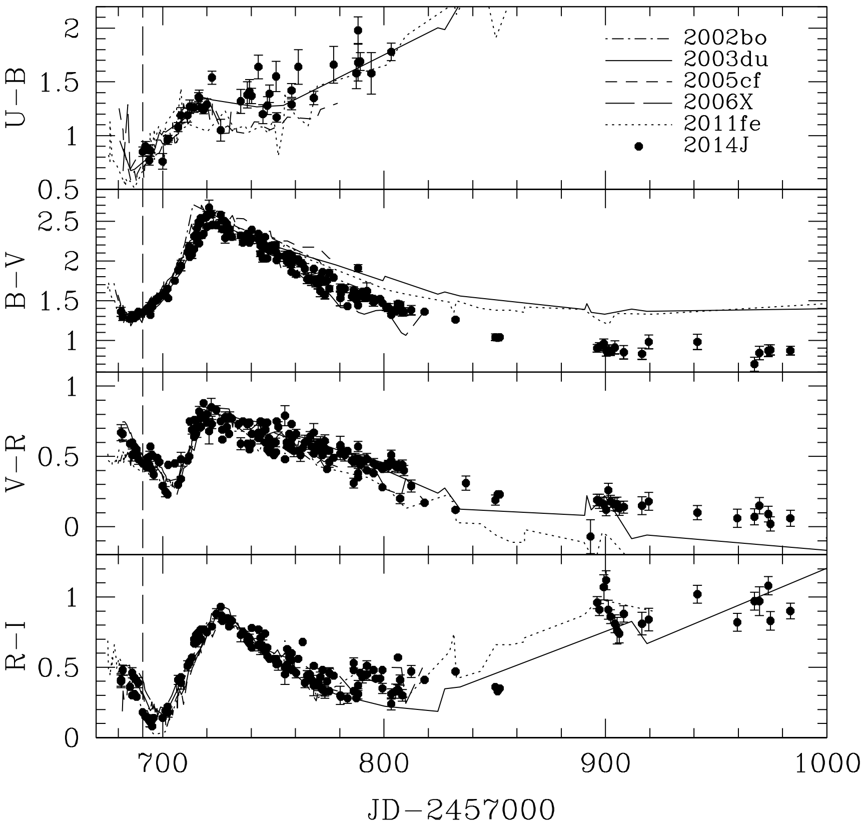

Figure 6. The colour curves of SN 2014J and comparison with those for 5 SNe Ia with nearly the same Δm_{15}. The time of B-band maximum is shown by a vertical dashed line.

The amount of shift applied to match the curves can be considered as an estimate of the colour excess of SN 2014J. We adopted the following colour excesses $E(B-V)$ for the SNe 2002bo, 2003du, 2005cf, 2006X, and 2011fe: 0.43, 0.01, 0.09, 1.26, and 0.01 mag, respectively, from the works cited earlier.

We obtained the following estimates: $E(U-B)=1.07\pm0.10$, $E(B-V)=1.38\pm0.04$, $E(V-R)=0.44\pm0.04$, and $E(R-I)=0.56\pm0.05$ mag.

The $(B-V)$ colour curve is also compared with the "Lira-Phillips" relation (Phillips et al., 1999), showing the time dependence of $(B-V)$ in the phase interval 30–90 days after the maximum for SNe Ia that suffered no extinction. This method yields $E(B-V)=1.35\pm0.02$ mag, in good agreement with the previous estimate. We adopt the mean value $E(B-V) = 1.36 \pm 0.03$ mag as most probable.

The colour excess due to the galactic extinction is $E(B-V)_{gal} = 0.14$ mag according to Schlafly & Finkbeiner (2011), so the colour excess in the host galaxy is $E(B-V)_{host} = 1.22$. If we assume the distance modulus for M82 $\mu = 27.73$ (Karachentsev & Kashibadze, 2006), then the absolute magnitudes, corrected for the galactic extinction, are -16.37 and -17.61 mag in the B and V bands, respectively.

Our value of $\Delta m_{15}(B) = 0.96$ is the same as determined by Srivastav et al. (2016), so we conclude that the true value of this parameter, corrected for the colour excess, is $\Delta m_{15}(B)_{true} = 1.08$.

According to the calibration of the Pskovskiy-Phillips relation by Prieto et al. (2006), the mean absolute magnitudes for SN Ia with $\Delta m_{15}(B) = 1.08$ are $M_B = -19.33$ and $M_V = -19.26$ mag.

We can calculate the most probable values of extinction in the host galaxy $A_B = 2.96$ and $A_V = 1.65$ mag. Using our estimate $E(B-V)_{host} = 1.22$ mag, we obtain the ratio of total-to-selective extinction $R_V = A_V/E(B-V) = 1.35$, in good agreement with the results of Foley et al. (2014).

This number is much smaller than the typical galactic value of 3.1, but close to the values found for another heavily reddened type Ia SNe (Wang et al., 2008).

4. Search for microvariability

Typical photometric monitoring of SNe consists of a single or few observations per night, so the short-timescale and low-amplitude variability remains poorly studied. Bonanos & Boumis (2016) reported evidence for microvariability in the optical light curve of SN 2014J. They obtained high-precision photometry in the B, V bands with a cadence of 2 min for about 8 hours per night during 4 consecutive nights at the phase ~ 16 days past maximum, and reported statistically significant detection of microvariability at the level of 0.02–0.05 mag with characteristic time 15–60 min on all nights.

We carried out photometric monitoring of SN 2014J at the A100 telescope during 6 nights from February 8 until March 3, 2014. Series of images in the B, V, R bands were obtained with exposure times of 60, 40, and 30 sec, the time lapse between consequent exposures in one filter was 3.5 min. The longest monitoring period was on the night of February 8/9, when it lasted for 7 hours, on the night February 9/10 observations lasted 5.8 hours and on the other nights monitoring continued for 3–1.3 hours.

We performed aperture photometry of SN relative to local standard stars 1 and 2 (S1, S2). Unfortunately, star 1 was overexposed on many frames in the V, R bands, and star 2 was often out of the field of view.

Typical photometric errors are 0.001–0.002 mag for the stars S1, S2 in all bands; for the SN the errors are about 0.002–0.003 mag in the V, R bands, for the B band they are 0.003–0.004 mag for the first nights in February, but increase to 0.015–0.02 mag for the nights in March.

Fig. 7 shows the data for the night February 8/9.

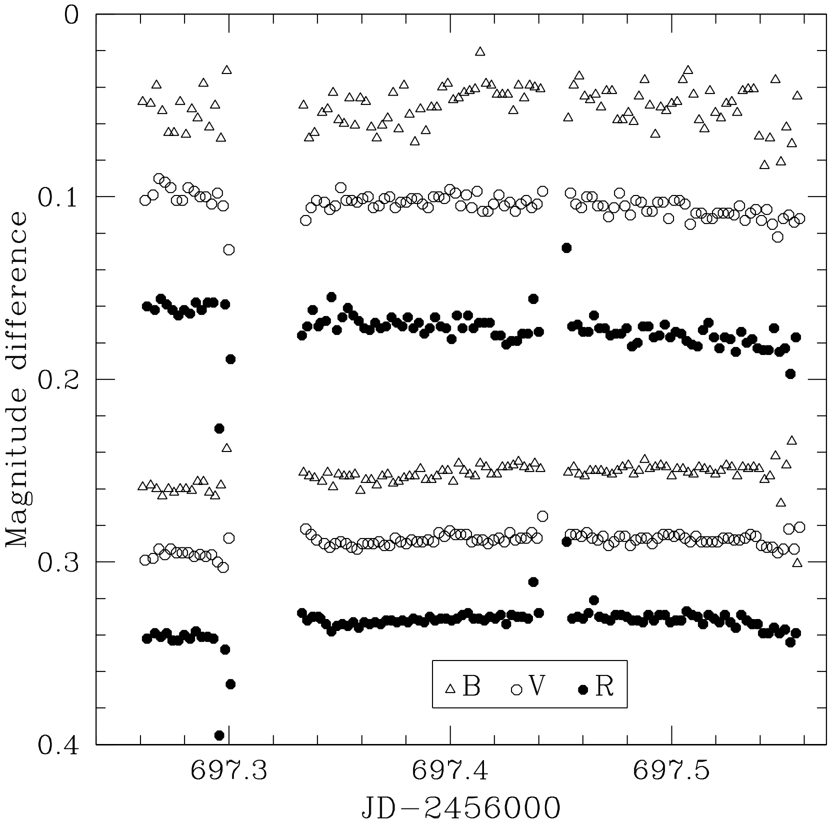

Figure 7. Results of monitoring of SN 2014J for the night February 8/9. 3 upper rows: magnitude differences Δ(SN-S1), 3 lower rows: magnitude differences Δ(S2-S1). The data were shifted vertically for clarity.

On the night February 8/9 the observations were interrupted by clouds, this is the reason for breaks in the monitoring and large magnitude deviations near the breaks.

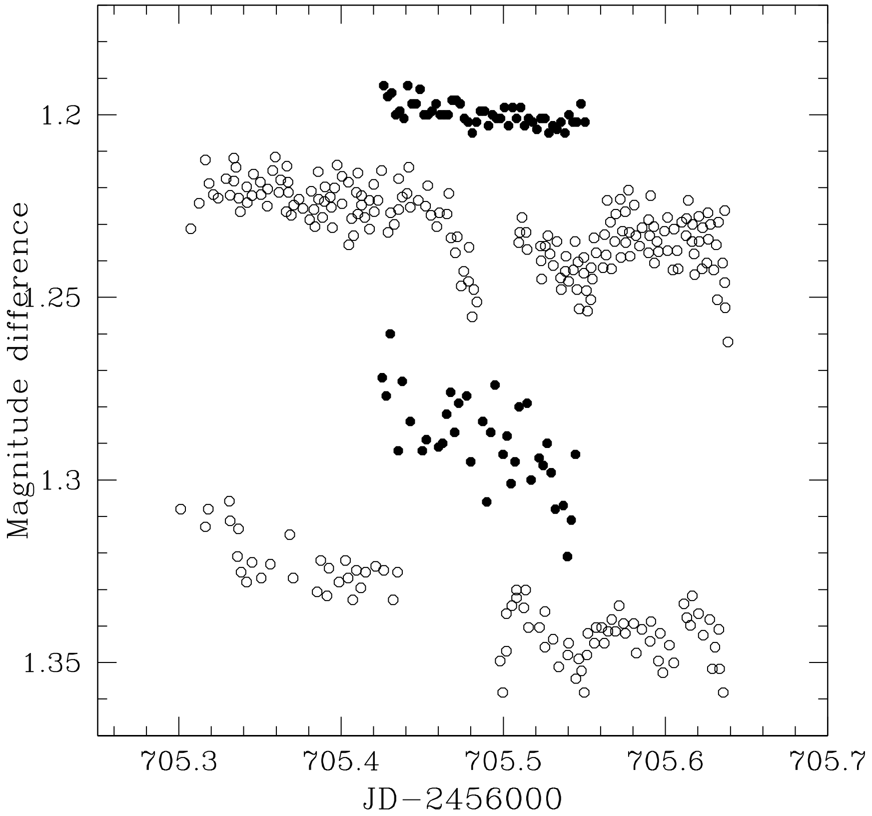

Figure 8. Results of monitoring of SN 2014J for the night February 16/17. Dots show our data, circles present the results by Bonanos & Boumis (2016). The magnitude differences Δ(S1-SN) are shown for the *V*-band in two upper rows, and for the *B*-band in two lower rows. The data were shifted vertically for clarity.

The differences of instrumental magnitudes Δ(S1-SN), Δ(S2-SN) were approximated by a first-order polynomial, and the regression coefficients and the standard deviations σ were calculated. The same procedure was applied to the magnitude differences of stars S1 and S2.

The minimal value of standard deviations σ(S1-SN) and σ(S2-SN) is 0.009 mag in the *B* band and 0.003 mag in the *V*, *R*-bands. On the nights when both stars 1 and 2 were measured, σ(S1-S2) was never significantly less than σ(S1-SN) and σ(S2-SN) for the *V*- and *R*-bands. Besides, no quasiperiodical SN brightness variations can be noticed on the plots of Δ(S1-SN) and Δ(S2-SN) versus time.

On the night February 16/17 monitoring was carried out at A100 and by Bonanos & Boumis (2016). Fig. 8 shows the comparison of results. Our observations do not confirm the dimming of SN in the V-band at JD 2456705.48 and 2456705.54, noticed by Bonanos & Boumis (2016).

We conclude that our observations do not confirm the existence of microvariability of SN 2014J with the amplitude and characteristic time reported by Bonanos & Boumis (2016).

5. Spectra

The spectra of SN 2014J obtained at the 2.6-meter telescope of CrAO are shown in Fig. 9, and those collected at the N600 and N100 telescopes are presented in Fig. 10.

The spectral evolution is typical for SN Ia, and the results are in good agreement with the data from Srivastav et al. (2016), Kawabata et al. (2014), Marion et al. (2015), and Bikmaev et al. (2015). The expansion velocities from the absorption features of the early spectra, obtained at the 2.6-meter telescope, were calculated by Tsvetkov et al. (2014). We used the radial velocity of the galaxy M82 v_{hel}=203 km s^{-1} to correct the observed shift of the lines, but Bikmaev et al. (2015) took into account the rotation of the galaxy and obtained a smaller radial velocity, v_{hel}=111 km s^{-1}, for the site of the SN. Using this value and measuring also the spectrum obtained at SAO, we calculate the following expansion velocities for the SiIIλ6355 line: 11700, 11510, and 10750 km s^{-1} for phases 2, 5 and 31 days after the maximum, respectively. These results are in good agreement with the data from Marion et al. (2015), Kawabata et al. (2014), and Srivastav et al. (2016), and they confirm that SN 2014J is located at the border of the Normal Velocity and High Velocity groups of SNe Ia (Wang et al., 2009a), in the Low Velocity Gradient subclass (Benetti et al., 2005).

The nebular spectra at phase $>$ 100 days are dominated by emission features of [FeIII]λ4071, [FeII]λ5159,5261 and NaI/[CoIII] features near 5900Å. We measured the velocity of the [FeIII]λ4071 emission feature and found the following values: -3000, -2280, -1630, and -110 km s^{-1} for phases 96, 124, 147, and 350 days after the maximum, respectively. We confirm the evolution of the redshift for this line, but our velocities are smaller than those obtained by Srivastav et al. (2016).

The strong interstellar NaI line is a characteristic feature of the spectra, with equivalent width 5.8 Å. The relation $E(B-V) = 0.16EW(\mathrm{NaI})$ (Turatto et al., 2003) gives $E(B-V) = 0.93$ mag. We consider this reasonable agreement with the value of $E(B-V)$ determined from the comparison of colour curves, taking into account the low correlation degree of this relation (Poznanski et al., 2011).

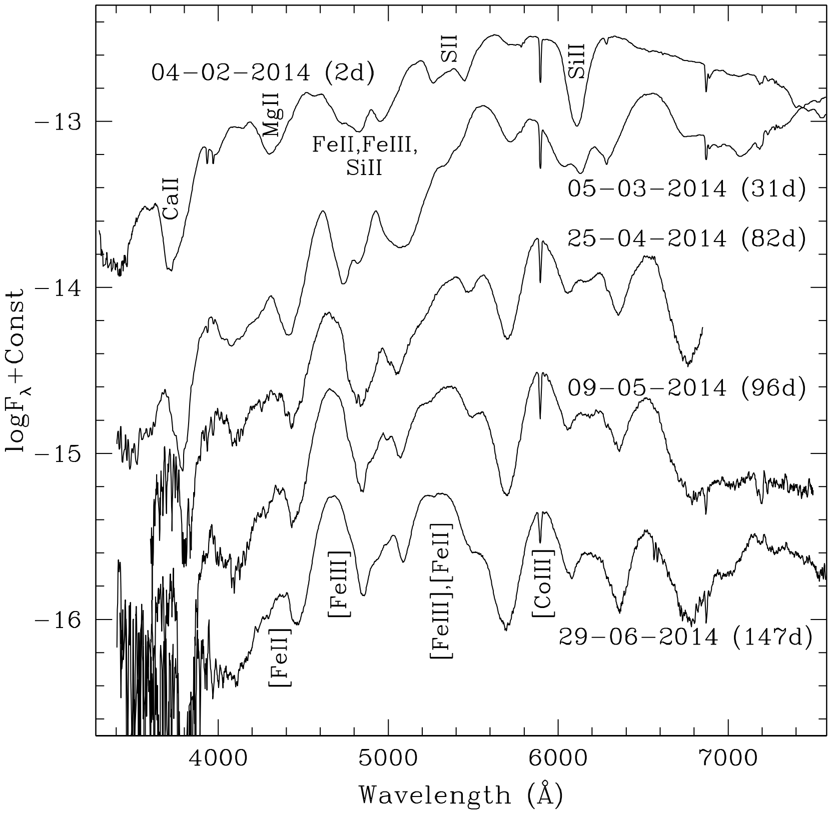

Figure 9. Spectra of SN 2014J collected at the 2.6-m Shajn telescope of CrAO. The date and phase past the B-band maximum are plotted near each spectrum.

6. Conclusions

We present the light and colour curves of SN 2014J spanning the phase interval from −8 to +416 days since the B-band maximum, and 9 spectra covering the period 2–350 days after the maximum. The light and colour curves are typical for SNe Ia, with a normal decline rate $\Delta m_{15}(B) = 1.08$. The interstellar extinction in the parent galaxy is very high, with $E(B-V)_{host} = 1.22$ and $R_V = 1.36$. The comparison of photometric data sets from 5 works reveals significant differences, especially for the U and B-bands, and for the period when the SN reached its maximum red colour.

The continuous photometric monitoring of SN 2014J on 6 nights does not reveal microvariability with the amplitude and characteristic time reported by

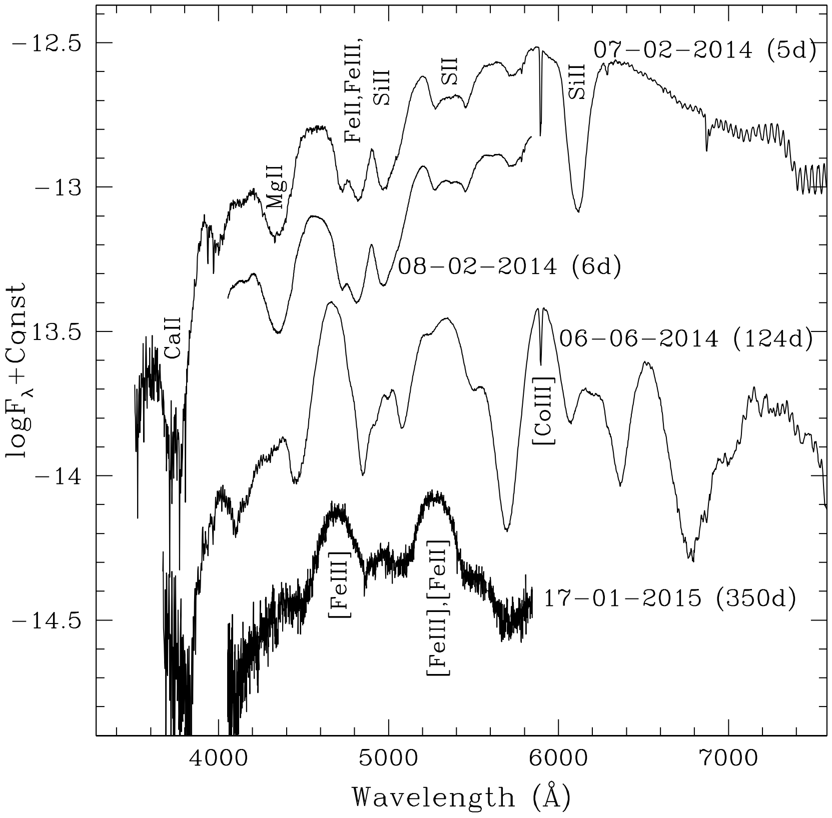

Figure 10. Spectra of SN 2014J acquired at the N100 (07-02-2014) and N600 (3 other spectra) telescopes of SAO.

Bonanos & Boumis (2016).

The spectral features are the same as for normal SNe Ia, the velocity evolution places SN 2014J at the border of the Normal Velocity and High Velocity groups, in the Low Velocity Gradient subclass. At the nebular stage we reveal the blue shift of [FeIII]λ4701 emission, which decreases with time.

Acknowledgements

The work of D.Tsvetkov was partly supported by the Russian Science Foundation Grant No. 16-12-10519.

The work of S.Shugarov was partly supported by Grants VEGA 2/0008/17 and APVV-15-0458.

This study was partly supported by the scholarship of the Slovak Academic Information Agency and by the Russian Science Foundation Grant No. 14-12-00146.

This study was also supported by the Committee on Science of the Ministry of Education and Science of the Republic of Kazakhstan (project no. BR05236322).

The authors are grateful to Savchenko S.S., Larionov V.M., Grishina T.S., Morozova D.A., Kopatskaya E.N., Larionova L.V., Borman G.A., who carried out some of the observations.

References

Amanullah, R., Goobar, A., Johansson, J., et al., The Peculiar Extinction Law of SN 2014J Measured with the Hubble Space Telescope. 2014, *Astrophys. J., Lett.*, **788**, L21, DOI: 10.1088/2041-8205/788/2/L21

Ashall, C., Mazzali, P., Bersier, D., et al., Photometric and spectroscopic observations, and abundance tomography modelling of the Type Ia supernova SN 2014J located in M82. 2014, *Mon. Not. R. Astron. Soc.*, **445**, 4427, DOI: 10.1093/mnras/stu1995

Astier, P., Guy, J., Regnault, N., et al., The Supernova Legacy Survey: measurement of Ω_M, Ω and w from the first year data set. 2006, *Astron. Astrophys.*, **447**, 31, DOI: 10.1051/0004-6361:20054185

Benetti, S., Cappellaro, E., Mazzali, P. A., et al., The Diversity of Type Ia Supernovae: Evidence for Systematics? 2005, *Astrophys. J.*, **623**, 1011, DOI: 10.1086/428608

Benetti, S., Meikle, P., Stehle, M., et al., Supernova 2002bo: inadequacy of the single parameter description. 2004, *Mon. Not. R. Astron. Soc.*, **348**, 261, DOI: 10.1111/j.1365-2966.2004.07357.x

Bikmaev, I. F., Chugai, N. N., Sunyaev, R. A., et al., Type Ia supernovae 2014J and 2011fe at the nebular phase. 2015, *Astronomy Letters*, **41**, 785, DOI: 10.1134/S1063773715120014

Bonanos, A. Z. & Boumis, P., Evidence for rapid variability in the optical light curve of the Type Ia SN 2014J. 2016, *Astron. Astrophys.*, **585**, A19, DOI: 10.1051/0004-6361/201425412

Denisenko, D., Gorbovskoy, E., Lipunov, V., et al., MASTER-Net Prediscovery and Follow-up Observations of SN 2014J in M82. 2014, *The Astronomer's Telegram*, **5795**

Foley, R. J., Fox, O. D., McCully, C., et al., Extensive HST ultraviolet spectra and multiwavelength observations of SN 2014J in M82 indicate reddening and circumstellar scattering by typical dust. 2014, *Mon. Not. R. Astron. Soc.*, **443**, 2887, DOI: 10.1093/mnras/stu1378

Gerke, J. R., Kochanek, C. S., & Stanek, K. Z., LBT R-band Variability Limit for the Progenitor of SN 2014J. 2014, *The Astronomer's Telegram*, **5808**

Goobar, A., Johansson, J., Amanullah, R., et al., The Rise of SN 2014J in the Nearby Galaxy M82. 2014, *Astrophys. J., Lett.*, **784**, L12, DOI: 10.1088/2041-8205/784/1/L12

Goobar, A., Kromer, M., Siverd, R., et al., Constraints on the Origin of the First Light from SN 2014J. 2015, *Astrophys. J.*, **799**, 106, DOI: 10.1088/0004-637X/799/1/106

Itagaki, K., Kaneda, H., Yamaoka, H., et al., Supernova 2014J in M82 = Psn J09554214+6940260. 2014, *Central Bureau Electronic Telegrams*, **3792**

Karachentsev, I. D. & Kashibadze, O. G., Masses of the local group and of the M81 group estimated from distortions in the local velocity field. 2006, *Astrophysics*, **49**, 3, DOI: 10.1007/s10511-006-0002-6

Kawabata, K. S., Akitaya, H., Yamanaka, M., et al., Optical and Near-infrared Polarimetry of Highly Reddened Type Ia Supernova 2014J: Peculiar Properties of Dust in M82. 2014, *Astrophys. J., Lett.*, **795**, L4, DOI: 10.1088/2041-8205/795/1/L4

Kessler, R., Becker, A. C., Cinabro, D., et al., First-Year Sloan Digital Sky Survey-II Supernova Results: Hubble Diagram and Cosmological Parameters. 2009, *Astrophys. J., Suppl.*, **185**, 32, DOI: 10.1088/0067-0049/185/1/32

Marion, G. H., Sand, D. J., Hsiao, E. Y., et al., Early Observations and Analysis of the Type Ia SN 2014J in M82. 2015, *Astrophys. J.*, **798**, 39, DOI: 10.1088/0004-637X/798/1/39

Phillips, M. M., The absolute magnitudes of Type IA supernovae. 1993, *Astrophys. J., Lett.*, **413**, L105, DOI: 10.1086/186970

Phillips, M. M., Lira, P., Suntzeff, N. B., et al., The Reddening-Free Decline Rate Versus Luminosity Relationship for Type IA Supernovae. 1999, *Astron. J.*, **118**, 1766, DOI: 10.1086/301032

Poznanski, D., Ganeshalingam, M., Silverman, J. M., & Filippenko, A. V., Low-resolution sodium D absorption is a bad proxy for extinction. 2011, *Mon. Not. R. Astron. Soc.*, **415**, L81, DOI: 10.1111/j.1745-3933.2011.01084.x

Prieto, J. L., Rest, A., & Suntzeff, N. B., A New Method to Calibrate the Magnitudes of Type Ia Supernovae at Maximum Light. 2006, *Astrophys. J.*, **647**, 501, DOI: 10.1086/504307

Pskovskii, I. P., Light curves, color curves, and expansion velocities of Type I supernovae as functions of the rate of brightness decline. 1977, *Astron. Zh.*, **54**, 1188

Richmond, M. W., Treffers, R. R., Filippenko, A. V., & Paik, Y., UBVRI Photometry of SN 1993J in M81: Days 3 to 365. 1996, *Astron. J.*, **112**, 732, DOI: 10.1086/118048

Riess, A. G., Filippenko, A. V., Challis, P., et al., Observational Evidence from Supernovae for an Accelerating Universe and a Cosmological Constant. 1998, *Astron. J.*, **116**, 1009, DOI: 10.1086/300499

Schlafly, E. F. & Finkbeiner, D. P., Measuring Reddening with Sloan Digital Sky Survey Stellar Spectra and Recalibrating SFD. 2011, *Astrophys. J.*, **737**, 103, DOI: 10.1088/0004-637X/737/2/103

Srivastav, S., Ninan, J. P., Kumar, B., et al., Optical and NIR observations of the nearby type Ia supernova SN 2014J. 2016, *Mon. Not. R. Astron. Soc.*, **457**, 1000, DOI: 10.1093/mnras/stw039

Stanishev, V., Goobar, A., Benetti, S., et al., SN 2003du: 480 days in the life of a normal type Ia supernova. 2007, *Astron. Astrophys.*, **469**, 645, DOI: 10.1051/0004-6361:20066020

Stritzinger, M., Hamuy, M., Suntzeff, N. B., et al., Optical Photometry of the Type Ia Supernova 1999ee and the Type Ib/c Supernova 1999ex in IC 5179. 2002, *Astron. J.*, **124**, 2100, DOI: 10.1086/342544

Tsvetkov, D. Y., Metlov, V. G., Shugarov, S. Y., Tarasova, T. N., & Pavlyuk, N. N., Supernova 2014J at maximum light. 2014, *Contributions of the Astronomical Observatory Skalnate Pleso*, **44**, 67

Tsvetkov, D. Y., Shugarov, S. Y., Volkov, I. M., et al., Optical observations of SN 2011fe. 2013, *Contributions of the Astronomical Observatory Skalnate Pleso*, **43**, 94

Turatto, M., Benetti, S., & Cappellaro, E., Variety in Supernovae. 2003, in *From Twilight to Highlight: The Physics of Supernovae*, ed. W. Hillebrandt & B. Leibundgut, 200

Wang, X., Filippenko, A. V., Ganeshalingam, M., et al., Improved Distances to Type Ia Supernovae with Two Spectroscopic Subclasses. 2009a, *Astrophys. J., Lett.*, **699**, L139, DOI: 10.1088/0004-637X/699/2/L139

Wang, X., Li, W., Filippenko, A. V., et al., The Golden Standard Type Ia Supernova 2005cf: Observations from the Ultraviolet to the Near-Infrared Wavebands. 2009b, *Astrophys. J.*, **697**, 380, DOI: 10.1088/0004-637X/697/1/380

Wang, X., Li, W., Filippenko, A. V., et al., Optical and Near-Infrared Observations of the Highly Reddened, Rapidly Expanding Type Ia Supernova SN 2006X in M100. 2008, *Astrophys. J.*, **675**, 626, DOI: 10.1086/526413

Zheng, W., Shivvers, I., Filippenko, A. V., et al., Estimating the First-light Time of the Type Ia Supernova 2014J in M82. 2014, *Astrophys. J., Lett.*, **783**, L24, DOI: 10.1088/2041-8205/783/1/L24

Contrib. Astron. Obs. Skalnaté Pleso **48**, 536 – 553, (2018)

Absolute parameters and period variation in a semidetached eclipsing variable V2247 Cyg

M.A. Burlak[1], **I.M. Volkov**[1,2] **and N.P. Ikonnikova**[1]

[1] *Sternberg Astronomical Institute, Lomonosov Moscow State University, Universitetskij Ave. 13, 119992 Moscow, Russia, (E-mail: marina.burlak@gmail.com,ikonnikova@gmail.com)*

[2] *Institute of Astronomy of the Russian Academy of Sciences, 48 Pyatnitskaya street, 119017 Moscow,*
Russia, (E-mail: hwp@yandex.ru)

Received: May 9, 2018; Accepted: June 22, 2018

Abstract. We aim to determine the absolute parameters of the components of a poorly studied Algol-type eclipsing binary V2247 Cyg. The data analysis is based on our numerous precise $UBVRcIc$ photometric observations and low resolution spectra. The photometric solution reveals a semi-detached configuration with a less-massive component filling its Roche lobe. The mass ratio, inclination, effective temperatures, and fractional radii were determined. Masses and radii of the components were obtained by a non-direct method. The Eclipse Time Variation (ETV) diagram revealed the period changes.

Key words: stars: binaries: eclipsing – stars: binaries: close – stars: interstellar reddening – stars: fundamental parameters

1. Introduction

Algol-type stars (EA) are eclipsing binaries consisting of spherical or ellipsoidal components and characterized by light curves (LCs) in which it is possible to specify the beginning and the end of eclipses. Algols are detached if both components are inside corresponding Roche lobes and semi-detached if one of the components fills its Roche lobe and loses matter. If the light changes between eclipses due to the gravitational deformation, we can estimate the mass ratio of the components without involving spectral studies. The analysis of multicolour LCs of Algols (EA) provides absolute parameters for their components which make possible clarifying the evolutionary status of the eclipsing binary.

The star BD +33 4035 V=10.9 mag was designated as V2247 Cyg (EA) in the 76th name-list of variable stars, Kazarovets et al. (2001), based on a private communication of N.E. Kurochkin and V.P. Goranskij, 1999, hereinafter KG. Due to the lack of data on the spectroscopic orbit of the object, we estimated the absolute parameters such as semi-major axes, radii and masses by the non-direct method described in Volkov et al. (2017). The precision of these values is not better than 10 percents, but it is good enough to find out that the location of the components on the diagrams given at the end of this article coincides with that of other binaries with well known parameters. Another aim of this work is to construct an ETV diagram for the star using our own and archive observations and to interpret the orbital period long-term change first found in this study.

2. Observations and data reduction

***UBVRcIc* photometry**. The main set of *UBVRcIc* observations of V2247 Cyg was obtained in 2013-2017 at the Crimean station of the Sternberg Astronomical Institute (SAI) with the 0.5-m $f/4$ Maksutov telescope (AZT-5) equipped with a CCD camera Apogee Alta U16M. All reductions and aperture photometry were made using the MaximDL software. The observational data were reduced to the standard Johnson-Cousins photometric system according to the following linear formulae:

$$\begin{gathered}
U = U_{inst} + 0.135((U_{inst} - B_{inst}) - (U_{st} - B_{st}))- \\
-0.007((B_{inst} - V_{inst}) - (B_{st} - V_{st})), \\
B = B_{inst} - 0.039((B_{inst} - V_{inst}) - (B_{st} - V_{st})), \\
V = V_{inst} + 0.088((B_{inst} - V_{inst}) - (B_{st} - V_{st})), \\
Rc = Rc_{inst} - 0.043((B_{inst} - Rc_{inst}) - (B_{st} - Rc_{st})), \\
Ic = Ic_{inst} - 0.063((B_{inst} - Rc_{inst}) - (B_{st} - Rc_{st})),
\end{gathered} \tag{1}$$

where index *inst* represents instrumental magnitudes of the observed star and *st* refers to the magnitudes of the standard star. The reduction coefficients were obtained by averaging the results of our observations of the standard area PG1633+099 of Landolt (1992) and observations of M67 performed by D.Yu. Tsvetkov.

The *UBVRIRc* CCD photometer equipped with a VersArray 512UV designed by one of the authors was used to make a calibration of the star in the standard Johnson-Cousins system on August 11, 2017. An equatorial standard GSC 543 227 was observed, whose *UBV* magnitudes were taken from Landolt (2009) and *RI* from Moffett & Barnes (1979), where the star was designated as 113 466. The observations were carried out with a Zeiss-600 reflector located at Mt. Koshka, Crimean Astrophysical Observatory(CrAO).

Photoelectric observations. The 0.6-m Zeiss $f/12.5$ Cassegrain telescope installed at the Crimean station of SAI equipped with the *UBV* photometer with a photomultiplier EMI 9789 (PMT), constructed by Lyutyj (1971), was used to get full *UBV* LCs. This photometer has an instrumental system *U* much closer to that of Johnson than AZT-5 which has glass elements in its optical path such as a meniscus and a corrector. So we used these observations to check our AZT-5 *U*-observations and found good coincidence.

For both sets of observations with AZT-5 and PMT the only reference star GSC 2695 1362(V_{st}=11.24, $(B-V)_{st}$=0.40) was used. No variability of the star was detected during the whole period of the observations.

The log of $UBVRcIc$ and UBV observations is given in Table 1. All original data can be found in a suitable computer form on-line at *http://www.astro.sk/caosp/Eedition/FullTexts/vol48no4/pp536-553.dat/*.

Table 1. Log of photometric observations.

Year	JD 2400000+...	N	System	Telescope
2013	56492-56495	1401	V	AZT-5, SAI
2014	56849-56857	2675	$UBVRcIc$	AZT-5, SAI
2015	57196-57240	5174	$UBVRcIc$	AZT-5, SAI
2017	57934-57980	2820	$UBVRcIc$	AZT-5, SAI
2017	57979-57994	25	UBV	PMT, SAI

Spectral observations. Low-resolution spectra of V2247 Cyg were obtained at the 1.25-m reflector of the SAI Crimean station. We used a diffraction spectrograph with a 600 lines/mm grating. The slit width was $4''$. The detector was an ST–402 CCD (765 × 510 pixels of $9 \times 9\mu$m). The spectral resolution (FWHM) was 7.4 Å. The spectra cover the wavelength interval from 3900 to 7200 Å. V2247 Cyg was observed on July 21, 30, August 27, and October 12, 2017.

Photographic observations. One extra timing of the primary minimum was obtained from an unpublished study of KG, who measured the star's magnitudes using 165 photographic plates of the SAI archive and derived a correct period of eclipses by the Lafler-Kinman method, Lafler & Kinman (1965), $P = 1^d.254861$. These data one can find in the card catalogue of SAI.

The system is listed in the catalogues of eclipsing stars of Malkov et al. (2006) and Avvakumova et al. (2013) which contain no ephemeris for the object. Otero (2008) derived a period of $P = 1^d.25486$ for the system, which perfectly coincides with the KG value.

3. Colour indices, spectra and determination of temperatures of the components

The most important parameters for the current analysis are the temperatures of the components that can be found in the following way. The colour indices of the light loss in the primary and secondary minima are calculated directly from the LCs in different passbands with no additional assumptions. Observed colour indices of the primary and secondary components are dereddened using a $(U-B),(B-V)$ two-colour diagram, see Fig. 1, $E(U-B)/E(B-V) = 0.710$ was accepted for the B5 spectral class from Table 11 in Straižys (1992). The colour indices calculated this way are applied to determine the temperatures of the components with the help of well-known calibrations.

$$\begin{gathered}\text{Primary}: (U-B)_0 = -0.689 \pm 0.015 (B-V)_0 = -0.202 \pm 0.010, \\ E(B-V) = 0.290 \pm 0.012. \\ \text{Secondary}: (U-B)_0 = -0.499 \pm 0.020 (B-V)_0 = -0.135 \pm 0.015, \\ E(B-V) = 0.288 \pm 0.014. \end{gathered} \tag{2}$$

For completeness we calculated mean colour indices in both minima and maxima of the LC. They are presented in Table 2. Keep in mind that these data are not dereddened.

Table 2. The observed colours in both minima and maxima.

Phase	$U-B$	$B-V$	$V-R_c$	R_c-I_c
0.0	-0.33	0.133	0.097	0.144
0.25	-0.43	0.102	0.072	0.115
0.5	-0.45	0.095	0.064	0.109
0.75	-0.42	0.111	0.069	0.116

We derived $T_1 = 17100$ K and $T_2 = 13000$ K from Flower (1996). Popper (1980) gives the temperatures that are 2000 K higher for the primary and 800 K higher for the secondary. We can see that the temperatures derived from the calibrations may have an uncertainty up to 1000 K for this range of temperatures. Equal values of interstellar reddening for both components can be obtained only if we attribute the third or fourth class of luminosity to the secondary component. We compared the results with the data from available surveys. A new review of interstellar extinction made by Green et al. (2015) gives $E(B-V) = 0.18 \pm 0.02$ for the distance to the star $d = 2040$ pc (see Table 4). From Schlafly & Finkbeiner (2011) and Schlegel et al. (1998) one can obtain $E(B-V) = 0.29 \pm 0.02$ for the total extinction along the given line of sight in the Galaxy. Taking into account the distance to the star we get $E(B-V) = 0.23 \pm 0.02$ from an equation in Bonifacio et al. (2000). The errors of these surveys seem to be understated. Nevertheless, we argue that such a discrepancy is not critical and we accept the value $E(B-V) = 0.29 \pm 0.01$ that follows from the photometry.

We obtained low-resolution spectra for the star in different phases of the orbital period. We did not detect any significant difference between the spectra obtained in the maximum and at the bottom of the primary minimum. The spectrum is dominated by the Balmer lines of hydrogen and lines of neutral helium. No lines of ionized helium are seen. The presence of He I lines in the absence of He II lines indicates the B spectral class (Gray & Corbally, 2009). The relative intensities of H I and He I lines alone do not allow the precise temperature determination due to possible helium abundance anomalies, which are

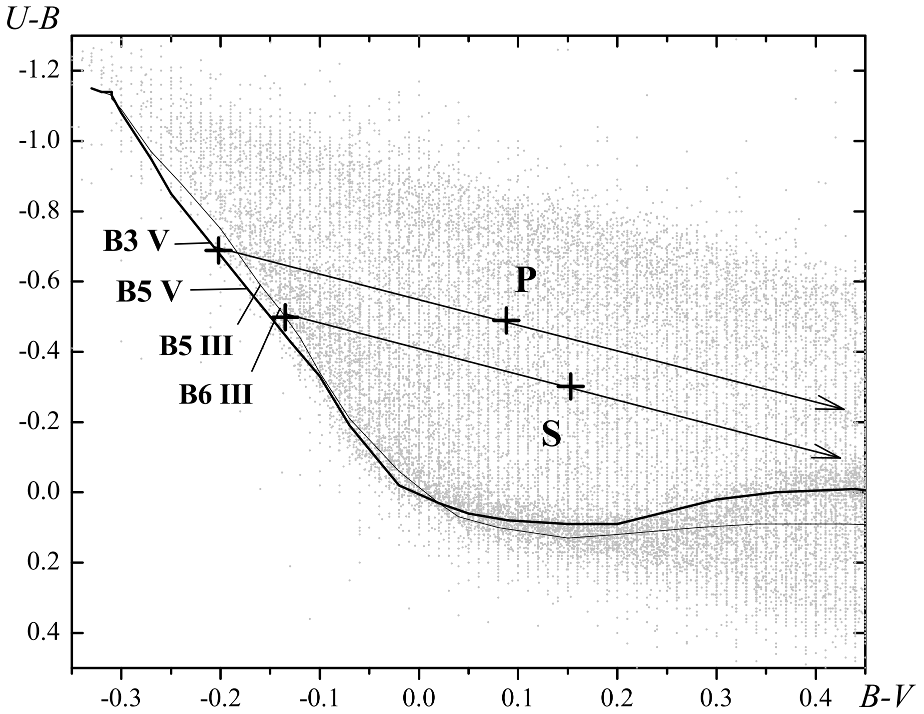

Figure 1. The $(U-B),(B-V)$ diagram. Arrows indicate the direction of interstellar reddening. The bold line stands for the standard luminosity class V sequence, and the thin one stands for that of class III, Straižys (1992). Grey points represent observations in the Johnson UBV system from the Mermilliod (1997) catalogue. Crosses mark observed and dereddened indices of the primary (P) and secondary (S) components.

not rare in B-class stars. The He I λ4471/Mg II λ4481 ratio may be of use for specifying the temperature of stars later than B3 and in our study it appeared very helpful as the lines of Si III and Si IV, which are weaker, could not be resolved. Besides, low spectral resolution and a low S/N ratio of our spectral data prevent a precise luminosity classification. The comparison with the stars of spectral classes between B3 and A0, and of luminosity classes from V to III, yields the best agreement for the spectral class B5 V. The uncertainty is about one subclass. The spectrum of V2247 Cyg is similar to that of 57 Cyg (B5 V) (Fig. 2). A B5 V-III spectrum corresponds to a temperature of 15 400 K according to the calibration of Straižys (1982), in good coincidence with photometric results.

In addition to H I and He I absorptions in the spectrum of V2247 Cyg, we identified prominent diffuse interstellar bands (DIBs) centered at λ5780 and

λ6284 and the strong interstellar NaI D doublet. The strengths of these lines in stellar spectra show a positive correlation with the observed extinction, though there is a significant dispersion about the mean relationship (Friedman et al., 2011), (Herbig, 1993). To estimate interstellar extinction, one needs to resolve Na I D1 and D2 lines, to measure their strengths separately, and to control the D2/D1 ratio, because the uncertainty is large at the higher Na column densities due to the line saturation. The low resolution of our spectra does not allow us to perform such a procedure. Similar problems arise if we intend to estimate extinction from the equivalent widths of DIBs: the DIB at λ6284 is blended with a telluric O_2 band consisting of several absorption lines which are not detectable with given resolution, and the DIB at λ5780 is too broad and shallow to be measured securely, given a low S/N ratio.

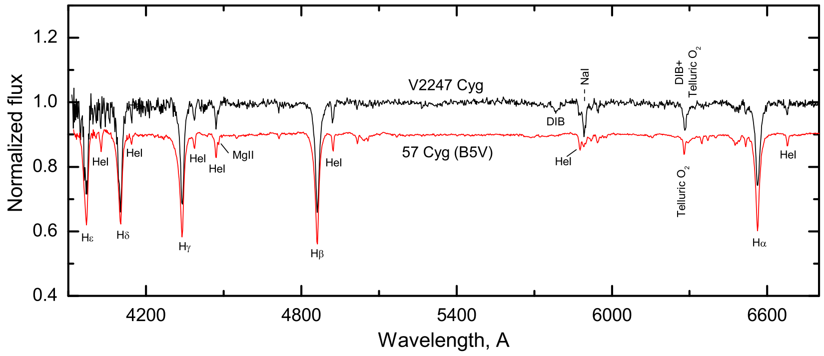

Figure 2. The spectra for V2247 Cyg and 57 Cyg normalized to the continuum, obtained on July 30, 2017. The spectrum for 57 Cyg is intentionally shifted along the vertical axis.

4. Light curves solution

The LCs of the binary show clear evidence for proximity effects, see Fig. 3. So, we used the PHOEBE program of Prša & Zwitter (2005) to analyze them. The best fit yielded a semidetached system with the secondary filling its Roche lobe. This agrees with the consideration inferred from our photometry that the secondary component has moved far enough in its evolution from the initial main sequence. We got an individual solution for each passband of AZT-5 observations and then repeated the procedure for less numerous PMT observations in 2017. All solutions led to similar parameters: the mass ratio q, inclination i, effective temperatures T, fractional radii r_1, r_2, and the potential Ω. Mean weighted values of the parameters are presented in Table 3. The solution of the LCs did not show any presence of a third light and it was assumed to be zero, $L_3 = 0$.

The temperatures of the components were included in solving LCs, as the values obtained from calibrations seemed to have discrepancies of up to 1000 K for the considered temperature range, see the previous section. We accepted a temperature of $T_1 = 17100$ K as the first approximation for the primary component. Solutions provided a confident minimum for the temperatures of the components, $T_1 = 16500$ K and $T_2 = 11500$ K, and these are 500 and 1500 K lower than it follows from photometric calibrations. The found temperatures correspond to the spectral types B4-5 V and B8 III-IV in the calibration of Straižys (1982).

Taking into account high accuracy and a large amount of observational data we included the albedo (A) of the secondary component and the gravity brightening coefficients (g) as varied parameters into the process of minimizing residuals. We found a shallow minimum for g_1=g_2=0.90 and A_2=0.8, but its reality is uncertain. So we assumed the theoretical values, see Table 3. The albedo of the primary component has a negligible effect on the shape of the LCs and was accepted from the PHOEBE of Prša & Zwitter (2005). The limb-darkening coefficients can be found from temperatures and gravitational accelerations of the components. The best results were obtained with a linear limb-darkening law. The coefficients were derived with the PHOEBE program according to van Hamme (1993). The solution is given in Table 3.

Table 3. Parameters derived from fitting the $UBVRcIc$ LCs.

Parameter	Primary	Secondary
i [°]	79.08 ± 0.04	
$q(M_2/M_1)$	0.812 ± 0.006	
T (K)	16500 ± 300	11450 ± 100
Sp	B4 V	B7 III-IV
BC (mag)	−1.461	−0.564
Ω	4.26 ± 0.02	2.51
A	0.6	0.6
g	1.0	1.0

Assuming a normal distribution for the residuals we get a mean error for an individual observational point in every spectral band:

$U - 0.042$ (1305 points), $B - 0.0107$ (2358 points), $V - 0.0099$ (3720 points), $Rc - 0.0100$ (2308 points), $Ic - 0.0133$ (2326 points).

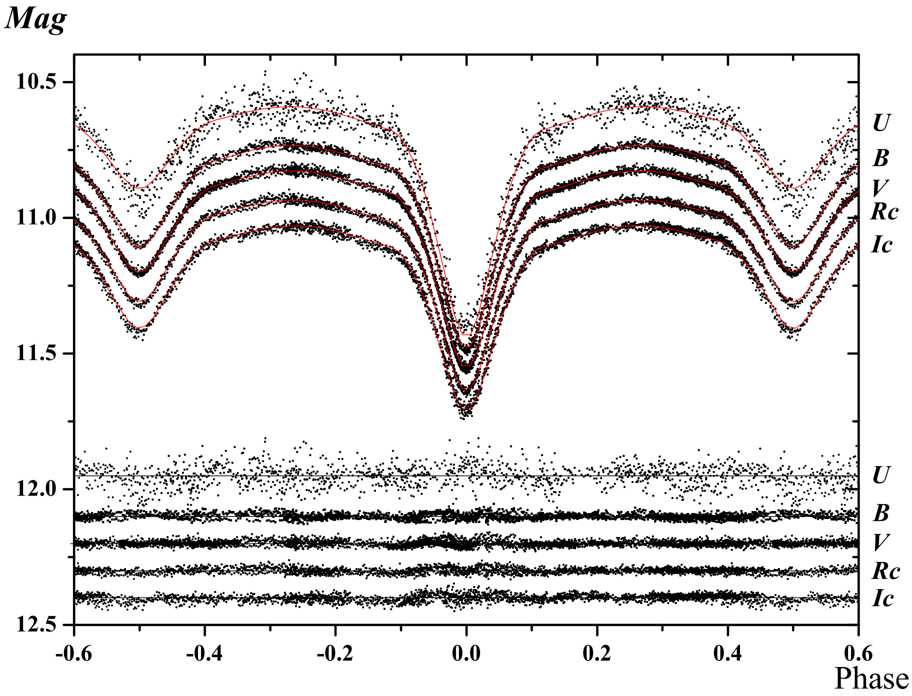

Figure 3. $UBVRcIc$ observations for V2247 Cyg. Red lines stand for the best fits. Residuals from the best fits are shown at the bottom of the picture.

Fig. 4 contains the phased colour curves for the star. The period was split into 120 intervals and the colour data were averaged within each interval. This plot is of interest as it demonstrates some asymmetry, especially in the $U - B$ colour index, which could be attributed to physical processes in the system.

Fig. 5 shows the $B - Rc$ phased colour curve for V2247 Cyg which best describes the tendency of the binary to get redder when approaching the secondary minimum. If there were the reflection effect, the object would get bluer.

5. Absolute parameters and ETV diagrams

We found the masses of the components by a non-direct method we used in Volkov et al. (2017). The method is based on the empirical mass-luminosity relation, the 3rd Kepler law, and the relation between the absolute and relative radii:

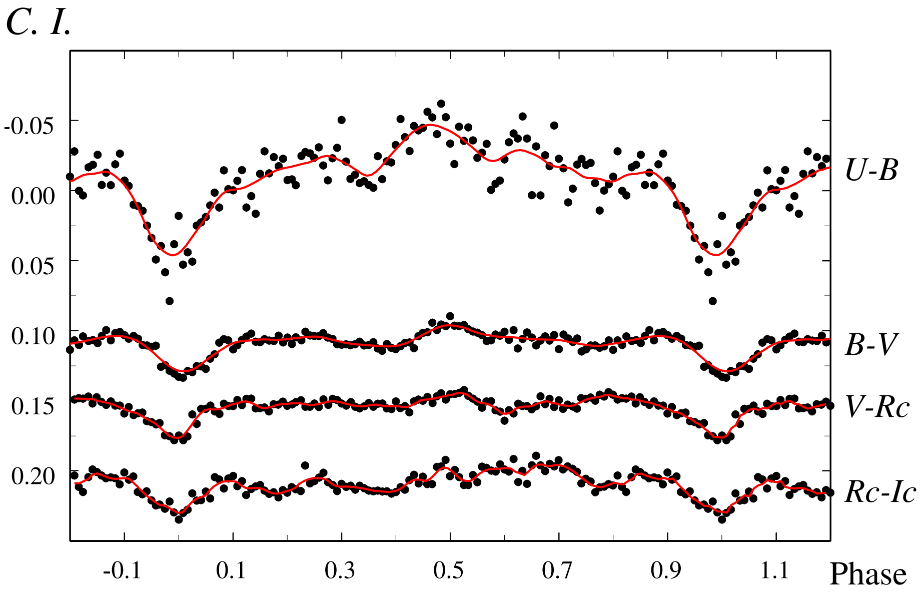

Figure 4. A plot showing colour indices (C.I.) phased with the current period. The Y-axis labels correspond to $B-V$. Other C.I. are shifted downwards, $U-B$ by 0.40, $V-Rc$ by 0.08 and $Rc-Ic$ by 0.09. Red lines are drawn by the Weighted Least Squares(WLS) method.

$$\begin{aligned}\log(L_1/L_\odot) &= 3.99\log(M_1/M_\odot),\\ a^3/P^2 &= M_1(1+q),\\ R_1 &= r_1 a.\end{aligned} \tag{3}$$

While the light curves solution provides a reliable q value for semidetached systems, see Table 3, the non-direct method yields $q = 0.81 \pm 0.01$, which is in perfect agreement with the value from the LCs solution. The absolute parameters of the system are presented in Table 4. Our photometric parallax, $\pi = 0.49 \pm 0.03$ mas, matches quite well the GAIA DR2 value, $\pi = 0.4310 \pm 0.0287$ mas, of Luri et al. (2018). We hope that with the use of these new GAIA data, temperature calibrations will be refined.

To derive precise minima times from photoelectric and CCD observations, we fitted the synthetic LCs, obtained during single overnight runs, by means of the PHOEBE program varying only the specific epoch. Sometimes, when only parts of the minimum were available for the close dates of observations, we compiled them into one minimum and assigned the acquired minimum time to the night with more numerous observations. In the case of simultaneous observations in several filters, the minima times were weighted and mean values were calculated.

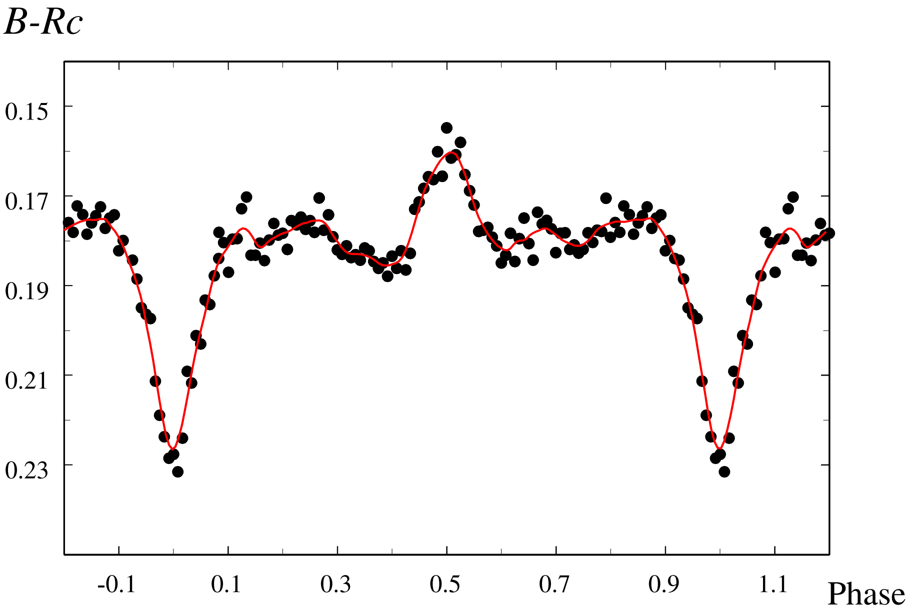

Figure 5. The $B - Rc$ colour index phased with the current period. The red line is drawn by the WLS method.

Table 4. The absolute parameters derived by the non-direct method.

Parameter	Primary	Secondary
M ($M_\odot$)	5.0 ± 0.2	4.05 ± 0.1
$q(M_2/M_1)$	0.81 ± 0.01	
R ($R_\odot$)	3.1 ± 0.2	3.8 ± 0.1
log L ($L_\odot$)	2.79 ± 0.05	2.42 ± 0.05
log g	4.17 ± 0.01	3.89 ± 0.01
a ($R_\odot$)	10.2 ± 0.4	
d [pc]	2040 ± 150	

The minima times are listed in Table 5, together with the already published ones. Primary and secondary minima times were used to construct an ETV diagram, see Fig. 6. One can see that the period of the system is changing: close to JD=2 456 000 it became shorter.

The $O - C$ residuals in the ETV diagram (Fig. 6) and in Table 5 were calculated using the linear ephemeris which is suitable for the modern epoch:

$$\text{HJD Min I} = 2456857.3783(2) + 1.2548450(3) \times E. \qquad (4)$$

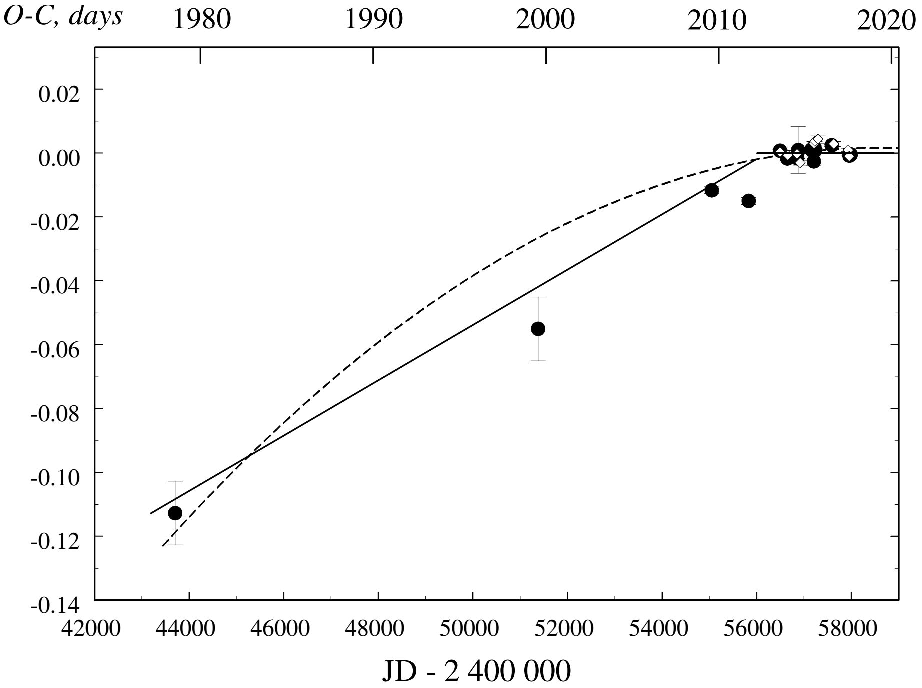

Figure 6. A plot showing the ETV diagram for V2247 Cyg, constructed using ephemeris (4). The circles represent primary minima, the diamonds – secondaries. The data are fitted by a parabolic law (6) – the dotted line, and linear laws (4) and (5) – solid straight lines.

The secondary component fills its Roche lobe and the mass transfer, or mass loss, might be responsible for the period change. Timings before JD2456000 satisfy the formula:

$$\text{HJD Min I } = 2456857.3808(6) + 1.2548564(4) \times E, \qquad (5)$$

which coincides with the KG and Otero (2008) within errors. The minima times in the ETV diagram can also be fitted by a parabola (a continuous period change), represented by the following ephemeris:

$$\text{HJDMin I } = 2456857.3768(3) + 1^d.2548481(9) \times E - 8.57(4) \cdot 10^{-10} \times E^2. \qquad (6)$$

The weights for the minima times were set equal to $1/\sigma^2$. Usually for such a configuration of the system one could expect mass transfer from the secondary component to the primary through the inner Lagrange point L_1. In this case there should be a gradual increase in the orbital period of the binary star. But we

Table 5. Times of minima for V2247 Cyg. The errors for the first two minima were not available and were set equal to the half of the least significant digit adduced by the authors.

HJD−2400000	Epoch	Residuals from linear ephemeris (4)	Residuals from parabolic fit (6)	Source
43706.49	-10480	−0.1127	0.0060	1
51378.67	-4366	−0.0550	−0.0285	2
55050.3899(11)	-1440	−0.0116	−0.0065	3
55833.4098(11)	-816	−0.0150	−0.0126	4
56493.4740(5)	-290	0.0008	0.0014	t.w., V
56495.3549(1)	-288.5	0.0003	0.0010	”
56650.3272(6)	-165	−0.0017	−0.0013	5
56657.2290(14)	-159.5	−0.0006	−0.0003	”
56855.4949(3)	-1.5	−0.0002	−0.0003	t.w., $UBVRcIc$
56857.3767(1)	0	−0.0016	−0.0017	”
56877.457(7)	16	0.0010	0.0009	6
56919.4892(8)	49.5	−0.0030	−0.0032	7
57158.5422(2)	240	0.0011	0.0005	”
57207.4775(14)	279	−0.0026	−0.0032	8
57212.5014(1)	283	0.0020	0.0013	t.w., $BVRcIc$
57214.3838(7)	284.5	0.0030	0.0024	7
57234.4620(1)	300.5	0.0037	0.0030	t.w., $UBVRcIc$
57236.3423(6)	302	0.0008	0.0001	t.w., U
57298.4598(13)	351.5	0.0044	0.0036	9
57586.4457(3)	581	0.0025	0.0013	7
57628.4825(8)	614.5	0.0029	0.0017	”
57938.4273(4)	861.5	0.0009	−0.0005	t.w., $UBVRcIc$
57958.5029(2)	877.5	−0.0010	−0.0024	”
57960.3863(1)	879	−0.0008	−0.0022	”
57990.5029(3)	903	−0.0004	−0.0019	t.w., UBV, PMT

Notes. 1 - KG; 2 - Otero (2008); 3 - Hubscher et al. (2010); 4 - Hubscher et al. (2013); 5 - Hubscher (2014); 6 - Hubscher & Lehmann (2015); 7 - Zasche et al. (2017); 8 - Hubscher (2016); 9 -Hubscher (2017); t.w. - this work.

are watching the opposite case – the period is decreasing. This means that a non-conservative mass loss from the secondary through the L_2 Lagrange point takes place. We can't rule out the abrupt period decrease close to JD =2456000. Fig. 7 presents the ETV diagram for the modern epoch on a large scale. We cannot say that the parabolic fit has any advantage comparing to the linear law. The linear fit explains old observations better than the parabola does, see Fig. 6. So

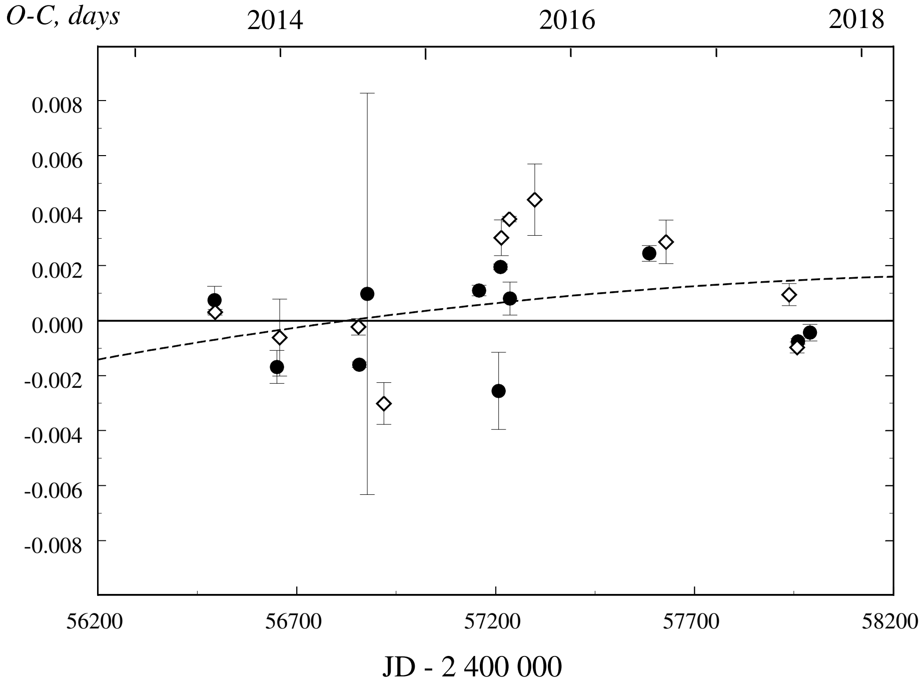

Figure 7. The ETV diagram for V2247 Cyg for the modern epoch on a large scale. The signs are the same as in Fig. 6. The parabolic and linear laws fit observations equally well.

we may suppose that the processes of mass loss and mass transfer in this system can occur episodically but not continuously. Some systematic difference is seen in the shape of the V light curve observed in 2013 comparing to LCs obtained in the 2014-2017 interval, i.e., the primary minimum was deeper by 0.01 in 2013. This difference may also be assigned to the processes mentioned above.

Figs. 8 and 9 show the location of the primary and secondary components in the HR diagram and $\log T - \log M$, $\log R - \log M$, $\log T - \log R$, and $\log L - \log M$ diagrams for V2247 Cyg as well as for 61 semidetached Algol binaries with well-determined absolute parameters (Ibanoğlu et al., 2006). While the position of the primary component is similar to that of other primaries, the secondary of V2247 Cyg lies near the border, or even outside, the region occupied by other secondaries. It's worth mentioning that, among 61 semidetached binaries listed in Ibanoğlu et al. (2006), none of the systems consists of two B-class stars. What makes V2247 Cyg unusual, when compared to other semidetached Algol-type binaries, is its higher mass and temperature of the secondary.

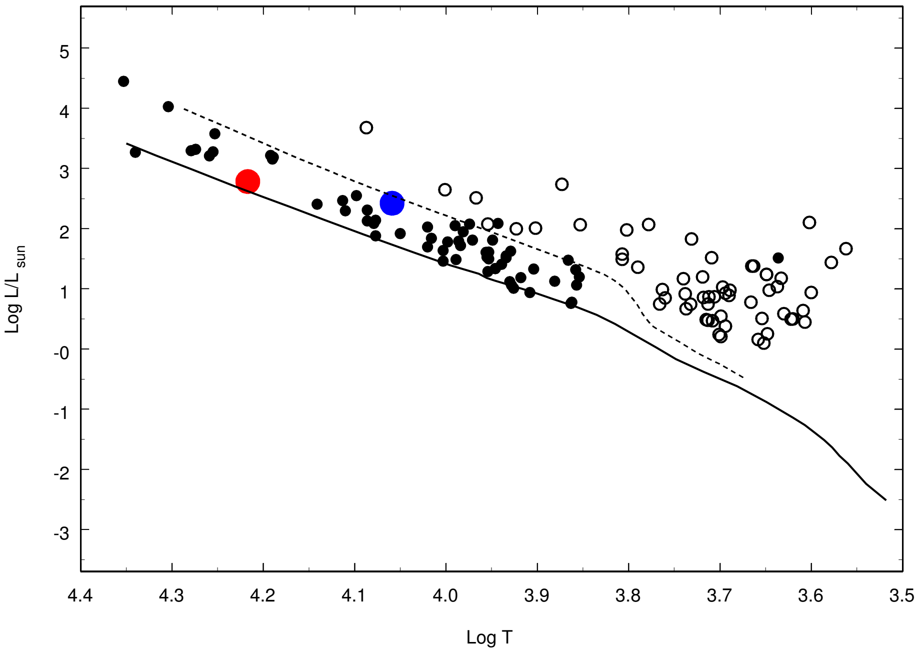

Figure 8. A plot showing the HR diagram for the primary (filled circles) and secondary (open circles) components of semidetached Algol binaries taken from Ibanoğlu et al. (2006). Solid and dashed lines represent the ZAMS and TAMS for solar chemical abundance (Girardi et al., 2000), respectively. We added the location of the primary (the red circle) and secondary (the blue circle) components of V2247 Cyg.

6. Conclusions

Using multicolour photometry we obtained reliable parameters for the Algol-type binary V2247 Cyg: colour indices, interstellar reddening, mass ratio, inclination, effective temperatures of the components, fractional radii, the potentials, as well as the albedo of the secondary and the gravity brightening coefficients. V2247 Cyg was found to be a semidetached system with the secondary filling its Roche lobe.

The B5III-V spectral type was ascribed to the low-resolution spectrum of V2247 Cyg.

Due to the lack of data on radial velocities, the masses of the components were computed by a non-direct method. The mass ratio derived this way is in excellent agreement with the value obtained through solving LCs.

The study of the ETV diagram enabled us to discover the orbital period decrease. It can be explained by a mass loss from the less massive secondary component.

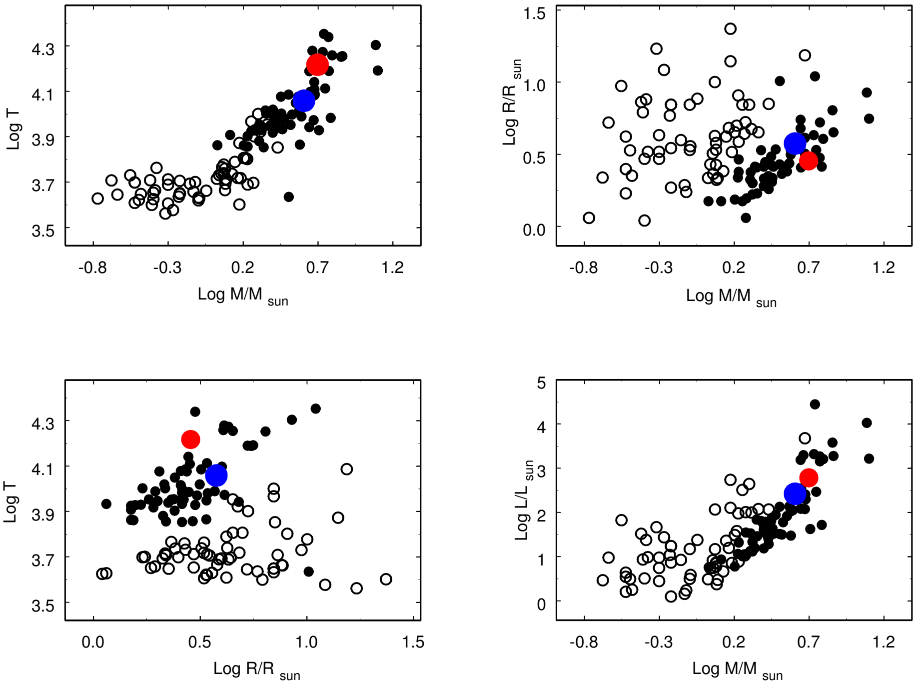

Figure 9. Various diagrams for semidetached Algol binaries taken from Ibanoğlu et al. (2006). Symbols are the same as in Fig. 8.

In the HR and $\log T - \log M$, $\log R - \log M$, $\log T - \log R$, and $\log L - \log M$ diagrams the primary component of V2247 Cyg lies well within the region occupied by the primaries of semidetached Algol-type binaries, whereas its secondary differs from other secondaries due to its higher mass and temperature.

We'd like to encourage high-resolution and high signal-to-noise spectroscopic observations of the system in order to determine the masses of the components from radial velocity curves.

Acknowledgements. This study was partly supported by the scholarship of the Slovak Academic Information Agency(IMV), RNF grant 14-12-00146 and RFBR grant 18-502-12025(IMV). We are grateful to professor N. N. Samus for providing access to the card catalogue of SAI, Dr. V.P. Goranskij for permission to use his data prior to publication and to an anonymous referee for important corrections.

References

Avvakumova, E. A., Malkov, O. Y., & Kniazev, A. Y., Eclipsing variables: Catalogue and classification. 2013, *Astronomische Nachrichten*, **334**, 860, DOI: 10.1002/asna.201311942

Bonifacio, P., Monai, S., & Beers, T. C., A Search for Stars of Very Low Metal Abundance. V. Photoelectric UBV Photometry of Metal-weak Candidates from the Northern HK Survey. 2000, *Astron. J.*, **120**, 2065, DOI: 10.1086/301566

Flower, P. J., Transformations from Theoretical Hertzsprung-Russell Diagrams to Color-Magnitude Diagrams: Effective Temperatures, B-V Colors, and Bolometric Corrections. 1996, *Astrophys. J.*, **469**, 355, DOI: 10.1086/177785

Friedman, S. D., York, D. G., McCall, B. J., et al., Studies of Diffuse Interstellar Bands V. Pairwise Correlations of Eight Strong DIBs and Neutral Hydrogen, Molecular Hydrogen, and Color Excess. 2011, *Astrophys. J.*, **727**, 33, DOI: 10.1088/0004-637X/727/1/33

Girardi, L., Bressan, A., Bertelli, G., & Chiosi, C., Evolutionary tracks and isochrones for low- and intermediate-mass stars: From 0.15 to 7 M_{sun}, and from Z=0.0004 to 0.03. 2000, *Astron. Astrophys., Suppl. Ser.*, **141**, 371, DOI: 10.1051/aas:2000126

Gray, R. O. & Corbally, J., C. 2009, *Stellar Spectral Classification*

Green, G. M., Schlafly, E. F., Finkbeiner, D. P., et al., A Three-dimensional Map of Milky Way Dust. 2015, *Astrophys. J.*, **810**, 25, DOI: 10.1088/0004-637X/810/1/25

Herbig, G. H., The diffuse interstellar bands. IX - Constraints on the identification. 1993, *Astrophys. J.*, **407**, 142, DOI: 10.1086/172500

Hubscher, J., BAV Results of observations - Photoelectric Minima of Selected Eclipsing Binaries and Maxima of Pulsating Stars. 2014, *Information Bulletin on Variable Stars*, **6118**

Hubscher, J., BAV-Results of observations - Photoelectric Minima of Selected Eclipsing Binaries. 2016, *Information Bulletin on Variable Stars*, **6157**

Hubscher, J., BAV-Results of observations - Photoelectric Minima of Selected Eclipsing Binaries and Maxima of Pulsating Stars. 2017, *Information Bulletin on Variable Stars*, **6196**, DOI: 10.22444/IBVS.6196

Hubscher, J., Braune, W., & Lehmann, P. B., BAV-Results of observations - Photoelectric Minima of Selected Eclipsing Binaries and Maxima of Pulsating Stars. 2013, *Information Bulletin on Variable Stars*, **6048**

Hubscher, J. & Lehmann, P. B., BAV-Results of observations - Photoelectric Minima of Selected Eclipsing Binaries and Maxima of Pulsating Stars. 2015, *Information Bulletin on Variable Stars*, **6149**

Hubscher, J., Lehmann, P. B., Monninger, G., Steinbach, H.-M., & Walter, F., BAV-Results of Observations - Photoelectric Minima of Selected Eclipsing Binaries and Maxima of Pulsating Stars. 2010, *Information Bulletin on Variable Stars*, **5941**

Ibanoğlu, C., Soydugan, F., Soydugan, E., & Dervişoğlu, A., Angular momentum evolution of Algol binaries. 2006, *Mon. Not. R. Astron. Soc.*, **373**, 435, DOI: 10.1111/j.1365-2966.2006.11052.x

Kazarovets, E. V., Samus, N. N., & Durlevich, O. V., The 76th Name-List of Variable Stars. 2001, *Information Bulletin on Variable Stars*, **5135**

Lafler, J. & Kinman, T. D., An RR Lyrae Star Survey with Ihe Lick 20-INCH Astrograph II. The Calculation of RR Lyrae Periods by Electronic Computer. 1965, *Astrophys. J. Suppl.*, **11**, 216, DOI: 10.1086/190116

Landolt, A. U., UBVRI photometric standard stars in the magnitude range 11.5-16.0 around the celestial equator. 1992, *Astron. J.*, **104**, 340, DOI: 10.1086/116242

Landolt, A. U., UBVRI Photometric Standard Stars Around the Celestial Equator: Updates and Additions. 2009, *Astron. J.*, **137**, 4186, DOI: 10.1088/0004-6256/137/5/4186

Luri, X., Brown, A. G., Sarro, L., et al., Gaia Data Release 2. Using Gaia parallaxes. 2018, *Astron. Astrophys.*, DOI: 10.1051/0004-6361/201832964

Lyutyj, V. M., Automatic electrophotometer with photon counting. 1971, *Soobshcheniya Gosudarstvennogo Astronomicheskogo Instituta*, **172**, 30

Malkov, O. Y., Oblak, E., Snegireva, E. A., & Torra, J., A catalogue of eclipsing variables. 2006, *Astron. Astrophys.*, **446**, 785, DOI: 10.1051/0004-6361:20053137

Mermilliod, J. C., VizieR Online Data Catalog: Homogeneous Means in the UBV System (Mermilliod 1991). 1997, *VizieR Online Data Catalog*, **2168**

Moffett, T. J. & Barnes, III, T. G., Equatorial UBVRI photoelectric sequences. 1979, *Astron. J.*, **84**, 627, DOI: 10.1086/112460

Otero, S. A., New and Confirmed Eclipsing Binaries In the ASAS-3 and NSVS Databases. 2008, *Open European Journal on Variable Stars*, **91**, 1

Popper, D. M., Stellar masses. 1980, *Ann. Rev. Astron. Astrophys.*, **18**, 115, DOI: 10.1146/annurev.aa.18.090180.000555

Prša, A. & Zwitter, T., A Computational Guide to Physics of Eclipsing Binaries. I. Demonstrations and Perspectives. 2005, *Astrophys. J.*, **628**, 426, DOI: 10.1086/430591

Schlafly, E. F. & Finkbeiner, D. P., Measuring Reddening with Sloan Digital Sky Survey Stellar Spectra and Recalibrating SFD. 2011, *Astrophys. J.*, **737**, 103, DOI: 10.1088/0004-637X/737/2/103

Schlegel, D. J., Finkbeiner, D. P., & Davis, M., Maps of Dust Infrared Emission for Use in Estimation of Reddening and Cosmic Microwave Background Radiation Foregrounds. 1998, *Astrophys. J.*, **500**, 525, DOI: 10.1086/305772

Straižys, V. 1982, *Metal-deficient stars, Institut Fiziki Akad. Nauk Litovskoj SSR, Mokslas, Vil'nyus*

Straižys, V. 1992, *Multicolor stellar photometry, Tucson : Pachart Pub. House*

van Hamme, W., New limb-darkening coefficients for modeling binary star light curves. 1993, *Astron. J.*, **106**, 2096, DOI: 10.1086/116788

Volkov, I. M., Chochol, D., Grygar, J., Mašek, M., & Juryšek, J., Orbital period changes in RW CrA, DX Vel and V0646 Cen. 2017, *Contributions of the Astronomical Observatory Skalnate Pleso*, **47**, 29

Zasche, P., Uhlar, R., Svoboda, P., et al., Collection of Minima of Eclipsing Binaries, part III. 2017, *Information Bulletin on Variable Stars*, **6204**, DOI: 10.22444/IBVS.6204

Contrib. Astron. Obs. Skalnaté Pleso **48**, 554 – 583, (2018)

Meteoroid stream and meteor showers of comet C/1964 N1. Part II

L. Neslušan[1] **and M. Hajduková, jr.**[2]

[1] *Astronomical Institute of the Slovak Academy of Sciences*
059 60 Tatranská Lomnica, The Slovak Republic, (E-mail: ne@ta3.sk)

[2] *Astronomical Institute of the Slovak Academy of Sciences, Interplanetary Matter Division, Dúbravská cesta 9, 845 04 Bratislava, The Slovak Republic*

Received: September 6, 2018; Accepted: October 9, 2018

Abstract. In this paper we give further, both graphical and tabular, information about our study of the meteor complex of the long-period comet C/1964 N1 (Ikeya). We found that the modeled stream of the comet approaches the Earth's orbit typically in four filaments that correspond to four showers. Their radiant areas are close to the apex of the Earth's motion around the Sun. We confirmed the generic relationship between the studied parent comet and July ξ-Arietids, #533. The comet is probably also the parent of ϵ-Geminids, #23. We suspect that there could be a relationship between the comet and ξ-Geminids, #718, though this relationship is rather uncertain. There are real counterparts of three of the predicted showers in the CAMS and SonotaCo databases.

Key words: Comets: individual: C/1964 N1 (Ikeya) – Meteorites, meteors, meteoroids

1. Introduction

In our previous paper (Neslušan & Hajduková, 2018, henceforth referred to as Paper I) we studied the meteoroid stream originating from the long-period comet C/1964 N1 (Ikeya). In the current paper we give tabular and further graphical information, which was not given in Paper I. For a better identification of predicted and found showers, we compared not only the corresponding geocentric, but also heliocentric radiants, which were both plotted in various coordinate systems. Several of these plots are shown here. With all this information, we intend to give a more complete description of our study of the C/1964 N1's stream.

Let us briefly recapitulate the main results. It was predicted that the C/1964 N1's stream crosses the orbit of our planet ordinarily in four distinct filaments. If some particles were released from the comet's nucleus in the far past, then they can cross the Earth's orbit also in the fifth filament at present. In Paper I, as well as hereinafter, we refer to these filaments as F1 to F4, and F5. Two of the filaments can be identified with the real showers in the meteor databases and the identification of another two is uncertain.

Following the discovery of Šegon et al. (2017), filament F3 was confirmed to be related with the July ξ-Arietids, #533 in the IAU MDC list of all showers[1] (Jopek & Kaňuchová, 2014). Filament F2 was identified with the ϵ-Geminids, #23, and F1 with a poorly defined, yet unknown shower, separated from the IAU MDC CAMS (Gural, 2011; Jenniskens et al., 2011, 2016a,b,c; Jenniskens & Nénon, 2016), and SonotaCo video (SonotaCo, 2009, 2016) databases. And, we suspected a relationship between filament F5 and the shower ξ-Geminids, #718, though this relationship was rather uncertain. The predicted numerousity of the last filament, F4, was low and this was likely the reason why no real counterpart of this filament was found.

Our paper is organized as follows. In Sect. 2, the nominal comet orbit is revisited together with the tool used for the numerical integration of this orbit as well as the orbits of perturbing planets and modeled theoretical particles. In Sect. 3, we give another details about the predicted showers resulting from our simulations. In the fourth section, we give such details about the identification of the predicted showers with their real counterparts and discuss some problems that occurred during the identification. A brief summary of our study is given in Sect. 5.

2. Remarks on the orbit of the parent comet and numerical integration

In our study, we considered the orbit of comet C/1964 N1 with the orbital elements published in the JPL small-body browser (Giorgini et al., 1996)[2]. This orbit, referred to epoch 1964 July 24.0 (JDT = 2438600.5), has the following elements: $q = 0.821752\,\mathrm{au}$, $e = 0.984643$, $a = 53.5099303\,\mathrm{au}$, $\omega = 290.7618^o$, $\Omega = 269.9493^o$, $i = 171.9200^o$, and $T = 2438608.7111$ (1964 August 1.2111).

The positions of the nodes of the nominal orbit during the last 100 millennia can be seen in Fig. 1. We can see the excursions of both post-perihelion (red dots) and pre-perihelion (blue dots) nodes through a large interval of heliocentric distances, from an interior of the Earth's orbit beyond the orbit of Saturn. Both nodes have crossed the orbit of the Earth several times. This implies a possibility that some associated meteor showers can exist.

We recall that the orbit of the parent comet as well as the theoretical particles, and perturbing planets, were integrated by using integrator RA15 (Everhart, 1985) within the software package MERCURY (Chambers, 1999). The gravitational perturbations of eight planets, Mercury to Neptune, were taken into account.

We also recall that the acceleration due to the Poynting-Robertson (P-R, hereinafter) effect is considered in our simulations. In particular, we used the improved formulas derived by Klačka (2014). The usage of them in the case

---

[1] https://www.ta3.sk/IAUC22DB/MDC2007/

[2] http://ssd.jpl.nasa.gov/sbdb.cgi

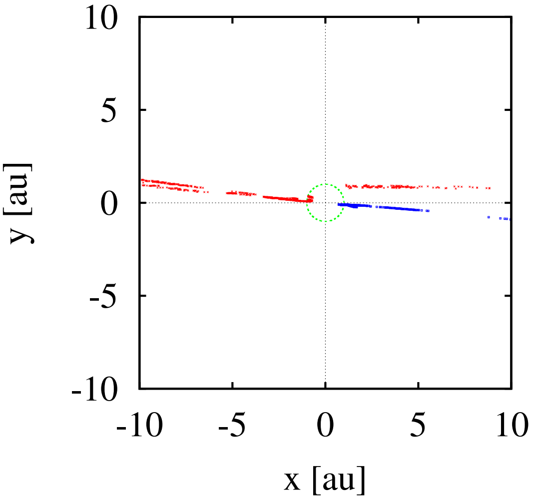

Figure 1. The positions of the orbital nodes of comet C/1964 N1 during the last 100 thousand years. The green circle indicates the orbit of the Earth. The red dots (blue dots) show the positions of ascending (descending) node.
The color version of the figures is provided in the on-line version of the article.

of meteoroid particles was described in, e.g., our previous paper (Hajduková & Neslušan, 2017). The parameter β, being the ratio of the accelerations due to both the P-R effect and gravity of the Sun, is again regarded as a free parameter.

3. The predicted showers

Our way of the modeling of theoretical meteoroid stream associated with the studied comet was described in Paper I. We created several partial models. Each of these was characterized by the evolutionary time t_{ev} and the P-R-effect parameter β. To gain a basic notion about the stream, the basic set of our models consisted of the models with every combination of values $t_{ev} = 5$, 10, 20, 40, and 80 kyr, and $\beta = 0.00001$, 0.0001, 0.001, 0.003, 0.005, 0.007, and 0.009. For some values of evolutionary time, the P-R effect caused a deflection of the stream from the collisional course with the Earth earlier or later than for the initially last considered value of $\beta = 0.009$. During the search of when the effect is strong enough to cause the complete deflection, we also created a few models with other values of β than listed above ($\beta = 0.006$, 0.008, 0.010, and 0.011).

We followed the dynamical evolution of the created stream until present. An overall view of the positions of the geocentric radiants of theoretical particles that approach the Earth's orbit within the distance of 0.05 au at present is shown in Fig. 2a, in an example (model for $(t_{ev},\ \beta) = (20,\ 0.0001)$). When these positions are shown in the ecliptical coordinate system with the origin identical to the apex of the Earth's motion around the Sun (the ecliptic longitude of every radiant, λ, is replaced with the longitude λ_2 calculated according to the relation $\lambda_2 = \lambda - (\lambda_\odot + 270^o)$; $\lambda_\odot$ is the solar longitude of meteor) - see an example in Fig. 2b - we see that the radiant areas of all filaments are in the close vicinity of the apex. This means that all the areas are also close to the ecliptic.

We can observe a rough symmetry of the filaments F1 and F4, as well as F2 and F3, in respect to the Earth's apex (Fig. 2b). The majority of radiants of a given filament are in a single quadrant (four filaments, F1−F4, in four quadrants) of the modified ecliptical coordinate system. However, the distribution to specific quadrants is not exact. There is some "contamination" of radiants of filament F4 in the radiant area of F3.

The detailed distribution of the positions of heliocentric radiants of the particles approaching the Earth's orbit within 0.05 au at present can be seen in Fig. 3 for four models. The radiants are distributed on both sides of the ecliptic (Fig. 3a,b,e,f). Sometimes, the radiant areas touch each other. Because of this circumstance, we also analyzed the distribution of radiants in dependence on the ecliptic longitude (Fig. 3c,d,g,h). A double-peak distribution is seen as for the radiants situated southward as those northward of the ecliptic, in the most models.

Just these double-peaked distributions were the reason why we divided the stream mostly into four filaments, two (F1 and F2) with the radiants northward and two (F3 and F4) southward of the ecliptic. The border between two neighboring filaments is the minimum between the peaks in the ecliptic-longitude distribution and, of course, the filaments are also separated by the ecliptic. In a few models for $t_{ev} = 80$ kyr and high values of β ($\beta = 0.005$, 0.007, 0.009, and 0.010), only a single "southern" filament occurred (Fig. 3f,h). As mentioned in Sect. 1, we refer to this filament as F5 and discuss its occurrence in Sect. 4.3. The mean characteristics of the predicted showers are given in Tables 1 and 2.

In Figs. 4 and 5, the positions of the geocentric and heliocentric radiants of theoretical particles and the corresponding real showers are shown in some models. In particular, the plots of Fig. 4 are related to filament F3 in the models with the P-R-effect parameter $\beta = 0.00001$ and a series of evolutionary times, t_{ev}. In the left-hand plots, there are the geocentric radiants. We can see a shift of some of these radiants to positions with a larger right ascension and declination and, at the same time, larger dispersion of the radiants. As it could be expected, the radiant area is more dispersed in the models where the meteoroid orbits evolve a longer time. The larger dispersion also occurs at the heliocentric radiants which are shown in the right-hand plots. The heliocentric radiants are more compact than their geocentric counterparts. With the increasing t_{ev}, the radiant area of the heliocentric radiants becomes larger, but its center, i.e. the mean radiant, remains the same.

The radiants in Fig. 5 are related to filament F2 in the models for $t_{ev} =$ 40 kyr and a series of the values of β-parameter. We can see influence of the P-R effect on the dynamics of particles in this filament. The effect tends to move the particles away from the vicinity of the Earth's orbit, therefore there is a smaller number of radiants in the radiant area with the increasing value of β. Again, the positions of the geocentric radiants are shown in the left-hand plots. We can see there a gradual shift of the radiant area to smaller values of right ascension. A highly concentrated area of numerous heliocentric radiants, in the right-hand plots, occur up to $\beta = 0.005$. For larger β-values the concentration sharply decreases.

In Paper I we showed the positions of the geocentric radiants in some of the models with the radiants shown in Figs. 4 and 5 in the sun-centered ecliptic coordinates (Figs. 3 and 4 in Paper I). The increasing of dispersion and decreasing of the concentration can also be seen in these plots.

We recall that we constructed the plots like those in Figs. 4 and 5 for every filament in each model, where the identification of a predicted shower with a real shower separated at least from a single database considered was successful. Except for tabular data, these figures also served to remove some identifications, which seemed to be successful on the basis of the D-criterion, but the predicted and observed radiant areas occurred unacceptably different (a more detailed description about the identification is given in Sect. 4).

The radiants of some theoretical particles situated clearly outside the heliocentric radiant area, that were removed from a given filament in this step, occurred to be merged and, thus, indistinguishable from the filament, when the geocentric radiant area was constructed. Hence, the comparison between the heliocentric, instead of geocentric, predicted and real radiants may sometimes result in some improvement (not, however, exceeding the statistical uncertainity at the determination of mean characteristics).

According to Fig. 5 (and others, not shown), there is, mostly, no perfect match between a given prediction and a real shower. Neither does the P-R effect tend to improve the match significantly. The latter implies that the meteoroid particles in the C/1964 N1 stream are, likely, quite large and the effect on them is not very efficient. In more detail, a good match can be found, typically, for β up to the value of about 0.001.

4. Identification of the predicted and real showers

The mean orbits of predicted meteor showers were used as the initial orbits in the iteration, done within the break-point method, to separate the eventual real counterparts of the showers from the meteor catalogs considered. The mean characteristics of these real showers are listed in Tables 3 and 4. Unfortunately, the dependence $N = N(D_{lim})$ constructed within the method never exhibited a clear break point; therefore, it was hard to decide if the separated set of meteors

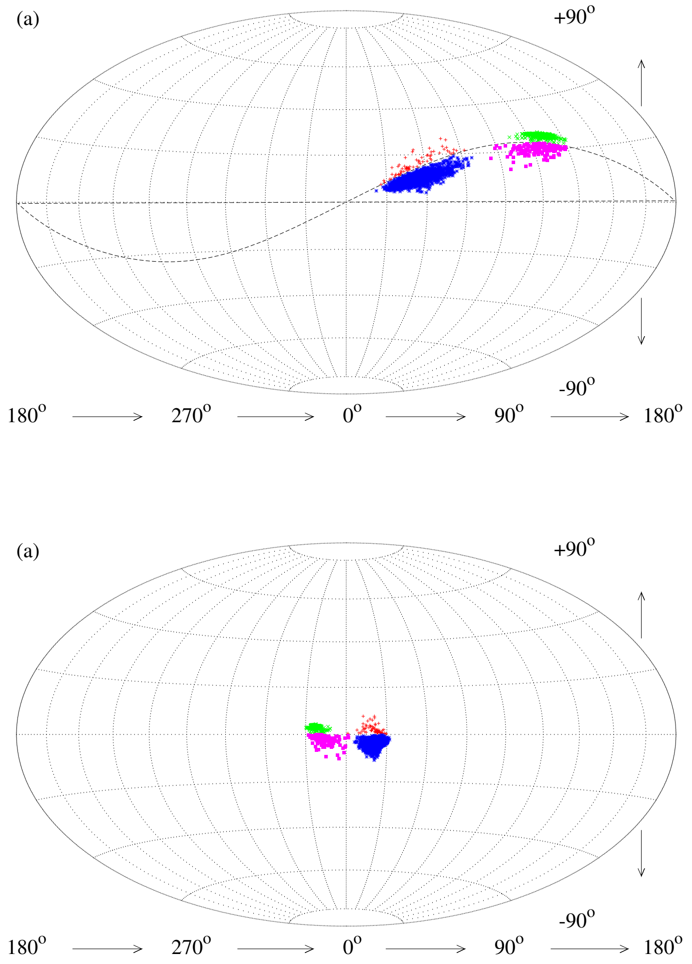

Figure 2. Positions of radiants of theoretical particles grouped in four filaments of the meteoroid stream associated with comet C/1964 N1 in the equatorial coordinate frame (plot a) and the ecliptical coordinate frame with the ecliptic longitude shifted in such a way that the apex of the Earth's motion is in the origin of the coordinate system (plot b). The radiants of particles in the F1 (F2, F3, F4) filament are plotted with red plus-shape points (green crosses, blue asterisks, violet full squares). The radiant positions are shown for the model of the C/1964 N1 stream characterized by $(t_{ev},\ \beta) = (20,\ 0.0001)$. The sinusoid-like curve in plot (a) shows the ecliptic.

is actually a shower or only a random, moderate accumulation of meteors in the given part of the orbital phase space. Hence, one should be careful in regarding the mean orbits of separated showers, listed in Tables 3 and 4, as actually real.

As well, the relationship between the predicted and separated showers is mostly uncertain. We recall (what was already stated in Paper I) that the iteration often resulted in the real mean orbit that was considerably different from the predicted mean orbit. We calculated the Southworth-Hawkins D-discriminant between the predicted and corresponding real mean orbits and we excluded all separated mean orbits with $D_{SH} > 0.2$. We also discarded some separated real showers if their geophysical data were much too different from the predicted counterpart. In particular, we mean that the difference in the mean solar longitude can scarcely exceed $\sim 20^o$, or the position of the predicted mean radiant should be away from its real counterpart more than a dozen of degrees.

We also calculated the D-discriminant between every predicted and known orbit in the IAU MDC list of all showers and we regarded as, possibly, related only the orbits with $D_{SH} \leq 0.20$. These identifications are given in Table 5. (When we used $D_{SH} < 0.25$, there occurred only a singe orbit, in addition, and this is also listed in the parentheses in Table 5.)

Criterion $D_{SH} \leq 0.20$ is not very strict, therefore it is not surprising that a single real shower, regardless it was separated from a considered database or found in the IAU MDC list of showers, is identified with more than a single predicted filament. Fortunately, the search for the minimum value of D_{SH} between the given real shower and a predicted filament leads to a unique association of the shower and filament.

4.1. Filaments F3 and F1, July ξ-Arietids

Seeing the values of the Southworth-Hawkins D-discriminant in the last but one column of the first part of Table 5, we can well identify the theoretical filament F3 to the shower July ξ-Arietids, #533 in the IAU MDC list of showers. This identification is consistent with the result obtained by Šegon et al. (2017). As seen in Table 5, the similarity between the mean orbit of the July ξ-Arietids and the predicted mean orbit of F3 can be characterized with a very small value of the D-discriminant. Specifically, $D_{SH} = 0.053$ when we consider the mean orbit determined by Šegon et al. (2014) and $D_{SH} = 0.070$ when the mean orbit determined by Jenniskens et al. (2016c) is considered. A little larger value, $D_{SH} = 0.078$, characterizes the similarity when we compare our filament F3 and the mean orbit found by Kornoš et al. (2014b).

A real shower corresponding to filament F3, its models especially for $t_{ev} =$ 20 kyr, was also found in the SonotaCo video data, whereby three modifications, denoted by 3S, 30S, and 32S in Table 3, most probably of the same shower, were separated by the break-point method in relation with F3. In addition, the shower 25C separated from the IAU MDC CAMS data is in agreement with F3 for $t_{ev} \geq 40$ kyr. No shower corresponding to F3 was found in the IAU MDC photographic (Porubčan et al., 2011; Neslušan et al., 2014) and EDMOND video (Kornoš et al., 2014a,b) data sets.

Comparing the predicted filament F3 to the real showers, it seems that the real meteoroids were not much influenced by the P-R effect. Their size corresponds to $\beta \lessapprox 0.001$. From Fig. 4 we can conclude that the evolutionary period of the particles in this filament was likely longer than 5 kyr, but shorter than ∼80 kyr, since the predicted radiant area is much more dispersed than its observed counterpart for $t_{ev} = 80$ kyr.

The radiant area of filament F3 is situated below the projection of the ecliptic on the celestial sphere. Filament F1 has a very similar mean orbit, but its radiant area is situated northward of the ecliptic. Hence, F1 can be regarded as a northern branch of the southern F3. Some showers with the mean characteristics resembling those of F1 were found in the IAU MDC CAMS video (showers 13C, 15C, and 17C), as well as in the SonotaCo video databases (10S; see Tables 1 and 2). However, these real showers were predicted only with the help of models with $t_{ev} = 80$ and are very dispersed. They are also uncertain due to a high threshold D_{lim}, from 0.32 to 0.40, used for their separation. Shower 13C was predicted for $\beta \leq 0.001$, 15C only for $\beta = 0.003$, 17C only for $\beta = 0.007$, and 10S for $\beta = 0.007$ and 0.009. No shower in the IAU MDC list was identified with F1.

4.2. Filaments F2 and F4, ϵ-Geminids

Filament F2 has probably its counterpart in the IAU MDC CAMS data - modifications 14C, 18C, 24C, and 26C. The match is quite good for all of them. Furthermore, we found a certain similarity of the mean orbit of F2 with three modifications, 20S, 22S, and 24S, in the SonotaCo data. We must be, however, careful with this identification, since the predicted solar longitude is up to 20^o larger than observed one in the case of 20S, and the observed one is about 20^o larger than predicted one in the case of 22S. The level of match of the predicted and real heliocentric radiant positions in F2 can be seen in Fig. 5, where these positions are shown in the models for $t_{ev} = 40$ kyr and a series of the values of the P-R-effect parameter β.

Filament F4 is the southern branch of the northern F2. Any real counterpart of F4 was found neither in the considered databases, nor in the IAU MDC list of all showers.

4.3. Filament F5

As seen in Fig. 3f,h, filaments F3 and F4, with the radiant areas below the ecliptic, disappeared and, instead of these filaments, there occurred a single filament, F5, with the radiant area in the region near the border of F3 and F4. This behavior can be observed in the theoretical models for $t_{ev} = 80$ kyr and $\beta \geq 0.005$ ($\beta = 0.007$ in Fig. 3f,h).

In Paper I we stated that the occurrence of the “irregular” filament F5 is, most likely, the consequence of a considerable change of the inclination of the parent-comet orbit. (This can be observed in Fig. 1f in Paper I.) In the period from about −92 to −80 kyr, the inclination was decreased, from ∼170^o to ∼158^o (i.e. the absolute value of inclination was increased from ∼10^o to ∼22^o; the orbit was at a larger distance from the ecliptic).

Because of this circumstance, we created additional stream models for the sequence of values t_{ev} equal to 50, 60, 70, 75, 78, 82, 85, and 90 kyr and $\beta = 0.007$ (since filament F5 in the models for $t_{ev} = 80$ kyr is the most abundant in the model for $\beta = 0.007$). As stated in Paper I, only if we consider particles released from the parent 80, 78, 70, and 60 kyr ago, some of them dynamically evolved to the present-day filament F5 and/or other filaments. Hence, only the corresponding data for these models are given in Tables 1 and 2.

We recall that no real counterpart of F5 was separated in the considered databases. We found only a rough similarity of its mean characteristics with the mean characteristics of ξ-Geminids, #718 in the IAU MDC list, which were found by Jenniskens et al. (2016a).

5. Summary

We gave additional details of our study, with the main results already published in Paper I, in which we modeled a theoretical stream of the comet C/1964 N1 (Ikeya). Our simulations of the comet’s stream imply the existence of, basically, four distinct filaments of the stream, which can be observed in the Earth’s atmosphere as four individual showers. We label the filaments as F1 to F4.

We further found that the orbit of the parent comet and its stream rapidly evolved in a period that ended about 50 kyr ago. During this period, the orbital corridors of individual filaments occupied a different space. One of the filaments, F5, was predicted to cross, temporarily, the Earth’s orbit in a different arc of its orbit than the younger filaments F1 to F4.

In the current paper we gave the further graphical and tabular information, which shows in more detail that the separation of real showers corresponding to the predicted ones was often not unique. Starting the iteration procedure from different initial orbits, we obtained several modifications of, most probably, the same real shower - cf. the first and last columns in Tables 3 and 4. In these tables, one can also see that the separated real showers contain a small number of members, 28 at most, many of them consist of 10 or fewer members.

Filament F3 was well identified with the shower July ξ-Arietids, #533 (Šegon et al., 2014, 2017, this work). In this work, filament F2 was identified to ϵ-Geminids, #23. A real counterpart of F1 was found in the CAMS and also SonotaCo data. And, we suspected that filament F5 could, perhaps, be related to the ξ-Geminids, #718. No real counterpart of filament F4 was found in the databases used, or in the IAU MDC list of showers.

The positive identifications of filament F1 in the data for $t_{ev} = 80\,\mathrm{kyr}$ (Table 1 or 2) imply a relatively large evolutionary age of meteoroids in F1 of $\sim$80 kyr. The age of the particles in F2 should be $\sim$20 and more millennia, the age of the largest part is predicted to be around $\sim$40 kyr. Filament F3 can contain some older as well as very young meteoroids, which were only recently released from the surface of the parent. The age of meteoroids in this filament does not likely much exceeds $\sim$40 kyr. Later, the stream seems to be more and more deflected from the collisional course with the Earth.

Filaments F1 to F4 should mostly contain the relatively large particles corresponding to the P-R parameter $\beta \lessapprox 0.001$; more detailed information can be discerned from Table 1, giving the predicted numbers for the specific values of β. Only filament F5, if its real counterpart exists, contains the Earth-hitting particles that are small, corresponding to $0.005 \lessapprox \beta \lessapprox 0.010$.

Our study provides an evidence that the comet C/1964 N1 is an active parent body of at least one, possibly more real showers. At the moment, there are not enough sufficient bulk of the precise data. We believe that the stream of the comet will be studied again in the future, when more extensive meteor data will be collected.

Acknowledgements. The work was supported, in part, by the VEGA - the Slovak Grant Agency for Science, grant No. 2/0037/18, and by the Slovak Research and Development Agency under the contract No. APVV-16-0148.

References

Chambers, J. E., A hybrid symplectic integrator that permits close encounters between massive bodies. 1999, *Mon. Not. R. Astron. Soc.*, **304**, 793, DOI: 10.1046/j.1365-8711.1999.02379.x

Cook, A. F., A Working List of Meteor Streams. 1973, *NASA Special Publication*, **319**, 183

Everhart, E., An efficient integrator that uses Gauss-Radau spacings. 1985, in *Dynamics of Comets: Their Origin and Evolution, Proceedings of IAU Colloq. 83, held in Rome, Italy, June 11-15, 1984. Edited by Andrea Carusi and Giovanni B. Valsecchi. Dordrecht: Reidel, Astrophysics and Space Science Library. Volume 115, 1985, p.185*, ed. A. Carusi & G. B. Valsecchi, 185

Giorgini, J. D., Yeomans, D. K., Chamberlin, A. B., et al., JPL's On-Line Solar System Data Service. 1996, in Bulletin of the American Astronomical Society, Vol. **28**, *AAS/Division for Planetary Sciences Meeting Abstracts #28*, 1158

Gural, P. S., The California All-sky Meteor Surveillance (CAMS) System. 2011, in *Proceedings of the International Meteor Conference, 29th IMC, Armagh, Northern Ireland, 2010*, 28–31

Hajduková, M. & Neslušan, L., Regular and transitory showers of comet C/1979 Y1 (Bradfield). 2017, *Astron. Astrophys.*, **605**, A36, DOI: 10.1051/0004-6361/201730646

Jenniskens, P., Meteor Showers Validated by Cameras for Allsky Meteor Surveillance (CAMS). 2012, in LPI Contributions, Vol. **1667**, *Asteroids, Comets, Meteors 2012*, 6339

Jenniskens, P., Gural, P. S., Dynneson, L., et al., CAMS: Cameras for Allsky Meteor Surveillance to establish minor meteor showers. 2011, *Icarus*, **216**, 40, DOI: 10.1016/j.icarus.2011.08.012

Jenniskens, P. & Nénon, Q., CAMS verification of single-linked high-threshold D-criterion detected meteor showers. 2016, *Icarus*, **266**, 371, DOI: 10.1016/j.icarus.2015.10.004

Jenniskens, P., Nénon, Q., Albers, J., et al., The established meteor showers as observed by CAMS. 2016a, *Icarus*, **266**, 331, DOI: 10.1016/j.icarus.2015.09.013

Jenniskens, P., Nénon, Q., Gural, P. S., et al., CAMS confirmation of previously reported meteor showers. 2016b, *Icarus*, **266**, 355, DOI: 10.1016/j.icarus.2015.08.014

Jenniskens, P., Nénon, Q., Gural, P. S., et al., CAMS newly detected meteor showers and the sporadic background. 2016c, *Icarus*, **266**, 384, DOI: 10.1016/j.icarus.2015.11.009

Jopek, T. J. & Kaňuchová, Z., Current status of the˜IAU MDC Meteor Showers Database. 2014, *Meteoroids 2013*, 353

Klačka, J., Solar wind dominance over the Poynting-Robertson effect in secular orbital evolution of dust particles. 2014, *Mon. Not. R. Astron. Soc.*, **443**, 213, DOI: 10.1093/mnras/stu1133

Kornoš, L., Koukal, J., Piffl, R., & Tóth, J., EDMOND Meteor Database. 2014a, in *Proceedings of the International Meteor Conference, Poznan, Poland, 22-25 August 2013*, ed. M. Gyssens, P. Roggemans, & P. Zoladek, 23–25

Kornoš, L., Matlovič, P., Rudawska, R., et al., Confirmation and characterization of IAU temporary meteor showers in EDMOND database. 2014b, *Meteoroids 2013*, 225

Neslušan, L. & Hajduková, Jr., M., Meteor showers of comet C/1964 N1 (Ikeya). 2018, *Astron. Astrophys.*, **616**, A162, DOI: 10.1051/0004-6361/201832829

Neslušan, L., Porubčan, V., & Svoreň, J., IAU MDC Photographic Meteor Orbits Database: Version 2013. 2014, *Earth Moon and Planets*, **111**, 105, DOI: 10.1007/s11038-013-9427-1

Porubčan, V., Svoreň, J., Neslušan, L., & Schunová, E., The Updated IAU MDC Catalogue of Photographic Meteor Orbits. 2011, in *Meteoroids: The Smallest Solar System Bodies*, ed. W. J. Cooke, D. E. Moser, B. F. Hardin, & D. Janches, 338

SonotaCo, A meteor shower catalog based on video observations in 2007-2008. 2009, *WGN, Journal of the International Meteor Organization*, **37**, 55

SonotaCo, Observation error propagation on video meteor orbit determination. 2016, *WGN, Journal of the International Meteor Organization*, **44**, 42

Šegon, D., Gural, P., Andreić, Ž., et al., New showers from parent body search across several video meteor databases. 2014, *WGN, Journal of the International Meteor Organization*, **42**, 57

Šegon, D., Vaubaillon, J., Gural, P. S., et al., Dynamical modeling validation of parent bodies associated with newly discovered CMN meteor showers. 2017, *Astron. Astrophys.*, **598**, A15, DOI: 10.1051/0004-6361/201629100

A. Appendix: Further graphical and tabular results

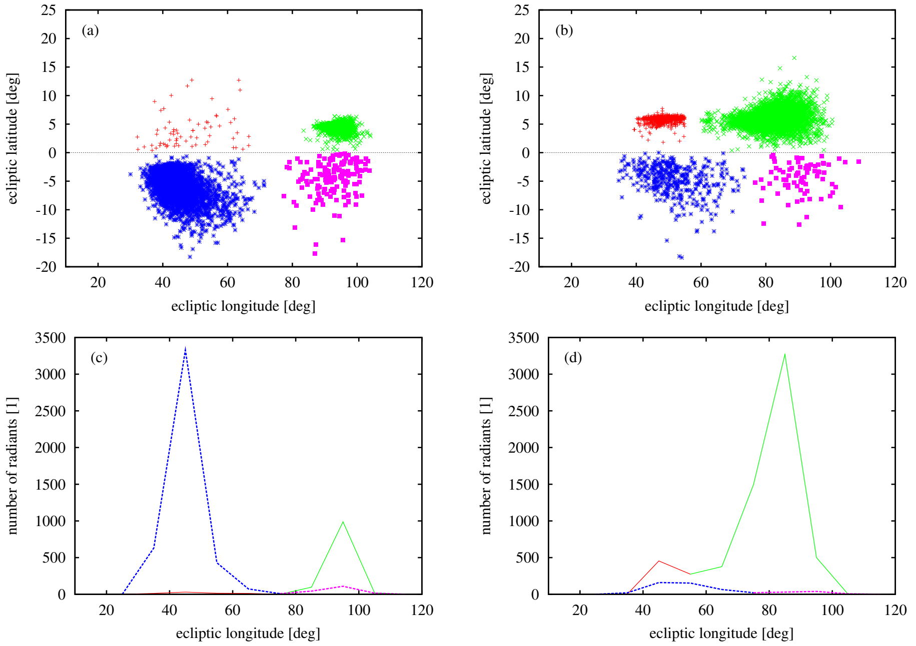

Figure 3. Positions of heliocentric radiants of theoretical particles grouped into five filaments of the meteoroid stream associated with comet C/1964 N1 (plots a, b, e, and f) and distribution of these radiants in the ecliptic longitude (plots c, d, g, and h). The radiants of particles in the F1 (F2, F3, F4, F5) filament are plotted with red plus-shape points (green crosses, blue asterisks, violet full squares, cyan full circles). The distribution of radiants situated northward (southward) from the ecliptic is shown with a red and green solid (blue and violet dashed; in plot (h) cyan dashed) curve. (The color of the part of the curve is the same as the radiant positions in the corresponding plot showing the positions of the radiants.) Both positions and distributions are shown for four models of the C/1964 N1 stream characterized by (t_{ev}, β) equal to (20, 0.0001) (plots a and c), (40, 0.003) (b, d), (80, 0.00001) (e, g), and (80, 0.007) (f, h). To show the positions of radiants, the ecliptical coordinate frame is used. Plots e−h are shown on the next page.

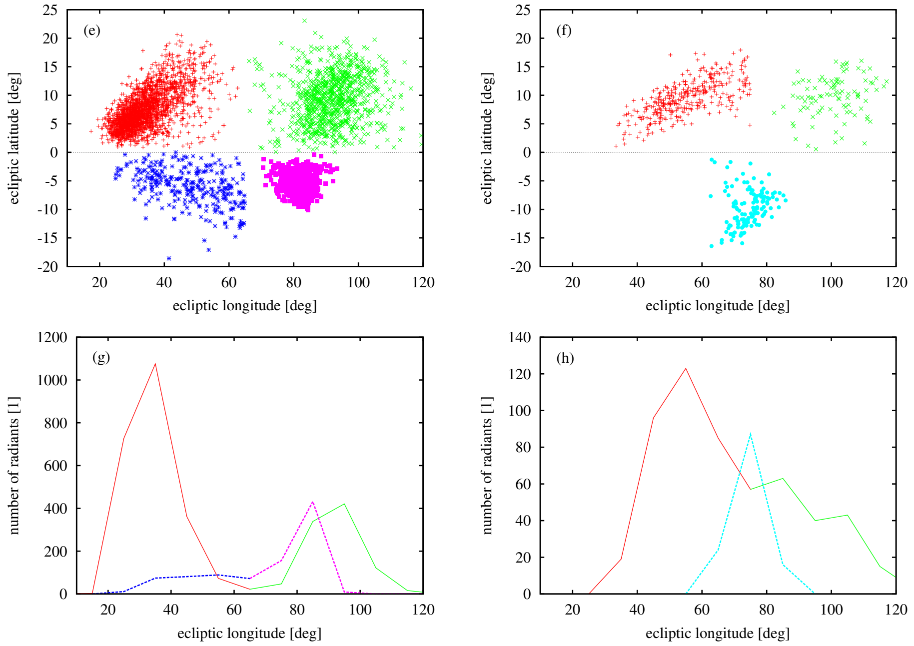

Figure 3. − continued.

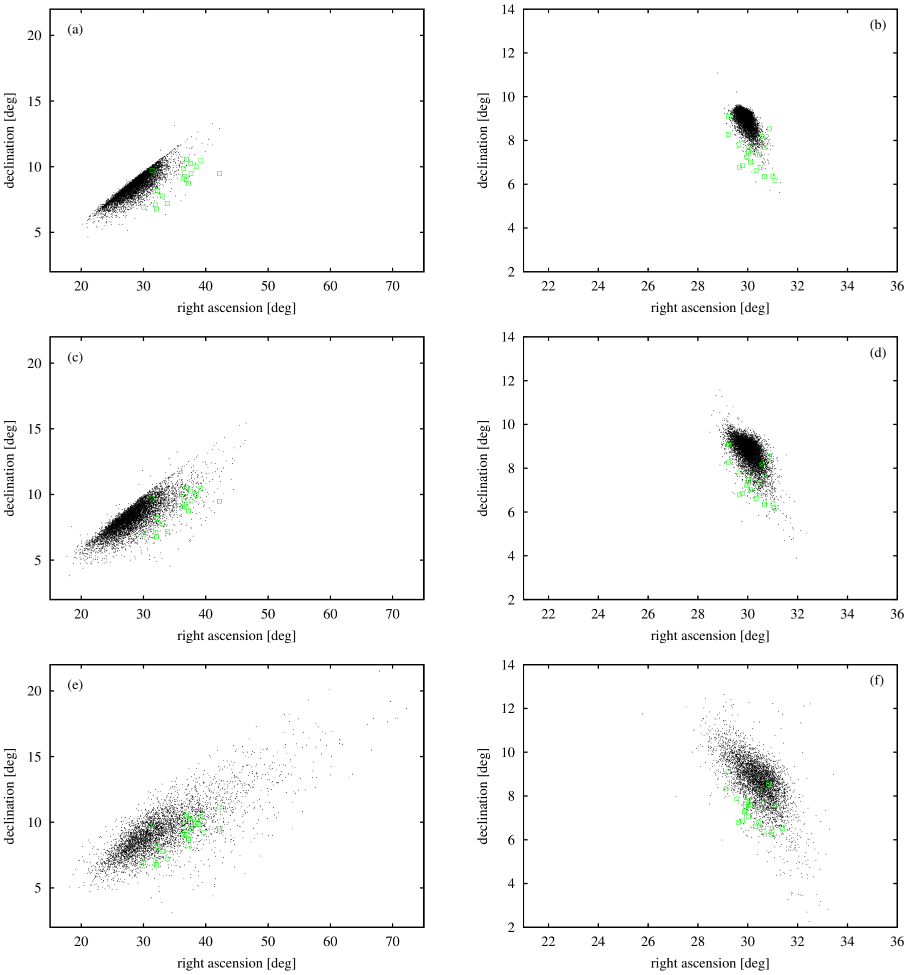

Figure 4. Positions of geocentric (left-hand plots, a, c, e, g, and i) and heliocentric (right-hand plots, b, d, f, h, and j) radiants of theoretical particles (black dots) in the predicted filament F3 and corresponding real-shower meteors separated from the CAMS-video (blue asterisks) and SonotaCo-video (green empty squares) databases. The positions are shown in the models for the P-R-effect parameter $\beta = 0.00001$ and a series of evolutionary times $t_{ev} = 5$ (plots a and b), 10 (c, d), 20 (e, f), 40 (g, h), and 80 kyr (i, j). Plots g−j are shown on the next page.

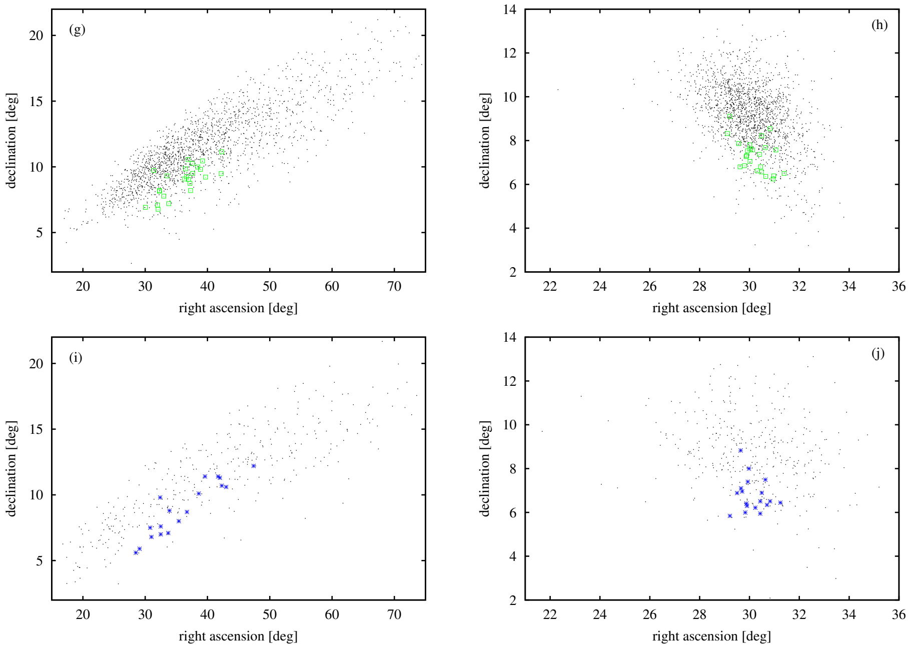

Figure 4. − continued.

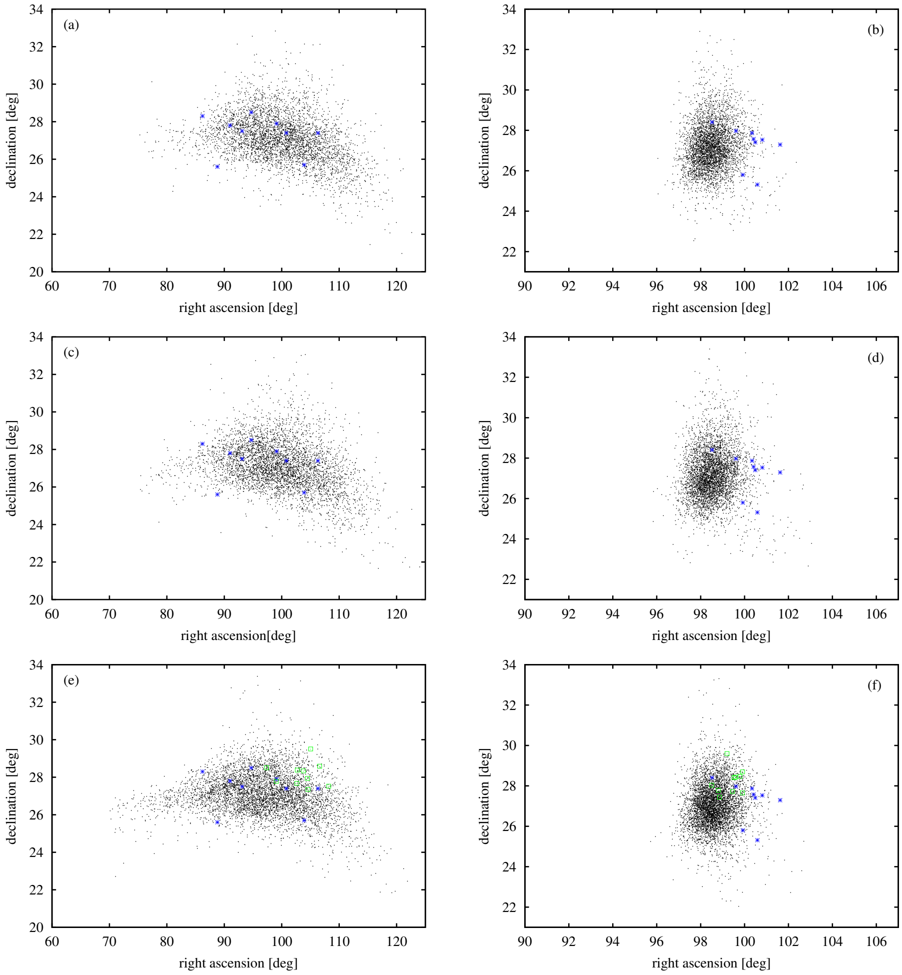

Figure 5. Positions of geocentric (right-hand plots, a, c, e, g, i, k, and m) and heliocentric (right-hand plots, b, d, f, h, j, l, and n) radiants of theoretical particles (black dots) in the predicted filament F2 and corresponding real-shower meteors separated from the CAMS-video (blue asterisks) and SonotaCo-video (green empty squares) databases. The positions are shown in the models for the evolutionary time $t_{ev} = 40\,\mathrm{kyr}$ and a series of the values of P-R-effect parameter $\beta = 0.00001$ (plots a and b), 0.0001 (c, d), 0.001 (e, f), 0.003 (g, h), 0.005 (i, j), 0.007 (k, l), and 0.008 (m, n). Plots g−n are shown on the next page.

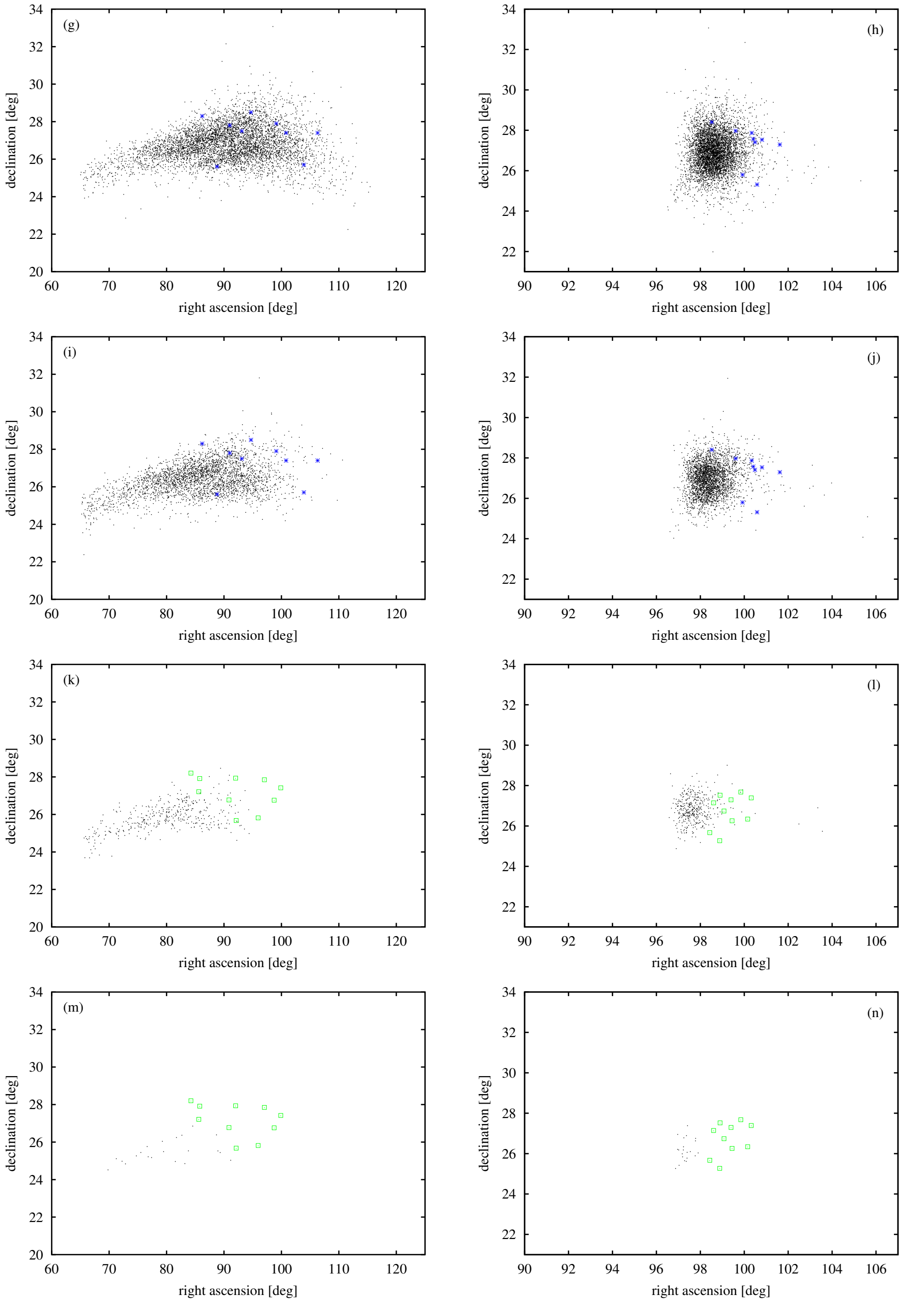

Figure 5. − continued.

Table 1. The mean geophysical characteristics of the predicted meteor showers. Notes: t_{ev} - the period following the orbital evolution (the theoretical stream was modeled before this time); β - the parameter characterizing the strength of the P-R effect; $\lambda_{\odot}$ - the mean solar longitude corresponding to the expected maximum of a shower; α and δ - equatorial coordinates of the mean geocentric radiant; V_g and V_h - the mean geocentric and heliocentric velocity; γ - the angular distance of the mean radiant from the Sun at the time corresponding to the $\lambda_{\odot}$ of the maximum; N_s - the number of particles in the orbits approaching the Earth's orbit within 0.05 au; D_{lim} - the threshold value of the Southworth-Hawkins D-discriminant used to separate the meteors of the filament; i.r.s. - the real shower identified with a given filament in a given model (according to this identification number, the real shower can be found in Tables 3 and 4). Time t_{ev} is given in kilo-years, the angular quantities are given in degrees, and velocities in km s^{-1}.

t_{ev}	β	$\lambda_{\odot}$	α	δ	V_g	V_h	γ	N_s	D_{lim}	i.r.s.
				filament F1						
10	0.0001	104.2± 7.5	27.9± 5.8	12.7± 2.0	68.9± 0.3	41.6± 0.1	74.	6	0.14	–
20	0.00001	117.3± 11.9	37.7±C 9.1	16.3± 3.4	69.5± 0.5	41.5± 0.1	77.	59	0.24	–
20	0.0001	115.9± 14.8	36.2± 11.1	16.4± 4.4	69.4± 0.7	41.6± 0.1	77.	67	0.27	–
20	0.001	115.3± 11.9	35.8± 9.0	16.2± 3.5	69.5± 0.5	41.6± 0.1	77	31	0.18	–
20	0.003	126.9± 18.2	44.6± 14.2	18.0± 3.7	69.9± 0.6	41.5± 0.1	80.	18	0.23 –	
40	0.00001	137.0± 19.5	52.1± 14.1	21.1± 4.1	70.2± 0.8	41.6± 0.2	82.	166	0.32	–
40	0.0001	127.1± 15.2	45.6± 11.9	18.9± 3.7	69.8± 0.6	41.6± 0.1	79.	108	0.23	–
40	0.001	138.5± 16.7	51.8± 11.7	21.5± 3.3	70.5± 0.7	41.7± 0.2	84.	134	0.28	–
40	0.003	135.3± 12.0	47.1± 8.7	20.9± 2.4	70.8± 0.4	41.8± 0.1	85.	917	0.13	–
40	0.005	133.8± 11.5	45.7± 8.2	20.5± 2.3	70.8± 0.4	41.8± 0.1	85	2059	0.12	–
40	0.007	133.0± 11.1	45.0± 7.7	20.2± 2.3	70.8± 0.4	41.8± 0.1	85.	1286	0.14	–
40	0.008	132.0± 11.4	44.0± 7.8	19.9± 2.3	70.8± 0.4	41.8± 0.1	85.	346	0.13	–
50	0.007	125.2± 10.0	39.5± 7.1	18.4± 2.2	70.5± 0.3	41.7± 0.1	82.	2356	0.19	20S
60	0.007	103.1± 7.9	23.3± 5.4	11.8± 1.9	69.8± 0.4	41.8± 0.0	77.	27	0.11	–
70	0.007	110.4± 8.9	28.7± 6.6	14.9± 2.9	69.9± 0.4	41.7± 0.1	78.	1514	0.23	–
80	0.00001	98.9± 12.1	20.6± 8.6	13.4± 4.7	69.0± 0.6	41.7± 0.1	75.	2248	0.32	13C
80	0.0001	99.7± 12.6	21.2± 9.2	13.7± 4.8	69.0± 0.6	41.7± 0.1	75.	2306	0.38	13C
80	0.001	105.6± 15.6	25.7± 11.8	15.7± 5.8	69.3± 0.6	41.7± 0.1	76.	2103	0.40	13C
80	0.003	120.0± 17.1	37.4± 14.1	20.9± 5.8	69.6± 0.5	41.7± 0.1	78.	1903	0.40	15C

Table 1. − continued.

t_{ev}	β	$\lambda_\odot$	α	δ	V_g	V_h	γ	N_s	D_{lim}	i.r.s.
filament F1 − continuation										
80	0.005	127.5± 17.6	44.2± 15.2	22.9± 5.2	69.8± 0.5	41.7± 0.1	79	1362	0.37	16C
80	0.007	133.1± 19.7	49.5± 17.1	23.7± 5.1	70.0± 0.5	41.7± 0.1	80.	442	0.38	17C, 10S
80	0.009	130.8± 13.7	47.1± 12.1	22.5± 4.7	70.1± 0.4	41.7± 0.0	80	67	0.32	10S
80	0.010	135.9± 27.8	49.1± 22.5	20.1± 5.9	70.4± 0.6	41.7± 0.2	84	10	0.28	−
filament F2										
10	0.00001	217.0± 2.6	112.1± 2.1	24.6± 0.4	69.7± 0.2	42.2± 0.0	107	79	0.06	−
10	0.0001	216.4± 2.4	111.7± 1.9	24.7± 0.3	69.7± 0.1	42.2± 0.0	107.	77	0.17	−
10	0.001	215.5± 2.3	110.9± 1.9	24.8± 0.3	69.8± 0.1	42.2± 0.0	107	134	0.06	−
10	0.003	214.4± 1.6	109.9± 1.4	25.0± 0.2	69.8± 0.1	42.2± 0.0	106	170	0.06	−
10	0.005	214.1± 1.4	109.5± 1.1	25.1± 0.1	69.8± 0.1	42.2± 0.0	106	64	0.03	−
20	0.00001	211.6± 5.2	108.1± 4.2	25.5± 0.7	70.0± 0.2	42.2± 0.1	105.	1067	0.23	18C
20	0.0001	211.2± 5.1	107.8± 4.1	25.5± 0.7	70.0± 0.3	42.1± 0.1	105.	1103	0.18	18C
20	0.001	209.7± 5.1	106.5± 4.2	25.8± 0.6	70.1± 0.2	42.2± 0.0	105.	1441	0.18	18C
20	0.003	206.5± 5.0	103.7± 4.1	26.1± 0.5	70.2± 0.2	42.1± 0.0	104	1689	0.15	14C
20	0.005	204.4± 4.1	101.8± 3.3	26.4± 0.3	70.3± 0.2	42.1± 0.0	104.	721	0.13	14C
20	0.006	202.7± 4.2	100.3± 3.5	26.6± 0.2	70.3± 0.2	42.2± 0.0	103.	239	0.10	14C
40	0.00001	201.7± 8.1	100.0± 6.9	27.1± 1.3	70.3± 0.3	42.1± 0.1	103.	4059	0.21	14C
40	0.0001	201.3± 8.1	99.7± 6.9	27.1± 1.3	70.3± 0.3	42.1± 0.1	103.	4361	0.24	14C
40	0.001	197.5± 9.3	96.8± 7.6	28.1± 8.3	69.8± 5.2	42.5± 3.4	101.	5074	0.22	14C, 24S
40	0.003	190.7± 9.7	90.8± 8.2	26.8± 1.0	70.7± 0.3	42.0± 0.1	100.	5379	0.21	14C
40	0.005	185.2± 9.2	86.3± 7.7	26.4± 0.9	70.9± 0.2	42.0± 0.1	99.	2894	0.20	14C
40	0.007	178.1± 8.6	80.3± 6.9	25.9± 0.7	71.0± 0.2	42.0± 0.1	97.	347	0.14	20S
40	0.008	178.4± 7.9	80.1± 6.3	25.5± 0.6	71.0± 0.2	42.0± 0.1	97.	21	0.08	20S
50	0.007	181.4± 9.5	83.7± 7.8	25.7± 1.1	71.0± 0.2	41.9± 0.1	97.	544	0.20	14C, 20S
70	0.007	188.8± 9.8	89.6± 8.3	25.8± 1.2	70.8± 0.2	42.0± 0.1	99.	110	0.19	14C, 20S
80	0.00001	202.2± 12.8	102.4± 10.9	28.2± 2.6	70.3± 0.4	42.0± 0.1	101.	953	0.39	18C, 22S
80	0.0001	203.5± 11.0	103.3± 9.6	28.1± 2.6	70.3± 0.4	42.0± 0.1	102.	999	0.38	22S, 18C
80	0.001	203.1± 12.4	103.7± 10.7	28.1± 2.7	70.4± 0.4	42.0± 0.1	101.	1137	0.39	22S, 18C
80	0.003	200.6± 16.3	104.6± 13.2	28.8± 2.8	70.6± 0.4	42.0± 0.1	98.	1074	0.40	23C

Table 1. - continued.

t_{ev}	β	$\lambda_{\odot}$	α	δ	V_g	V_h	γ	N_s	D_{lim}	i.r.s.
filament F2 − continuation										
80	0.005	200.3± 14.8	107.1± 12.4	29.0± 2.6	70.9± 0.3	41.9± 0.1	95	462	0.40	24C
80	0.007	202.7± 11.2	108.8± 9.1	27.9± 2.4	71.0± 0.3	41.9± 0.1	96.	98	0.38	24C
80	0.009	200.5± 16.2	108.2± 11.7	28.1± 2.5	71.0± 0.4	42.0± 0.1	94.	13	0.32	26C
filament F3										
5	0.00001	103.1± 3.6	28.6± 2.5	8.5± 0.9	68.8± 0.2	41.6± 0.0	74.	7072	0.14	3S
5	0.0001	103.1± 3.6	28.6± 2.5	8.5± 0.9	68.8± 0.2	41.6± 0.0	74.	6847	0.16	3S
5	0.001	103.6± 3.6	28.9± 2.5	8.7± 0.9	68.9± 0.3	41.7± 0.0	74.	5055	0.13	3S
5	0.003	105.1± 4.6	29.8± 3.2	9.1± 1.2	69.0± 0.3	41.7± 0.0	74.	1320	0.14	3S
5	0.005	110.1± 7.2	33.1± 4.9	10.5± 1.8	69.4± 0.5	41.7± 0.0	76	42	0.10	32S
10	0.00001	102.8± 4.9	28.4± 3.5	8.2± 1.2	68.8± 0.3	41.6± 0.1	73.	7158	0.18	3S
10	0.0001	102.8± 5.0	28.5± 3.6	8.3± 1.2	68.8± 0.3	41.6± 0.1	73.	7074	0.21	3C
10	0.001	103.2± 4.5	28.6± 3.2	8.4± 1.2	68.8± 0.3	41.6± 0.0	74.	5149	0.19	3S
10	0.003	104.7± 4.8	29.4± 3.3	9.0± 1.3	69.0± 0.3	41.7± 0.0	74.	1209	0.20	3S
10	0.005	110.1± 7.0	32.8± 4.8	10.7± 1.9	69.5± 0.4	41.7± 0.0	76	33	0.09	32S
20	0.00001	108.2± 8.6	32.8± 6.4	9.3± 1.9	69.0± 0.4	41.6± 0.1	75.	4484	0.27	30S
20	0.0001	108.1± 8.3	32.7± 6.2	9.2± 1.8	69.0± 0.4	41.6± 0.1	74.	4460	0.24	
20	0.001	108.7± 7.8	33.0± 5.9	9.5± 1.8	69.0± 0.4	41.6± 0.1	75.	3207	0.28	3S
20	0.003	111.3± 8.7	34.3± 6.4	10.5± 2.1	69.3± 0.4	41.6± 0.1	76.	852	0.26	3S
20	0.005	112.8± 7.2	34.4± 5.0	11.6± 1.9	69.6± 0.4	41.7± 0.1	77.	79	0.20	25C, 30S
20	0.006	119.0± 12.2	38.5± 8.7	13.2± 2.6	70.0± 0.6	41.7± 0.1	79	12	0.14	–
40	0.00001	117.0± 13.3	39.2± 10.2	11.4± 2.8	69.4± 0.6	41.6± 0.1	77.	1724	0.26	30S
40	0.0001	116.0± 12.3	38.4± 9.5	11.1± 2.7	69.4± 0.6	41.6± 0.1	76.	1572	0.22	25C, 30S
40	0.001	120.3± 14.7	41.6± 11.3	12.2± 3.0	69.6± 0.6	41.6± 0.1	77.	1217	0.22	25C
40	0.003	121.8± 12.6	42.2± 9.7	12.9± 2.9	69.8± 0.6	41.6± 0.1	78.	407	0.26	25C
40	0.005	120.4± 9.1	40.2± 6.7	13.2± 2.4	69.9± 0.5	41.7± 0.1	78.	56	0.13	25C
50	0.007	155.2± 7.3	71.0± 6.3	18.3± 0.9	70.7± 0.2	41.6± 0.0	83.	6	0.22	–
70	0.007	117.3± 13.2	35.0± 9.0	11.5± 3.0	68.7± 4.9	41.2± 2.1	81.	20	0.20	25C, 32S
80	0.00001	112.7± 13.6	36.4± 11.4	10.3± 3.4	69.1± 0.6	41.6± 0.1	75.	297	0.35	25C
80	0.0001	119.1± 17.6	42.0± 14.9	11.3± 3.7	69.3± 0.7	41.6± 0.1	76.	405	0.40	25C

Table 1. - continued.

t_{ev}	β	$\lambda_\odot$	α	δ	V_g	V_h	γ	N_s	D_{lim}	i.r.s.
filament F3 − continuation										
80	0.001	122.4± 17.7	45.1± 15.0	12.2± 3.5	69.3± 0.7	41.6± 0.1	76.	446	0.38	25C
80	0.003	128.2± 15.7	50.4± 13.7	13.7± 3.3	69.5± 0.6	41.6± 0.1	77	277	0.35	–
80	0.0001	119.1± 17.6	42.0± 14.9	11.3± 3.7	69.3± 0.7	41.6± 0.1	76.	405	0.40	25C
80	0.001	122.4± 17.7	45.1± 15.0	12.2± 3.5	69.3± 0.7	41.6± 0.1	76.	446	0.38	25C
80	0.003	128.2± 15.7	50.4± 13.7	13.7± 3.3	69.5± 0.6	41.6± 0.1	77	277	0.35	–
filament F4										
10	0.00001	213.7± 3.1	109.2± 2.5	21.5± 0.4	69.9± 0.1	42.1± 0.0	106.	5	0.05	–
10	0.0001	197.0± 13.4	97.7± 9.7	20.7± 1.5	70.6± 0.4	41.9± 0.3	100.	6	0.14	–
20	0.00001	202.1± 12.7	101.9± 9.3	20.1± 1.7	70.5± 0.4	41.9± 0.2	101.	152	0.26	–
20	0.0001	202.9± 12.0	102.5± 8.8	20.4± 1.4	70.5± 0.4	41.9± 0.2	101.	165	0.28	–
20	0.001	203.6± 7.5	102.1± 5.9	20.8± 1.1	70.5± 0.3	42.0± 0.1	102.	84	0.13	–
20	0.003	199.2± 11.0	98.8± 8.0	20.6± 1.6	70.6± 0.3	42.0± 0.2	101.	49	0.27	–
40	0.00001	200.8± 14.2	101.9± 10.7	19.7± 1.9	70.7± 0.4	41.9± 0.2	100.	348	0.24	–
40	0.0001	199.6± 14.4	101.2± 10.9	19.6± 1.9	70.7± 0.4	41.9± 0.2	99.	359	0.24	–
40	0.001	201.2± 10.9	102.4± 8.5	19.8± 1.7	70.8± 0.3	41.9± 0.1	100.	195	0.24	–
40	0.003	192.2± 13.9	95.3± 10.1	20.5± 1.5	70.9± 0.3	41.9± 0.2	97.	83	0.33	–
40	0.005	194.5± 7.7	96.9± 6.7	20.7± 0.8	71.0± 0.1	41.9± 0.1	98.	12	0.16	–
50	0.007	194.2± 8.0	96.7± 7.3	20.2± 2.6	71.0± 0.3	42.0± 0.1	98.	20	0.27	–
80	0.00001	200.2± 5.6	94.7± 4.6	19.8± 1.0	69.7± 0.3	42.1± 0.0	106	567	0.20	–
80	0.0001	199.9± 5.4	94.4± 4.5	19.8± 1.0	69.7± 0.3	42.1± 0.0	106.	507	0.18	–
80	0.001	199.2± 6.0	93.9± 4.9	20.1± 0.8	69.8± 0.3	42.1± 0.0	106.	254	0.18	–
80	0.003	193.4± 25.6	104.0± 18.9	16.6± 2.6	70.9± 0.5	41.8± 0.2	90.	179	0.32	–
filament F5										
70	0.007	186.4± 5.3	83.6± 4.3	20.9± 0.5	70.4± 0.2	42.1± 0.0	102.	336	0.10	–
78	0.007	182.8± 4.7	80.3± 3.6	19.1± 0.5	70.3± 0.2	42.0± 0.0	102.	189	0.10	–
80	0.005	190.5± 6.1	87.2± 5.1	17.8± 1.8	70.0± 0.2	42.1± 0.0	103.	114	0.18	–
80	0.007	188.7± 5.7	86.0± 5.0	17.2± 1.8	70.1± 0.2	42.1± 0.0	103.	123	0.20	–
80	0.009	184.2± 4.4	82.1± 3.9	16.3± 2.6	70.1± 0.3	42.0± 0.0	102.	33	0.21	–

Table 2. Mean orbital characteristics with the dispersion (characterized by the standard deviation) of the predicted annual meteor showers associated with the parent body considered. Notes: t_{ev}, β, and i.r.s - as in Table 1; q - the mean perihelion distance; a - the mean semi-major axis; e - the mean eccentricity; ω - the mean argument of perihelion; Ω - the mean longitude of ascending node; and i - the mean inclination to the ecliptic. Quantities q and a are given in astronomical units and angular elements in degrees.

t_{ev}	β	q	a	e	ω	Ω	i	i.r.s.
				filament F1				
10	0.0001	0.794± 0.041	64.2± 28.3	0.985± 0.008	143.8± 24.4	123.7± 23.8	177.4± 2.0	–
20	0.00001	0.862± 0.057	51.9± 44.5	0.978± 0.009	138.4± 21.8	120.9± 22.7	176.9± 1.9	–
20	0.0001	0.857± 0.075		0.982± 0.010	141.4± 19.1	122.6± 19.0	175.8± 3.1	–
20	0.001	0.856± 0.059	49.8± 44.4	0.982± 0.010	143.7± 18.0	124.9± 19.8	176.2± 2.3	–
20	0.003	0.910± 0.071	46.5± 20.9	0.977± 0.009	135.2± 19.1	117.2± 18.8	177.1± 1.7	–
40	0.00001	0.927± 0.070		0.982± 0.013	155.9± 29.7	139.0± 26.5	175.0± 2.5	–
40	0.0001	0.894± 0.065	65.6± 64.7	0.979± 0.010	141.5± 21.7	127.0± 21.3	176.1± 2.0	–
40	0.001	0.953± 0.067	240.1± 199.5	0.988± 0.012	163.2± 26.8	141.5± 22.2	174.8± 2.2	–
40	0.003	0.978± 0.042	330.6± 234.7	0.996± 0.002	173.6± 5.4	145.7± 5.4	174.2± 0.6	–
40	0.005	0.978± 0.043		0.996± 0.002	170.6± 6.1	142.4± 6.3	174.3± 0.6	–
40	0.007	0.980± 0.045	401.4± 367.1	0.997± 0.002	168.7± 5.6	140.2± 5.8	174.4± 0.5	–
40	0.008	0.981± 0.047		0.997± 0.001	166.0± 4.8	137.0± 4.9	174.4± 0.5	–
50	0.007	0.963± 0.042		0.995± 0.003	151.6± 11.8	122.6± 13.0	174.6± 0.9	20S
60	0.007	0.884± 0.045		0.999± 0.001	104.0± 8.6	69.8± 8.6	175.5± 0.3	–
70	0.007	0.907± 0.041	208.7± 180.1	0.994± 0.004	128.1± 17.5	97.1± 19.7	174.2± 2.0	–
80	0.00001	0.821± 0.064		0.994± 0.005	128.9± 17.2	98.8± 19.0	171.6± 3.3	13C
80	0.0001	0.823± 0.062	206.4± 191.3	0.993± 0.005	129.5± 17.0	99.8± 19.1	171.4± 3.4	13C
80	0.001	0.849± 0.067	209.0± 206.5	0.993± 0.005	134.6± 17.6	106.4± 20.7	170.8± 3.9	13C
80	0.003	0.899± 0.056	146.6± 123.2	0.990± 0.006	141.2± 14.6	119.6± 19.9	168.6± 3.8	15C
80	0.005	0.915± 0.049	118.9±111.9	0.989± 0.006	142.0±15.5	125.1± 21.4	168.3± 3.5	16C
80	0.007	0.927± 0.046	96.9± 56.2	0.987± 0.007	142.9± 18.1	128.9± 24.5	169.0± 3.4	17C, 10S
80	0.009	0.935± 0.038	96.9± 61.5	0.987± 0.006	142.3±16.7	126.0± 21.3	170.6± 3.5	10S
80	0.010	0.953± 0.055		0.989± 0.008	162.3±43.2	137.3± 46.1	174.2± 3.8	–

Table 2. − continued.

t_{ev}	β	q	a	e	ω	Ω	i	i.r.s.
filament F2								
10	0.00001	0.762± 0.019	132.9± 57.3	0.994± 0.002	264.9± 2.4	243.3± 2.6	174.3± 0.1	–
10	0.0001	0.766± 0.017	130.6± 31.6	0.994± 0.001	264.6± 2.4	243.0± 2.7	174.2± 0.1	–
10	0.001	0.771± 0.016	167.6± 76.0	0.995± 0.002	263.4± 2.1	241.5± 2.5	174.2± 0.1	–
10	0.003	0.776± 0.011		0.996± 0.002	262.1± 1.7	239.8± 2.0	174.1± 0.1	–
10	0.005	0.776± 0.011	342.7±191.9	0.997± 0.001	261.1± 0.9	238.4± 1.0	174.0± 0.0	–
20	0.00001	0.803± 0.035	154.5± 109.3	0.993± 0.004	250.7± 10.5	229.6± 10.5	173.8± 1.0	18C
20	0.0001	0.806± 0.035	146.4± 78.8	0.993± 0.004	250.8± 10.0	229.6± 9.9	173.8± 0.9	18C
20	0.001	0.814± 0.035	163.9± 98.1	0.994± 0.003	250.1± 7.2	228.5± 7.4	173.6± 0.7	18C
20	0.003	0.832± 0.033		0.995± 0.003	246.9± 5.9	224.5± 6.3	173.5± 0.6	14C
20	0.005	0.842± 0.029	280.6± 238.1	0.996± 0.002	244.4± 3.9	221.4± 4.1	173.4± 0.3	14C
20	0.006	0.850± 0.030	384.2± 375.7	0.997± 0.001	242.8± 2.7	219.3± 2.8	173.3± 0.2	14C
40	0.00001	0.848± 0.044	119.3± 75.4	0.991± 0.004	223.9± 15.0	200.5± 16.5	172.4± 2.0	14C
40	0.0001	0.850± 0.044	122.3± 120.8	0.991± 0.004	223.1± 15.2	199.7± 16.7	172.4± 2.1	14C
40	0.001	0.867± 0.044		0.991± 0.004	218.5± 15.8	194.7± 17.4	172.7± 1.9	14C, 24S
40	0.003	0.900± 0.043	146.1±133.8	0.992± 0.004	209.4± 16.5	184.6± 18.1	173.6± 1.6	14C
40	0.005	0.922± 0.038	157.3± 96.5	0.992± 0.004	202.6± 15.4	177.0± 16.6	174.2± 1.3	14C
40	0.007	0.946± 0.033	174.8± 91.4	0.993± 0.003	193.7± 12.4	166.7± 13.1	174.9± 1.0	20S
40	0.008	0.941± 0.034	167.0± 61.8	0.994± 0.002	191.1± 13.4	162.9± 13.6	175.6± 0.8	20S
50	0.007	0.948± 0.039	117.3± 80.7	0.990± 0.005	204.6± 19.4	180.4± 20.5	175.3± 1.7	14C, 20S
70	0.007	0.912± 0.043	103.3± 100.1	0.987± 0.007	206.3± 20.4	182.2± 21.8	175.3± 1.9	14C, 20S
80	0.00001	0.867± 0.066		0.984± 0.008	217.6± 19.2	200.1± 19.3	170.0± 4.2	22S, 18C
80	0.0001	0.863± 0.064	82.9± 75.8	0.985± 0.008	218.2± 16.7	200.5± 17.3	170.1± 4.2	22S, 18C
80	0.001	0.873± 0.067		0.984± 0.008	216.4± 17.9	200.7± 18.7	170.0± 4.1	22S, 18C
80	0.003	0.915± 0.067	60.7± 46.7	0.981± 0.007	206.4± 21.0	199.4± 19.8	168.5± 4.0	23C
80	0.005	0.948± 0.053	53.2± 27.5	0.979± 0.007	198.5± 19.0	199.7± 18.1	168.0± 3.4	24C
80	0.007	0.945± 0.056	53.2± 26.1	0.979± 0.008	202.5± 18.2	203.1± 14.7	169.8± 3.5	24C
80	0.009	0.945± 0.045	53.7± 17.9	0.981± 0.006	196.3± 25.1	199.7± 20.3	169.3± 3.8	26C

Table 2. - continued.

t_{ev}	β	q	a	e	ω	Ω	i	i.r.s.
				filament F3				
5	0.00001	0.800± 0.027	84.9± 31.5	0.989± 0.003	287.2± 8.8	266.0± 8.8	174.1± 0.8	3S
5	0.0001	0.800± 0.027	85.2± 31.0	0.990± 0.003	287.2± 8.9	266.0± 8.8	174.1± 0.8	3S
5	0.001	0.805± 0.027	99.0± 40.8	0.991± 0.003	285.8± 8.0	264.4± 7.9	174.2± 0.7	3S
5	0.003	0.818± 0.033	144.6± 109.5	0.993± 0.002	284.3± 7.2	262.6± 7.1	174.3± 0.7	3S
5	0.005	0.855± 0.048		0.997± 0.002	286.1± 6.3	263.8± 6.3	174.7± 0.5	32S
10	0.00001	0.794± 0.034	86.8± 43.5	0.989± 0.004	293.8± 12.6	272.8± 12.8	173.8± 1.3	3S
10	0.0001	0.794± 0.035	87.6± 42.6	0.989± 0.004	293.6± 12.6	272.7± 12.9	173.8± 1.3	3S
10	0.001	0.800± 0.033	99.4± 51.0	0.990± 0.004	290.8± 11.5	269.5± 11.7	174.0± 1.2	3S
10	0.003	0.817± 0.034	136.9± 66.9	0.993± 0.003	286.8± 8.8	264.8± 8.8	174.4± 0.9	3S
10	0.005	0.858± 0.046		0.996± 0.001	284.8± 5.3	261.9± 5.3	175.3± 0.5	32S
20	0.00001	0.817± 0.049	79.1± 52.4	0.987± 0.006	302.0± 16.4	282.9± 17.3	173.0± 2.3	30S
20	0.0001	0.816± 0.048	80.6± 58.9	0.987± 0.006	301.7± 16.0	282.5± 16.8	173.1± 2.1	30S
20	0.001	0.824± 0.045	84.3± 82.5	0.988± 0.006	300.5± 15.9	281.0± 16.8	173.4± 2.1	3S
20	0.003	0.849± 0.047		0.989± 0.006	298.4± 22.2	278.6± 18.1	174.3± 2.1	3S
20	0.005	0.872± 0.044		0.991± 0.005	301.5± 21.0	278.7± 20.9	176.1± 1.5	25C, 30S
20	0.006	0.904± 0.069		0.988± 0.012	306.4± 20.4	283.3± 21.0	176.7± 1.7	–
40	0.00001	0.859± 0.063	70.8± 61.5	0.984± 0.008	311.1± 22.9	293.7± 23.5	173.4± 2.9	30S
40	0.0001	0.856± 0.061		0.984± 0.007	310.7± 20.5	293.1± 20.8	173.3± 2.9	25C, 30S
40	0.001	0.875± 0.062	69.2± 51.4	0.984± 0.008	309.2± 37.6	294.7± 29.2	173.7± 2.8	25C
40	0.003	0.894± 0.058	79.3± 66.3	0.985± 0.007	310.5± 25.9	292.3± 27.7	174.4± 2.8	25C
40	0.005	0.903± 0.046	94.2± 57.9	0.988± 0.005	305.4± 20.9	284.6± 22.4	175.6± 1.7	25C
50	0.007	0.972± 0.020	40.8± 7.2	0.975± 0.005	335.6± 17.4	333.2± 17.1	173.1± 2.1	–
70	0.007	0.903± 0.056	93.2± 47.6	0.988± 0.006	302.5± 23.2	277.6± 25.2	175.8± 1.8	25C, 32S
80	0.00001	0.832± 0.062		0.986± 0.008	311.2± 17.2	293.9± 19.5	173.2± 3.4	25C
80	0.0001	0.848± 0.070		0.984± 0.009	313.5± 22.8	300.4± 21.0	172.4± 3.6	25C
80	0.001	0.851± 0.070	77.2± 71.5	0.984± 0.009	311.6± 23.7	301.3± 23.0	172.3± 4.0	25C
80	0.003	0.861± 0.059	78.5± 69.1	0.984± 0.008	314.7± 18.9	306.6± 28.7	172.4± 4.1	–

Table 2. - continued.

t_{ev}	β	q	a	e	ω	Ω	i	i.r.s.
				filament F4				
10	0.00001	0.776± 0.020	71.5± 10.0	0.989± 0.002	9.7± 7.8	-12.5± 7.3	178.0± 0.9	–
10	0.0001	0.891± 0.082		0.974± 0.017	20.3± 29.0	2.3± 29.2	175.6± 2.3	–
20	0.00001	0.871± 0.073	59.0± 53.0	0.978± 0.011	29.1± 21.5	12.1± 21.3	175.2± 3.0	–
20	0.0001	0.867± 0.071	66.9± 65.4	0.979± 0.012	28.6± 21.3	11.3± 21.1	175.6± 2.5	–
20	0.001	0.852± 0.045		0.986± 0.007	26.9± 18.2	6.5± 18.4	175.9± 1.9	–
20	0.003	0.874± 0.065	90.9± 56.8	0.985± 0.011	27.5± 17.2	7.2± 16.6	175.6± 2.8	–
40	0.00001	0.894± 0.073		0.978± 0.010	27.3± 19.9	13.6± 20.3	174.7± 3.1	–
40	0.0001	0.903± 0.072	52.1± 40.7	0.977± 0.010	26.5± 19.9	13.4± 20.0	174.5± 3.2	–
40	0.001	0.900± 0.058	56.9± 55.5	0.979± 0.010	26.7± 18.6	13.4± 20.3	174.7± 2.8	–
40	0.003	0.930± 0.066	61.2± 56.3	0.978± 0.010	22.1± 23.4	8.1± 23.0	175.3± 2.6	–
40	0.005	0.928± 0.034	55.2± 18.6	0.982± 0.006	16.1± 14.7	1.1± 13.4	175.4± 1.1	–
50	0.007	0.929± 0.042	74.1± 42.4	0.984± 0.008	24.5± 17.7	10.2± 15.5	174.8± 4.3	–
80	0.00001	0.790± 0.037	358.1±294.7	0.997± 0.002	64.6± 11.9	30.2± 12.0	173.2± 1.8	–
80	0.0001	0.792± 0.035		0.997± 0.002	65.7± 11.0	31.2± 11.5	173.1± 1.7	–
80	0.001	0.796± 0.039		0.997± 0.002	66.9± 11.4	32.4± 12.0	173.7± 1.4	–
80	0.003	0.948± 0.049		0.974± 0.009	359.4± 30.2	11.7± 28.9	171.1± 4.0	–
				filament F5				
70	0.007	0.875± 0.031	451.8± 392.8	0.997± 0.001	70.3± 7.8	34.1± 8.5	175.2± 0.7	–
78	0.007	0.882± 0.032		0.997± 0.002	51.7± 5.5	12.8± 5.8	172.3± 1.0	–
80	0.005	0.859± 0.032		0.996± 0.002	56.3± 7.5	21.0± 9.0	169.3± 3.3	–
80	0.007	0.874± 0.027	294.6± 226.5	0.996± 0.003	53.4± 6.3	18.3± 7.9	168.4± 3.2	–
80	0.009	0.893± 0.022	251.0± 207.8	0.996± 0.003	49.0± 5.4	11.8± 7.2	166.9± 4.6	–

Table 3. Mean geophysical characteristics of the real showers separated from the CAMS video (C) and SonotaCo video (S) databases and identified with at least one of predicted filaments (F1, F2, F3, or F4) of the modeled meteoroid stream of comet C/1964 N1. Notes: Cat.No. - the working number (in this work) of the shower in the C or S catalog (this number serves to relate the real shower to a filament in Tables 1 and 2); $\lambda_\odot$ - the mean solar longitude corresponding to the expected maximum of a shower; α and δ - the equatorial coordinates of mean geocentric radiant; V_g and V_h - the mean geocentric and heliocentric velocity; γ - the angular distance of the mean radiant from the Sun at the time corresponding to the $\lambda_\odot$ of the maximum; N_s - the number of the real meteors of a given shower selected from the given database; D_{lim} - the threshold value of the Southworth-Hawkins D-discriminant used to separate the meteors of the observed shower; i.p.f. - the predicted filament with which the given real shower is identified. Angular quantities are given in degrees, and velocities in $\mathrm{km\,s^{-1}}$.

Cat.No.	$\lambda_\odot$	α	δ	V_g	V_h	γ	N_s	D_{lim}	i.p.f.
13C	101.5± 7.8	22.1± 6.3	15.6± 2.4	69.1± 1.0	41.8± 0.8	75	13	0.14	F1
14C	195.2± 7.8	96.0± 6.9	27.3± 1.0	70.4± 0.2	41.7± 0.2	100	9	0.10	F2
15C	115.7± 6.8	32.1± 5.0	21.5± 2.7	68.4± 0.7	40.6± 0.5	79	8	0.10	F1
16C	135.6± 12.9	48.3± 10.4	26.1± 3.4	69.5± 0.8	41.0± 0.7	83	20	0.15	F1
17C	143.8± 6.3	57.1± 5.2	28.4± 1.5	69.3± 0.5	40.7± 0.5	83	8	0.10	F1
18C	199.6± 7.3	100.1± 6.2	27.5± 1.0	70.3± 0.4	41.7± 0.3	101	7	0.09	F2
23C	215.7± 6.2	117.6± 5.0	28.4± 1.5	69.8± 0.5	41.4± 0.5	101	9	0.11	F2
24C	210.8± 9.9	116.5± 8.0	28.0± 1.1	70.9± 0.6	41.9± 0.4	97	6	0.10	F2
25C	113.2± 7.4	36.2± 5.5	8.9± 2.1	68.8± 0.5	41.1± 0.5	76	18	0.10	F3
26C	211.5± 8.6	117.3± 6.8	27.0± 1.9	70.9± 0.5	41.8± 0.3	97	9	0.11	F2
3S	101.3± 34.9	35.3± 3.2	8.9± 1.2	69.4± 0.4	41.7± 0.3	65	20	0.08	F3
10S	145.1± 8.8	56.8± 6.8	27.3± 1.7	70.2± 0.4	41.4± 0.5	85	5	0.10	F1
20S	153.8± 81.3	92.2± 5.7	27.2± 0.9	70.5± 0.6	41.7± 0.5	62	10	0.09	F2
22S	221.3± 56.3	102.5± 4.8	28.5± 0.9	70.4± 0.4	42.0± 0.5	120	8	0.07	F2
24S	204.6± 3.6	103.4± 3.3	28.2± 0.6	70.9± 0.4	42.7± 0.3	103	10	0.07	F2
30S	104.0± 32.3	36.0± 3.4	9.0± 1.2	69.3± 0.4	41.6± 0.4	67	24	0.09	F3
32S	105.0± 29.3	35.3± 2.8	8.9± 1.3	69.5± 0.4	41.7± 0.3	69	15	0.06	F3

Table 4. Mean orbital characteristics, with the dispersion, of the real showers separated from the CAMS video (C) and SonotaCo video (S) databases and identified with at least one of predicted filaments (F1, F2, F3, or F4) of the modeled meteoroid stream of comet C/1964 N1. Notes: Cat.No. and i.p.f. - as in Table 3; q - the mean perihelion distance; a - the mean semi-major axis; e - the mean eccentricity; ω - the mean argument of perihelion; Ω - the mean longitude of ascending node; and i - the mean inclination to the ecliptic. Quantities q and a are given in astronomical units and angular elements in degrees.

Cat.No.	q	a	e	ω	Ω	i	i.p.f.
13C	0.838± 0.042	620.8± 498.0	1.001± 0.063	130.7± 6.7	101.5± 7.8	169.0± 3.2	F1
14C	0.905± 0.032	28.6± 16.8	0.960± 0.018	215.7± 6.0	195.2± 7.8	172.6± 1.8	F2
15C	0.898± 0.037	10.9± 5.8	0.900± 0.040	139.3± 7.1	115.7± 6.8	165.5± 2.2	F1
16C	0.961± 0.040	168.2± 358.9	0.928± 0.061	155.5± 11.8	135.5± 12.9	165.8± 2.9	F1
17C	0.964± 0.019	19.1± 27.4	0.899± 0.049	154.6± 5.9	143.7± 6.3	165.6± 2.0	F1
18C	0.891± 0.035	29.1± 19.7	0.957± 0.022	218.2± 6.5	199.6± 7.3	172.0± 1.9	F2
23C	0.869± 0.041	18.9± 13.3	0.931± 0.043	221.8± 6.6	215.7± 6.3	166.7± 2.3	F2
24C	0.937± 0.036	346.1± 505.8	0.970± 0.035	206.9± 10.1	210.7± 9.9	168.1± 1.8	F2
25C	0.854± 0.036	75.8± 231.1	0.944± 0.040	312.5± 5.7	293.2± 7.4	170.7± 1.4	F3
26C	0.940± 0.034	237.2± 431.9	0.963± 0.030	206.1± 9.2	211.4± 8.6	169.5± 2.7	F2
3S	0.857± 0.027	20.6± 35.6	0.992± 0.028	313.4± 4.3	292.2± 4.4	171.1± 1.5	F3
10S	0.983± 0.022	13.2± 15.3	0.954± 0.043	161.8± 9.2	145.1± 8.8	167.4± 1.5	F1
20S	0.907± 0.030	5.9± 14.9	0.967± 0.040	215.6± 6.1	191.8± 6.5	173.2± 1.6	F2
22S	0.883± 0.028	14.3± 26.0	0.981± 0.038	219.6± 4.9	202.2± 5.5	169.9± 1.1	F2
24S	0.857± 0.019	-2.4 ± 24.1	1.041± 0.026	223.4± 3.1	204.6± 3.6	170.5± 1.2	F2
30S	0.860± 0.027	19.8± 32.5	0.983± 0.033	313.7± 4.3	293.0± 4.6	170.9± 1.5	F3
32S	0.860± 0.025	19.7± 33.7	0.995± 0.027	313.9± 3.9	292.3± 4.1	171.1± 1.1	F3

Table 5. The showers from the IAU MDC list of all showers found to be related to the predicted showers with meteoroids originating in comet C/1964 N1. In the first column of the table, the evolutionary time, t_{ev}, and the mark "MDC:" are given. While t_{ev} is applicable to the theoretical shower, mark "MDC:" is applicable to the real shower from the IAU MDC list. In the second column, the P-R-effect parameter β is applicable to the theoretical shower and the IAU MDC number, MDC No., to the real shower. In the third last column of Part 1, the number of theoretical particles used to predict the shower, N_{tp} (applicable to the theoretical shower), and the number of real meteors, N_{real} (applicable to the real shower), identified by the original author to be the members of the shower are given. The value of the Southworth-Hawkins D-discriminant between the mean orbits of both predicted and real showers is given in the last but one column of the first part of the table. The meaning of other symbols is following: $\lambda_{\odot}$ - the mean solar longitude, α and δ - the mean right ascension and mean declination of the geocentric radiant, V_g - the mean geocentric velocity, q - the mean perihelion distance, a - the mean semi-major axis, e - the mean eccentricity, ω - the mean argument of perihelion, Ω - the mean longitude of ascending node, and i - the mean inclination to the ecliptic.

PART 1 - geophysical data

t_{ev} [kyr]; MDC	β; MDC No.	$\lambda_{\odot}$ [deg]	α [deg]	δ [deg]	V_g [km s^{-1}]	N_{tp}; N_{real}	D_{SH}	source
relation to filament F2								
10	0.00500	214.1	109.5	25.1	69.80	64		this work
MDC:	23	206.0	101.6	26.7	68.80	3	0.194	Jenniskens, 2012
MDC:	23	206.0	104.8	26.9	69.40	7	0.100	Cook, 1973
40	0.00001	201.7	100.0	27.1	70.30	4059		this work
MDC:	23	198.0	93.8	28.1	69.60	31	0.163	Jenniskens et al., 2016a
relation to filament F3								
20	0.00300	111.3	34.3	10.5	69.30	852		this work
MDC:	533	112.6	35.0	9.2	68.85	19	0.078	Kornoš et al., 2014b
40	0.00001	117.0	39.2	11.4	69.40	1724		this work
MDC:	533	119.0	40.1	10.6	69.40	61	0.053	Šegon et al., 2014
40	0.00010	116.0	38.4	11.1	69.40	1572		this work
MDC:	533	119.0	40.1	10.6	69.40	61	0.053	Šegon et al., 2014
40	0.00010	116.0	38.4	11.1	69.40	1572		this work
MDC:	533	119.0	41.5	10.7	68.90	20	0.070	Jenniskens et al., 2016b

Table 5. − continued.

PART 1 - geophysical data; continuation

t_{ev} [kyr]; MDC	β; MDC No.	$\lambda_\odot$ [deg]	α [deg]	δ [deg]	V_g [km s^{-1}]	N_{tp}; N_{real}	D_{SH}	source
relation to filament F5								
80	0.00500	190.5	87.2	17.8	70.00	114		this work
(MDC:	718	206.0	96.9	12.7	68.10	33	0.217	Jenniskens et al., 2016a)

PART 2 - orbital elements

t_{ev}; MDC	β; No.	q [au]	a [au]	e	ω [deg]	Ω [deg]	i [deg]	source
relation to filament F2								
10	0.00500	0.776	342.7	0.997	261.1	238.4	174.0	this work
MDC:	23	0.731	10.0	0.927	241.7	209.0	172.9	Jenniskens, 2012
MDC:	23	0.770	26.8	0.971	237.0	209.7	173.0	Cook, 1973
40	0.00001	0.848	119.3	0.991	223.9	200.5	172.4	this work
MDC:	23	0.813	11.3	0.957	230.9	198.4	171.2	Jenniskens et al., 2016a
relation to filament F3								
20	0.00300	0.849	102.0	0.989	298.4	278.6	174.3	this work
MDC:	533	0.863		0.939	313.8	292.6	171.8	Kornoš et al., 2014b
40	0.00001	0.859	70.8	0.984	311.1	293.7	173.4	this work
MDC:	533	0.883		0.965	318.0	299.0	171.6	Šegon et al., 2014
40	0.00010	0.856	75.5	0.984	310.7	293.1	173.3	this work
MDC:	533	0.883		0.965	318.0	299.0	171.6	Šegon et al., 2014
40	0.00010	0.856	75.5	0.984	310.7	293.1	173.3	this work
MDC:	533	0.860	10.7	0.952	312.4	292.7	170.4	Jenniskens et al., 2016b
relation to filament F5								
80	0.00500	0.859	337.1	0.996	56.3	21.0	169.3	this work
(MDC:	718	0.726	5.8	0.952	60.8	26.3	159.9	Jenniskens et al., 2016a)